

PERFLUOROPOLYETHER-BASED ELECTROLYTES
FOR LITHIUM BATTERY APPLICATIONS

Hiu Ching Wong

A dissertation submitted to the faculty of the University of North Carolina at Chapel Hill in partial fulfillment of the requirements for the degree of Doctor of Philosophy in the Department of Chemistry

Chapel Hill
2015

Approved by:

Joseph M. DeSimone

Sergei S. Sheiko

Valerie Ashby

Royce W. Murray

Michel Gagné

© 2015
Hiu Ching Wong
ALL RIGHTS RESERVED

ABSTRACT

HIU CHING WONG: Perfluoropolyether-based Electrolytes for
Lithium Battery Applications
(under the direction of Prof. Joseph M. DeSimone)

Large-scale rechargeable batteries are expected to play a key role in today's emerging sustainable energy landscape. State-of-the-art lithium-ion batteries are not only widely used in electric vehicles, but they are currently gaining traction as backup power in aircraft and smart grid applications. In all of these cases, safety surrounding the electrolyte, an essential component of a lithium-ion battery, is a challenging limitation: the low flash points of currently used small molecule organic alkyl carbonates impose a high risk of ignition under most operating conditions. For this reason, extensive efforts are being made to develop viable nonflammable electrolytes to replace these organic solvents.

Herein, we describe new classes of nonflammable liquid and solid electrolytes composed of oligomeric perfluoropolyethers. These materials are promising electrolyte alternatives due to their low glass transition temperatures, high chemical stability, capacity to dissolve lithium salts such as lithium bis(trifluoromethane)sulfonimide lithium salt, and compatibility with various common polymers such as poly(ethylene glycol). Synthetic modifications used to introduce a wide range of functional groups has created a platform of intrinsically fireproof materials that can be chemically tailored to achieve the desired physical, thermal, mechanical, and electrochemical properties for specific battery applications. Using this approach carbonate-, thiol-, allyl-, and propargyl- functionalized perfluoropolyethers were prepared from the

commercially available hydroxyl-terminated PFPEs. The terminal group and molecular weight effects on the bulk properties of these materials were systematically characterized and their viability as electrolytes was evaluated.

The described work ultimately paves the way towards further optimization of perfluoropolyether materials towards the development of high performance lithium- ion batteries. The interesting properties of these materials invite an extensive study into the fundamental mesoscale ion transport and the relationship between perfluoropolyether chemical structure and electrolyte electrochemical property, as well as a closer analysis into the perfluoropolyether and electrode interface. Investigation in these areas using techniques such as advanced nuclear magnetic resonance spectroscopy and transmission electron microscopy is proposed.

ACKNOWLEDGEMENTS

The author acknowledges those who contributed to and assisted with the work herein: Dr. Didier Devaux, Dr. Alessandra Vitale, Dr. Daniel Hallinan Jr., Jacob Thelen, William Daniel, Dr. Yanbao Fu, Dr. Sue Mecham, Mahati Chintapalli, Alexander Lapidés, Dr. Ashish Pandya, and Dr. Simon Lux. The work described especially in the fourth chapter would not materialize without the contributions of two young talented scientists, Kevin Olson and Austria Taylor; it was such a pleasure to have the opportunity to mentor them during my graduate experience. My gratitude additionally extends to Dr. Yapei Wang, Dr. Mark Elsesser, Dr. David Wong, Crista Farrell, Vicki Haithcock, and Dr. J. Chris Luft for some great conversations and their countless support in my professional development. Of course, I would also like to sincerely thank my principal investigator Professor Joseph M. DeSimone; it has been an honor to be a part of his team and grow as a researcher under his technical and professional guidance.

My pursuit of a graduate degree at North Carolina was largely due to the efforts of Professor Alex Adronov, my mentor and former advisor at McMaster University. The many times in which he had more confidence in me than I had for myself taught me valuable lessons in maturity and perseverance and his wise words continue to resonate whenever I encounter scientific and professional challenges.

While many students only have one advisor in their graduate career, I was fortunate to feel that I had two through my multiple collaborations with Dr. Nitash Balsara; I sincerely thank Professor Balsara for his mentorship and his group members for their hospitality and kindness

during my time spent at the University of California, Berkeley and Lawrence Berkeley National Laboratory.

My entire experience would definitely not have been possible without the continued and unconditional support from my family: my parents, Chris and Vizona, and my brother, Jonathan. I would also like to thank my friends Tiffany, Quynh, Daniel, Sarah, Tessa, and Stuart, and many others who were an instrumental source for motivation and encouragement.

Last but not least, with all my heart, I would like to thank and dedicate this work to Zachary Lewis Rodgers, who continues to inspire me everyday on and beyond the benchtop.

"What we call the beginning is often the end. And to make an end is to make a beginning. The end is where we start from."

- T.S. Elliot

TABLE OF CONTENTS

LIST OF TABLES.....	xii
LIST OF FIGURES.....	xiii
LIST OF ABBREVIATIONS.....	xix
CHAPTER 1: INTRODUCTION TO LITHIUM-ION BATTERIES.....	1
1.1 Introduction to Lithium-Ion Batteries.....	1
1.1.1 Battery History, Terminology, and Chemistry	2
1.1.2 Concerns Regarding Battery Electrolytes.....	4
1.1.3 Current Efforts in Electrolyte Research.....	5
1.1.4 Liquid Electrolytes.....	6
1.1.4.1 Development of Fire Retardant Additives	6
1.1.4.2 Room Temperature Ionic Liquids.....	6
1.1.5 Solid-State Electrolytes.....	7
1.1.6 Hybrid Electrolytes and Other Systems.....	9
1.2 Perfluoropolyethers.....	9
1.2.1 Methods Used to Synthesize PFPEs	10
1.2.1.1 Anionic Ring Opening Polymerization of Hexafluoropropylene Oxide	10
1.2.1.2 Direct Fluorination.....	11
1.2.1.3 Photooxidation.....	12
1.2.2 PFPE Uses and Applications	14
1.3 Techniques for Electrolyte Characterization.....	18

1.3.1	Physical and Thermal Characterization	18
1.3.1.1	Thermogravimetric Analysis	18
1.3.1.2	Different Scanning Calorimetry.....	19
1.3.1.3	Flammability Tests	20
1.3.1.4	Viscosity	21
1.3.2	Characterization of Elastomers	22
1.3.3	Electrochemical Characterization	24
1.3.3.1	Ionic Conductivity	24
1.3.3.2	Electrochemical Window	25
1.3.3.3	Battery Performance	26
1.3.4	Lithium-Ion Transference Number	27
1.3.4.1	Lithium-Ion Transference Number Using Pulsed Field Gradient NMR	28
1.3.4.2	Other Methods of Measuring Li-ion t^+ 's	30
1.3.4.2.1	Potentiostatic Polarization	30
1.3.4.2.2	Galvanostatic Polarization	31
1.3.4.2.3	Electromotive Force Method	31
	REFERENCES	34
CHAPTER 2: PFPE/PEG BLENDS AS LI- ION BATTERY ELECTROLYTES.....		40
2.1	Introduction to Perfluoropolyether/Poly(ethylene glycol) Blends.....	40
2.1.1	Investigations of Blends of Oligomers of PFPE and PEG with a Lithium Salt	42
2.2	Materials.....	43
2.3	Experimental.....	43
2.3.1	Characterization of Physical and Thermal Properties.....	43

2.3.2	Electrochemical Characterization	44
2.4	Results and Discussion.....	44
2.5	Conclusion.....	58
	REFERENCES	59
CHAPTER 3: NOVEL PERFLUOROPOLYETHER-BASED ELECTROLYTES		62
3.1	Investigations of Perfluoropolyether/Carbonate Electrolytes.....	62
3.2	Materials.....	64
3.3	Experimental.....	64
3.3.1	Synthesis of PFPE-Dimethyl Carbonate.....	64
3.3.2	Physical and Thermal Characterization	65
3.3.3	NMR Characterization of PFPEs	66
3.3.4	Electrochemical Characterization	68
3.3.5	Determination of t^+ using Alternating Current Impedance Spectroscopy	68
3.3.6	Electrochemical Coin Cell Testing.....	70
3.4	Results and Discussion.....	71
3.5	Future Directions for PFPE-Dimethyl Carbonate Electrolytes.....	83
	REFERENCES	84
CHAPTER 4: FURTHER MODIFICATIONS OF PERFLUOROPOLYETHERS		87
4.1	PFPEs as a Chemical Platform for End Group Functionalization.....	87
4.2	Part A: Effect of Functional Groups on Electrolyte Properties.....	87
4.2.1	Materials	88
4.2.2	Experimental.....	89
4.2.2.1	Synthesis of PFPE _{E10} -Dimethyl Carbonate	89

4.2.2.2	Synthesis of PFPE _{E10} - Diallyl Carbonate	89
4.2.2.3	Synthesis of PFPE _{E10} -Dipropargyl Carbonate	90
4.2.2.4	Physical Characterization of PFPEs	90
4.2.3	Results and Discussion	91
4.3	Part B: Translation to Ultraviolet-Curable PFPE Electrolytes.....	100
4.3.1	Materials	101
4.3.2	Experimental.....	102
4.3.2.1	Synthesis of PFPE-Dimethacrylate.....	102
4.3.2.2	Synthesis of PFPE-Dithiol	102
4.3.2.3	Photocuring of PFPE Precursors.....	103
4.3.2.4	Characterization of Crosslinked PFPEs	103
4.3.3	Results and Discussion	104
	REFERENCES	112
	CHAPTER 5: ONGOING AND FUTURE DIRECTIONS.....	115
5.1	Introduction.....	115
5.2	NMR as a Tool to Study Ion Transport in Electrolytes.....	115
5.2.1	Using pfg-NMR to Measure t^+ 's in PFPE Electrolytes	116
5.2.1.1	Preliminary Experiments and Results.....	116
5.2.1.1.1	Materials	116
5.2.1.2	Experimental.....	117
5.2.1.2.1	Synthesis of PFPE-Dimethyl Carbonate.....	117
5.2.1.2.2	Preparation of NMR Samples	117
5.2.1.2.3	Pfg-NMR Experimental Procedure.....	118

5.2.1.3	Discussion of Preliminary Results	119
5.2.2	Other Possible NMR Experiments: Determination of Linewidth and Relaxation	125
5.2.2.1	Linewidth	125
5.2.2.2	Relaxation	127
5.3	Investigation of PFPE/Electrode Interfaces.....	128
5.3.1	Characterization of PFPE/Electrode Interfaces	130
5.3.2	Enhancing SEI Formation through Incorporation of Ethylene Carbonate.....	131
5.3.3	Investigation of Failure Modes	133
	REFERENCES	134

LIST OF TABLES

Table 1.1 Example of hybrid electrolytes, as reported by Kim and coworkers in <i>Chemistry of Materials</i> . ²⁷	9
Table 2.1 Sustained burning information for PFPE+PEG Electrolyte ($r=0.026$).....	50
Table 2.2 Selected peaks and full widths at half maximum of ¹⁹ F NMR for PEG, PFPE+PEG and PFPE electrolytes.	56
Table 2.3 VTF fitted parameters for PEG, PFPE+PEG and PFPE electrolytes containing LiTFSI ($r = 0.026$).	57
Table 3.1 Chemical shift analysis of a ¹⁹ F NMR spectrum of PFPE ₁₀₀₀ -diol. Peaks a-h correspond to peaks a-h in Figure 3.2.	67
Table 3.2 Determination of m:n and number of repeating units for PFPE ₁₄₀₀ -diol, PFPE ₂₀₀₀ -diol, and PFPE ₄₀₀₀ -diol.....	67
Table 3.3 PFPEs studied with their corresponding degrees of polymerization and T_g 's.	72
Table 4.1 Determination of m:n:q ratio and number of units for PFPE _{E10} -diol.....	92
Table 4.2 Thermal properties of PFPE _{E10} -diol and synthesized dicarbonate derivatives	95
Table 4.4 Corresponding decomposition temperature (5%), sustained burning characteristics, and flash points of these materials.	73
Table 4.5 VFT parameters calculated for PFPE ₁₀₀₀ -DMC electrolytes	78

LIST OF FIGURES

Figure 1.1 Li-ion battery market revenue breakdown in 2013 and the projected breakdown in 2020, as published by <i>Frost and Sullivan</i> . ¹	1
Figure 1.2 Li-ion battery in various configurations as published by Armand and coworkers in <i>Nature</i> : (a) cylindrical (b) coin (c) prismatic or pouch unit, and (d) flat. ³ ...	3
Figure 1.3 Schematic of the charge (<i>left</i>) and discharge (<i>right</i>) process of a Li-ion battery. ⁹	4
Figure 1.4 Japan Airlines Boeing 787 Dreamliner at Boston Logan Airport with smoke from battery fire. ¹⁴	5
Figure 1.5 Chemical structures of typical RTILs, as reported by Stepniak and coworkers in <i>Electrochimic Acta</i> . ²⁴	7
Figure 1.6 Intrachain (top) and interchain (bottom) hopping of ions facilitated by segmental motion of polymer chains. ³⁴	8
Figure 1.7 Different types of branched and linear PFPEs with various end group functionalities.....	10
Figure 1.8 Anionic ring opening of HFPO in the presence of CsF and TG. ⁴⁰	11
Figure 1.9 Lewis acid catalyzed ring opening polymerization of 2,2,3,3-tetrafluorooxetane following by direct fluorination under UV light. ³⁹	11
Figure 1.10 Synthetic schemes outlining the initiation, propagation, and termination of PFPE polymerization. ⁴⁹	13
Figure 1.11 Temperature range of use of PFPEs relative to other lubricants and oils. ⁵³	15
Figure 1.12 Microchannel section and sidewall of PFPE microfluidic device (left); PFPE device filled with colored water-based solution (as reported by Bongiovanni and coworkers in <i>Langmuir</i>). ⁵⁴	16
Figure 1.13 Density of attached spores of <i>Ulva</i> on PDMS and PFPE elastomers containing sPFPE and sPFPE with 10% SS after a 1h settlement period, as reported by DeSimone and coworkers in <i>Macromolecules</i> . Bars show 95 % confidence limits. ⁶⁶	17
Figure 1.14 Synthetic scheme of PFPE/PEG networks via a precursor approach, as reported by DeSimone and coworkers in <i>the Journal of the American Chemical Society</i> . ⁶⁴	17

Figure 1.15 Final density of attached diatoms on PFPE/PEG coatings. Bars show 95% confidence limits, as reported by DeSimone and coworkers in <i>Biofouling</i> . ⁶⁵	18
Figure 1.16 Sample DSC curve illustrating the T_g , T_c and T_m of a sample. ⁷⁰	20
Figure 1.17 Example of a customized ignition test involving exposing a flame to an electrolyte-soaked membrane. ⁷⁴	21
Figure 1.18 Sample apparatus of sustained burning test in accordance with ASTM D4206.....	21
Figure 1.19 Stress strain plot and characteristic curves of rigid plastics, fibers, flexible plastics, and elastomers. ⁸¹	23
Figure 1.20 Sample Nyquist plot obtained from EIS. ⁸³	25
Figure 1.21 Components of an assembled battery coin cell.	26
Figure 1.22 Sample galvanostatic cycling of a battery cell between 2.75 V and 4.25 V at a C-rate of 20 C.....	27
Figure 1.23 Sample diffusion spectrum of two signals decaying in intensity as magnetic field gradient strength increases. ⁹⁰	29
Figure 1.24 Sample plot of diffusion peak intensity as a function of gradient field strength. ⁹⁰	29
Figure 1.25 Sample E_{trans} vs. E plot produced by the electromotive force method for an EC/DEC electrolyte, as reported by Gores and coworkers in <i>Electrochimica Acta</i> . ⁸⁶	33
Figure 2.1 Photograph of PFPE/PEG blend films that are optically transparent or opaque based on different composition ratios and molar masses, as reported by DeSimone and coworkers in <i>the Journal of the American Chemical Society</i> . X-axis denotes the molar mass of PFPE and PEG and Y-axis represent composition ratios. ²²	41
Figure 2.2 Chemical structures of PFPE-diol, PEG-diol, and LiTFSI.....	42
Figure 2.3 Representative DSC heating curve of an immiscible ternary blend (PFPE with 0.10 and 0.45 wt. fractions of LiTFSI and PEG respectively), exhibiting two distinct T_g 's at -78 °C and -64 °C.	45

Figure 2.4 Photograph of miscible and immiscible ternary blends PFPE/PEG/ LiTFSI and ternary phase diagram of PFPE, PEG, and LiTFSI physical blends expressed in wt. fractions.	46
Figure 2.5 FTIR spectra of PFPE, PEG, LiTFSI and blended solutions at various wt. fractions. Highlighted guidelines are shown at 748, 798, 1190, 1325 and 1345 cm^{-1} respectively.	48
Figure 2.6 DSC cooling traces of PFPE and PEG blends at various PFPE wt. fractions.....	49
Figure 2.7 Percent crystallinity, expressed in X_c , as a function of PFPE wt. fraction.	49
Figure 2.8 Thermogram of PFPE/PEG Blend ($[\text{PFPE}]/[\text{PEG}]=1.6$) with LiTFSI concentration $r = 0.026$. ($T_d(5\%) = 197.84\text{ }^\circ\text{C}$) in N_2	50
Figure 2.9 T_g of PFPE (Δ), PEG (\square), and PFPE+PEG blend (\circ) electrolytes as a function of salt concentration r ; dotted lines represent fitted linear regressions.....	52
Figure 2.10 ^{19}F NMR spectra of PFPE, PEG, and PFPE+PEG electrolytes in reference to 0.05 M LiTFSI in D_2O and pure PFPE. Highlighted guidelines are shown at -79.94, -83.49, and -85.51 ppm.	55
Figure 2.11 Temperature-dependent ionic conductivities of PFPE (black Δ), PEG (blue \square), and PFPE/PEG blend (red \circ) electrolytes ($r = 0.026$); each sample follow VTF behavior.....	57
Figure 3.1 ^1H NMR of PFPE ₁₀₀₀ -DMC in CDCl_3	65
Figure 3.2 ^{19}F NMR of PFPE ₁₀₀₀ -diol obtained in CDCl_3 . Peak labels a-h correspond to peaks a-h in Table 3.1	67
Figure 3.3 Nyquist plot obtained from AC Impedance for PFPE ₁₀₀₀ -DMC electrolyte. Open symbols represent the experimental spectrum while the line is the modeling using electrical equivalent circuit.....	69
Figure 3.4 Electrical model used to fit the Nyquist plot.	69
Figure 3.5 t^+ measurements of cells containing 50 μm PFPE ₁₀₀₀ -DMC electrolyte using the Bruce and Vincent method using a 20 mV polarization at 38.8 $^\circ\text{C}$	70
Figure 3.6 Chemical reaction scheme describing the synthesis of PFPE-DMC from PFPE-diol.	72

Figure 3.7 TG curves for thermal decompositions of DMC (solid grey), PFPE ₁₀₀₀ -diol (dash blue), and PFPE ₁₀₀₀ -DMC (solid green).....	73
Figure 3.8 Characterization of LiTFSI loading in PFPE electrolytes. (A) Maximum LiTFSI loading in PFPE-diols (blue) and PFPE-DMCs (green) expressed in r_{max} , the molar ratio of Li-ions to repeating fluoroether units and molarity, and in R_{max} (<i>inset</i>), the molar ratio of Li-ions to end group functionalities, as a function of molecular weight. (B) FTIR spectra of PFPE ₁₀₀₀ -DMC/LiTFSI blends at different concentrations.	75
Figure 3.9 FTIR of PFPE ₁₀₀₀ -diol/LiTFSI blends compared to pure PFPE ₁₀₀₀ -diol and LiTFSI.	76
Figure 3.10 Electrochemical behavior of PFPE electrolytes. (A) Ionic conductivities of PFPE ₁₀₀₀ -diol (filled black circles), PFPE ₁₄₀₀ -diol (filled green squares), PFPE ₂₀₀₀ -diol (filled blue triangles), PFPE ₄₀₀₀ -diol (filled red diamonds), PFPE ₁₀₀₀ -DMC (open black circles), PFPE ₁₄₀₀ -DMC (open green squares), PFPE ₂₀₀₀ -DMC (open blue triangles), PFPE ₄₀₀₀ -DMC (open red diamonds) with LiTFSI at 30°C as a function of r . (B) t^+ (open green triangles) and temperature-dependent conductivity (filled blue squares) of PFPE ₁₀₀₀ -DMC. Conductivity follows VFT regression (grey, $A = 5 \cdot 10^{-4} \text{ Scm}^{-1} \text{ K}^{-0.5}$, $B = 0.47 \text{ kJmol}^{-1}$, $T_0 = 271 \text{ K}$).	78
Figure 3.11 Nyquist plot obtained from AC impedance for SEO polymer electrolyte. t^+ was calculated to be 0.12.	80
Figure 3.12 Cyclic voltammograms of PFPE ₁₀₀₀ -DMC at 1 mV.s ⁻¹ from a Li/Electrolyte/Stainless steel cell obtained at every fifth cycle at 40 °C (blue), 60 °C (green), 80 °C (orange), and 100 °C (red).....	81
Figure 3.13 Cyclability of Li/PFPE ₁₀₀₀ -DMC-LiTFSI/LiNMC cells. (A) Discharge profiles obtained at 30 °C at different rates from C/20 to C/8 for a typical prototype Li/PFPE ₁₀₀₀ -DMC-LiTFSI/LiNMC. (B) Cycle performance of battery prototypes showing discharge (open green squares), charge (open blue squares) capacities, as well as overall efficiencies (filled grey circles).....	82
Figure 3.14 Cycle performance of LiPF ₆ -EC/DEC (1 M, 1:2 vol, Daikin Industries) batteries.	82
Figure 4.1 Chemical structure of PFPE _{E10} -diol	92
Figure 4.2 Synthetic scheme of PFPE _{E10} -diol to prepare PFPE _{E10} -DMC, PFPE _{E10} -DAC and PFPE _{E10} -DPC.	93
Figure 4.3 Li-ions are solvated by carbonyl oxygen atoms of carbonate molecules.	94

Figure 4.4 Thermogravimetric curves for thermal decomposition of PFPE _{E10} -diol and its derivatives obtained in N ₂	95
Figure 4.5 Maximum solubility of LiTFSI in different PFPE electrolytes.....	96
Figure 4.6 Viscosity as a function of salt concentration in PFPE electrolytes.	97
Figure 4.7 T_g as a function of salt concentration in PFPE _{E10} -diol and its derivatives.	98
Figure 4.8 IR spectra of PFPE _{E10} -DPC with 29 wt.% LiTFSI (purple) relative to pure PFPE _{E10} -DPC (black).....	99
Figure 4.9 Schematic of the synthesis of PFPE-DMA.	105
Figure 4.10 A schematic of the synthesis of PFPE-dithiol.	106
Figure 4.11 A schematic of the free-radical polymerization and thiol-ene click reaction between PFPE-DMA and PFPE-dithiol.....	106
Figure 4.12 Gel fraction of PFPE-DMA elastomers with various wt.% of PFPE-dithiol.....	107
Figure 4.13 Young's Modulus of PFPE elastomers with various wt. % of PFPE-dithiol.....	109
Figure 4.14 Stress strain curves for PFPE-DMA elastomers with various wt. % of PFPE-dithiol	109
Figure 4.15 The flexibility of (left) a PFPE-DMA elastomer compared to that of a PFPE-DMA with 20% PFPE-dithiol elastomer (right).....	109
Figure 4.16 Arrhenius plots of temperature-dependent ionic conductivity of PFPE-DMA elastomers with various wt.% of PFPE-dithiol.	111
Figure 5.1 Schematic of NMR sample set up using a coaxial insert. ⁶	118
Figure 5.2 Sample STEbp pulse sequence as observed in the nucleus channel (in this example figure the nucleus channel is ¹ H) and gradient channel (denoted by G). The radio frequency pulse, magnetic field gradient pulse, and acquisition of the free induction decay (FID) are also noted.	119
Figure 5.3 Measurement of D from STEbp and LEDbp sequences as a function of temperature.	120
Figure 5.4 ⁷ Li NMR Spectrum of PFPE-diol with 10 wt. % LiTFSI at 20 °C.	121

Figure 5.5 Simulated diffusion decay curve from 2 to 95% gradient strength in 14 steps obtained using Bruker TopSpin software. The data fit shown was achieved using equation 5.1.....	121
Figure 5.6 Diffusion decay curve where the intensity has not decayed sufficiently even at 95 % gradient strength.....	122
Figure 5.7 Diffusion coefficients of Li-ions in PFPE-DMC (open blue circles) and PFPE-diol (open red squares) as a function of temperature (K^{-1}).....	124
Figure 5.8 7Li NMR spectra of PFPE-diol containing 10 wt. % LiTFSI from 20 to $-40\text{ }^\circ C$ (293 to 233 K).	126
Figure 5.9 Illustration of a π pulse and its effects on magnetic spin. ²³	128
Figure 5.10 Sample graph of T_1 relaxation as a function of inverse temperature (K^{-1}). A T_1 minimum is shown here at approximately $3.15\text{ }K^{-1}$ ($44\text{ }^\circ C$).	128
Figure 5.11 In situ TEM experiments reported by Cui and coworkers in <i>Nano Letters</i> . (a) schematic of a typical in situ TEM cell. (b-d) Time series of the lithiation of a single silicon sphere (a-Si sphere and a-Li _x Si sphere indicates unlithiated and lithiated spheres respectively). ³³	131
Figure 5.12 Synthesis of vinyl ethers bearing carbonate side groups, as reported by Boutevin and coworkers in in <i>the Journal of Polymer Science</i> . ³⁸	132
Figure 5.13 Proposed synthetic scheme of the synthesis of PFPE-EC electrolytes	132
Figure 5.14 Dendritic lithium formed in a lithium battery, as observed by Notten and coworkers in <i>the Journal of Power Sources</i> . ⁴⁴	133

LIST OF ABBREVIATIONS AND SYMBOLS

A	constant proportional to the number of charge carriers
A/cm^2	Ampere per square centimeter
AC	alternating current
A_{eff}	or A in terms of electrochemical and mechanical testing; cross-sectional area
AFM	atomic force microscopy
ASTM	American Society for Testing and Materials
ATR	attenuated total reflectance
ATRP	atom-transfer radical-polymerization
B	activation energy for ion motion
BBO	broadband observe
C/n	charge rate
CDCl_3	deuterated chloroform
cP	centiPoises
CsF	cesium fluoride
CV	cyclic voltammetry
dyn/cm	dyne per centimeter
D	diffusion coefficient
D_2O	deuterated water
DAC	diallyl carbonate
DBTDA	dibutyltin diacetate
DC	direct current
DEC	diethyl carbonate

DMA	dimethylacrylate
DMC	dimethyl carbonate
DMSO	dimethyl sulfoxide
DP	degree of polymerization
DPC	diproparyl carbonate
DSC	differential scanning calorimetry
E	potential difference of cell in the presence of a salt bridge
E	Young's Modulus
E_{trans}	potential different of cell in absence of a salt bridge
EC	ethylene carbonate
EIS	electrochemical impedance spectroscopy
F	Faraday's constant
F_n	tensile force
FID	free induction decay
FTIR	Fourier transform infrared spectroscopy
FWHM	full width at half maximum
g	gradient strength
g/mL	gram per milliliter
g/mol	grams per moles
G	NMR gradient channel
h	hours
HCPK	α -hydroxycyclohexylphenyl ketone
HFPO	hexafluoropropylene oxide

HMIS	Hazardous Materials Identification System
I	in terms of NMR; observed intensity
I_0	in terms of NMR; reference intensity
IEM	2-Isocyanatoethyl methacrylate
ICPMS	inductively coupled plasma mass spectroscopy
IR	infrared spectroscopy
L	length
LEDbp	longitudinal eddy current delay with bipolar gradients
Li	lithium
Li-ion	lithium-ion
LiTFSI	bis(trifluoromethane)sulfonimide lithium salt
M_c	molecular weight between crosslinks
mg	milligram
mHz	millihertz
mm	millimeter
N_2	nitrogen gas
nm	nanometer
NMC	nickel manganese cobalt oxide
NMR	nuclear magnetic resonance spectroscopy
O_2	oxygen gas
PAN	polyacrylonitrile
PDMS	polydimethylsiloxane
PEG	poly(ethylene glycol)

PEO	poly(ethylene oxide)
pfg-NMR	pulsed-field gradient nuclear magnetic resonance spectroscopy
PFPE	perfluoropolyether
PFPE ₁₀₀₀ -X	<i>or</i> PFPE-X; materials synthesized from Fluorolink D10 or PFPE _{D10} -diol; X represents terminal functional group (allyl, DMC, propargyl, etc.) (Chemical structure found in Chapter 2.)
PFPE ₁₄₀₀ -X	materials synthesized from Fluorolink materials molecular weight 1400. X represents terminal functional group (allyl, DMC, propargyl, etc.) (Chemical structures found in Chapter 3)
PFPE ₂₀₀₀ -X	materials synthesized from Fluorolink materials molecular weight 2000. X represents terminal functional group (allyl, DMC, propargyl, etc.) (Chemical structures found in Chapter 3)
PFPE ₄₀₀₀ -X	materials synthesized from Fluorolink materials molecular weight 4000. X represents terminal functional group (allyl, DMC, propargyl, etc.) (Chemical structures found in Chapter 3)
PFPE _{E10} -X	materials synthesized from Fluorolink E10 or PFPE _{E10} -diol; X represents terminal functional group (allyl, DMC, propargyl, etc.) (Chemical structures found in Chapter 4.)
r	lithium salt concentration; molar ratio of lithium ions to polymer repeating units
r_{\max}	maximum molar ratio of lithium ions to polymer repeating units
R	ideal gas constant
R	in terms of electrochemical calculations; resistance
RTIL	room temperature ionic liquids
s	seconds
SE	spin echo
SEI	solid electrolyte interface
SEO	polystyrene-block-poly(ethylene oxide)
SPE	solid polymer electrolyte

STE	stimulated echo
STEBp	stimulate echo with bipolar gradients
S/cm	Siemens per centimeter
t^+	transference number
T_0	empirical reference temperature corresponding to zero configurational energy
T_1	spin-lattice relaxation
T_c	crystallization temperature
TEA	triethylamine
TFE	tetrafluoroethylene
T_g	glass transition temperature
TG	tetraglyme
TGA	thermogravimetric analysis
T_m	melting temperature
UV-Vis	ultraviolet visible spectroscopy
V	volts
VFT	Vogel-Tamman-Fulcher
X_c	degree of crystallization
XPS	x-ray photoelectron spectroscopy
wt.	weight
Δ	NMR diffusion time
Ω/cm^2	Ohm per square centimeter
γ	gyromagnetic ratio
δ	length of gradient

ε	in terms of tensile testing; engineering stress
ε	in terms of calculating ionic conductivity; porosity of separator
η	viscosity
ν_E	crosslink density
μ	mobility
σ	in terms of electrochemical notation; ionic conductivity
σ	in terms of tensile testing; engineering stress

CHAPTER 1

INTRODUCTION TO LITHIUM-ION BATTERIES

1.1 Introduction to Lithium-Ion Batteries

Lithium-ion (Li-ion) batteries are one of the most commonly used batteries in portable electronics such as cellphones and laptops. In contrast to primary batteries, which are non-rechargeable and disposable, Li-ion batteries belong in the family of secondary or rechargeable batteries, and therefore demonstrate drastically longer lifetimes. In addition, Li-ion batteries exhibit high energy density, slow loss in charge when not in use, and are significantly more lightweight than lead acid batteries. According to *Frost & Sullivan*, a global growth consulting firm that provides market research and analysis, the global Li-ion battery market was worth \$11.7 billion in 2012 and is expected to double by 2016.¹ While the handheld consumer segment currently dominates sales in this area, growth in this market is driven by the burgeoning automotive and utility segments, as utilities are seeking to use Li-ion batteries as energy storage and smart grid solutions to improve efficiency and effectiveness (Figure 1.1).

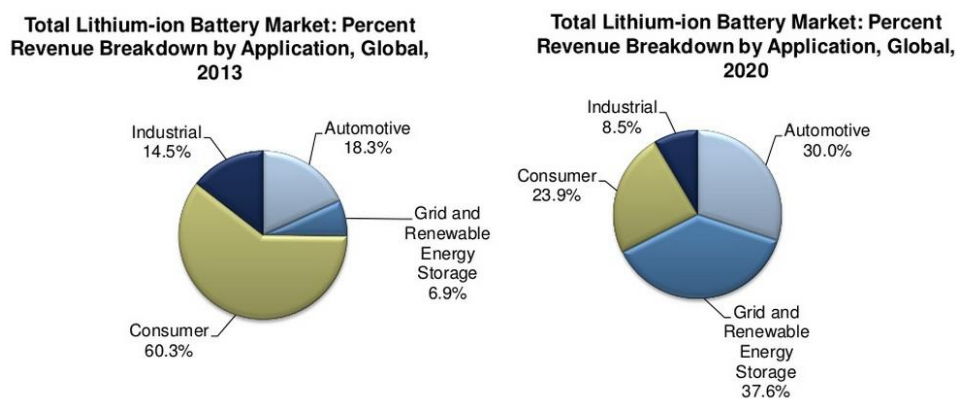


Figure 1.1 Li-ion battery market revenue breakdown in 2013 and the projected breakdown in 2020, as published by *Frost and Sullivan*.¹

1.1.1 Battery History, Terminology, and Chemistry

Nonrechargeable lithium (Li) batteries were first prepared by Dr. Michael Stanley Wittingham while he was working for Exxon Research and Engineering Company in 1976. Dr. John Goodenough, from Oxford University then the University of Texas at Austin, expanded this work in 1979 by developing rechargeable lithium ion cells composed of lithium cobalt oxide (LiCoO_2) and lithium metal as the cathode and anode respectively.² This was the first demonstration of cathode materials capable of reversible intercalation and stable donation of Li-ions. By 1991, Li-ion batteries containing LiCoO_2 were commercially released by Sony and Asahi Kasei; LiCoO_2 is now a ubiquitous material in today's portable electronic devices.

Although the two terms “battery” and “cell” are often used interchangeably to describe an electrochemical storage system, it is important to note the differences especially for industrial and commercial applications. A “cell” or “battery cell” is a basic electrochemical unit that contains the fundamental components such as the electrodes, electrolyte and oftentimes the separator. Battery cells are most commonly found in cylinder, coin, prismatic, and flat configurations (Figure 1.2). In contrast, a “battery”, also called a “battery pack”, is composed of a collection of cells, as well as the appropriate housing or casing, electrical interconnections and other types of electronics that control or stabilize the cells from overheating or overcharging. Larger applications such as laptops and zero emission vehicles use battery packs due to higher voltage requirements.

As previously mentioned, an electrochemical cell is fundamentally composed of an electrolyte sandwiched between two electrodes. The most widely used materials for these components are: an organic mixture usually of ethylene carbonate (EC), diethyl carbonate (DEC), and dimethyl carbonate (DMC) as the electrolyte, lithium cobalt oxide (LiCoO_2) as the

cathode, and carbon (in the form of graphite) as the anode. During the battery cell charge process, Li-ions move through the electrolyte from the positive electrode, the cathode, to the negative electrode, the anode. During the cell discharges, the direction of Li-ion migration is reversed, and Li-ions are intercalated back into LiCoO_2 (Figure 1.3), thus providing current through a load. These processes can also be described in terms of the following electrochemical half-reactions:

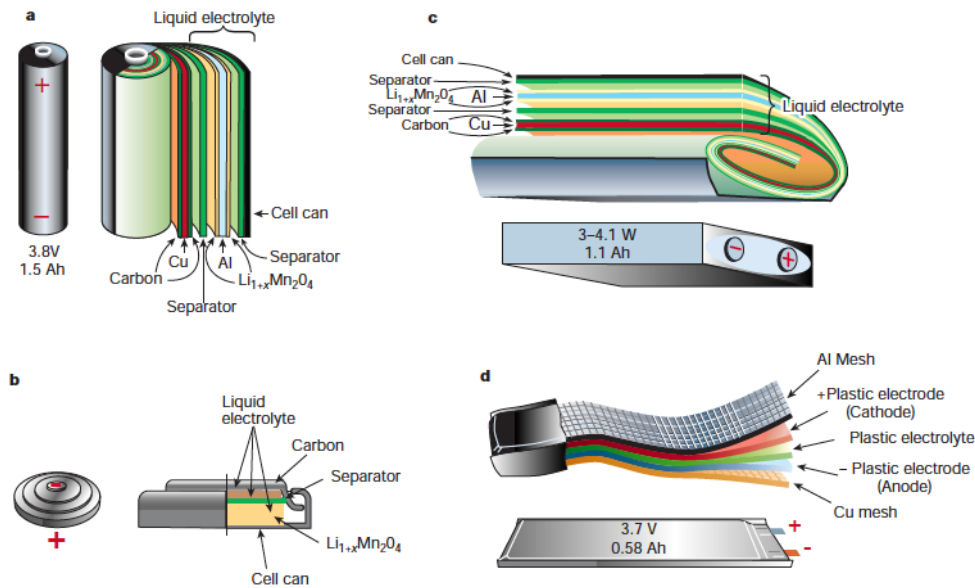
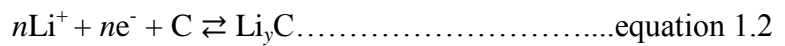
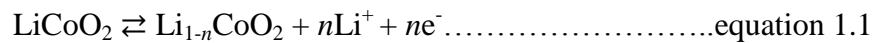


Figure 1.2 Li-ion battery in various configurations as published by Armand and coworkers in *Nature*: (a) cylindrical (b) coin (c) prismatic or pouch unit, and (d) flat.³

Researchers continue to explore the use of materials other than LiCoO_2 and graphite in order to improve the energy density, cost and durability of overall Li-ion batteries.

Commercially, there are growing trends of using lithium NMC,⁴ lithium manganese oxide

(LiMn_2O_4)⁵ and lithium iron phosphate (LiFePO_4)⁶ as cathode materials. For anodes, silicon⁷ and lithium titanium oxide⁸ are also gaining popularity.

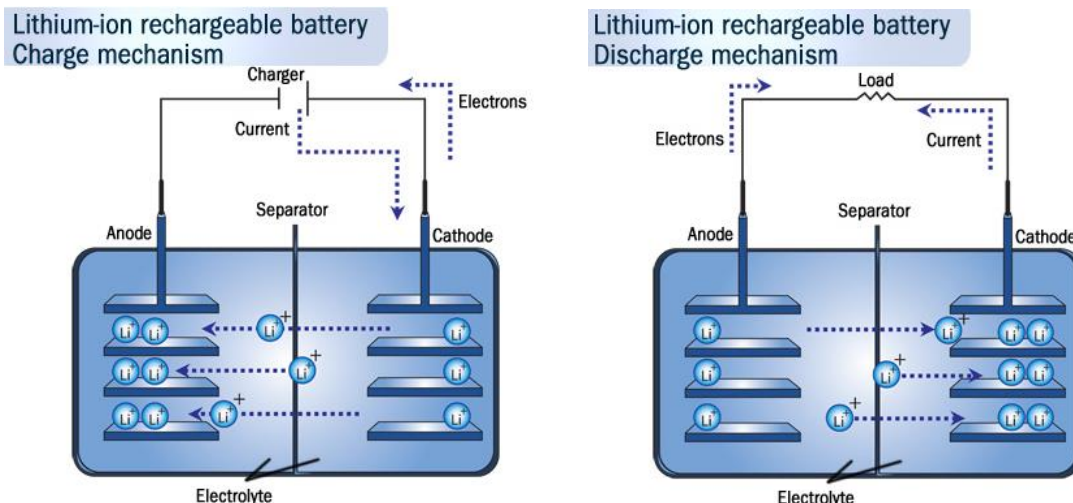


Figure 1.3 Schematic of the charge (*left*) and discharge (*right*) process of a lithium-ion battery.⁹

1.1.2 Concerns Regarding Battery Electrolytes

Material selection for Li-ion battery electrolytes is crucial as it acts as the media separating the cathode and anode, and therefore must be physically and electrochemically stable against both oxidizing and reducing chemistries. As a source of Li-ions, electrolytes contain lithium salts with large polarizable, monovalent anions such as hexafluorophosphate (PF_6^-), perchlorate (ClO_4^-), and bis(trifluoromethane)sulfonimide (TFSI).

Small molecule alkyl carbonates are currently the most commonly used liquid electrolytes for consumer and transportation battery applications. While these organic solvents are capable of dissolving large amounts of lithium salts and exhibit high ionic conductivities on the order of 10^{-2} S/cm at room temperature, they also exhibit low flash points and are therefore highly flammable and capable of spontaneous combustion. For example, DMC, an important component in commercial Li-ion battery electrolytes, has a Hazardous Materials Identification System (HMIS) flammability rating of 3 on a scale of 0 - 4, indicating a high risk of ignition

under most operating conditions. The intrinsic instability of carbonate-based solvents increases at higher temperatures, where exothermic electrolyte breakdown can lead to thermal runaway,^{10,11} resulting in battery short-circuiting and ultimately catastrophic failure of the battery. While this failure rate stands at about 1 in 10 million systems, this rate is intolerable for large-scale applications where catastrophic failure of one cell affects the operation of the battery pack as a whole; cost and user safety could also be heavily compromised. These safety issues were widely recognized when large Li-ion batteries were incorporated as back up power sources on aircraft; to date there have been at least five reported incidents of battery fires or smoke on the Boeing 787 Dreamliner passenger aircraft (Figure 1.4).^{12,13}



Figure 1.4 Japan Airlines Boeing 787 Dreamliner at Boston Logan Airport with smoke from battery fire.¹⁴

1.1.3 Current Efforts in Electrolyte Research

The safety hazards surrounding organic carbonate electrolyte solutions have prompted the search for new materials that possess the conductivity potential of classical EC/DEC/DMC systems yet are environmentally and thermally benign within operational limits. In the vast diversity of novel liquid materials found in the literature, research efforts can generally be categorized into the development of additives for alkyl carbonates and room temperature ionic

liquids. As alternatives to liquid electrolytes, solid-state polymeric electrolytes and hybrid systems have also garnered much interest.

1.1.4 Liquid Electrolytes

1.1.4.1 Development of Fire Retardant Additives

Fire retardant additives studied for Li-ion battery electrolytes are most commonly organophosphates and their halogenated derivatives;¹⁵⁻¹⁸ these chemicals reduce electrolyte flammability by acting as chemical radical scavengers that terminate radical chain reactions leading to combustion.^{16,17} While effective, there is oftentimes a trade-off between electrolyte flammability and reductive stability since many phosphates degrade against low reductive potentials and therefore are incompatible with anodes such as graphite.^{15,17}

In addition to phosphorus-based additives, small molecule ethers¹⁹⁻²¹ and fluorinated carbonates^{17,22,23} have also been reported. Because the lithium salt dissolution capabilities and electrochemical properties of these nonflammable molecules are limited, they must be diluted with traditional volatile carbonates and are strictly used as co-solvents. Elimination of flash point and flammability of the overall electrolyte is only achieved when fluorinated carbonates becomes the majority component.¹⁷

1.1.4.2 Room Temperature Ionic Liquids

Room temperature ionic liquids (RTILs) are a specific class of ionic liquids that exhibit melting temperatures below room temperature; they consist purely of large ions and their combinations and are free of any non-ionic small molecule solvent. RTILs are commonly quaternary ammonium salts such as tetralkylammonium or cyclic amines (Figure 1.5).²⁴ This group of molten salts has no measurable vapor pressure²⁵ and is thus considered nonflammable

and nonvolatile, which makes them of great interest in Li-ion battery research. However, the purity of RTILs is often an issue, as their moisture sensitivity significantly impacts their conductivity. The high viscosity that is characteristic for ionic liquids (in some cases as high as 500-600cP)^{24,26} can also cause difficulties with handling, which subsequently increases cost.

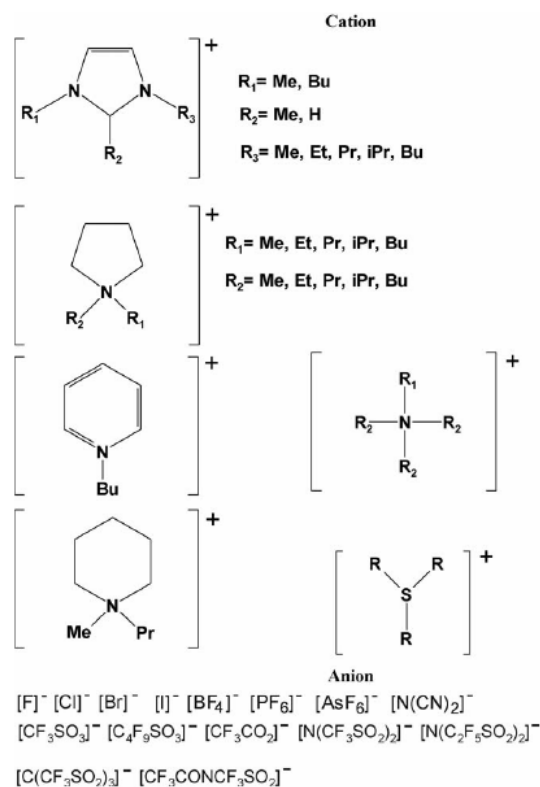


Figure 1.5 Chemical structures of typical RTILs, as reported by Stepniak and coworkers in *Electrochimica Acta*.²⁴

1.1.5 Solid-State Electrolytes

Dry polymer electrolytes are attractive alternatives to liquids due to the complete elimination of flammable solvents;^{3,27} polymeric electrolytes are also often cheaper and easier to process and handle.²⁸ Poly(ethylene oxide) (PEO)- and poly(ethylene glycol) (PEG)-based materials are the most extensively studied solid-state electrolytes due to their unique ability to solvate Li-ions. In these electrolytes, the Li-ions are complexed to ether oxygens of the polymer

backbone. There are two generally accepted mechanisms for ion transport in these materials: (i) the ion hopping mechanism where ions ‘hop’ from one region to the next, and (ii) the vehicular mechanism where the ion migrates with the solvation shell intact. In polymeric electrolytes, the latter is suppressed due to limited diffusion of polymer chains in entangled systems.²⁸ Ion transport in macromolecular electrolytes is therefore dominated by rapid segmental motion of polymer chains that lead to intrachain or interchain hopping of ions (Figure 1.6). Since polymer segmental motion is reduced as temperatures approach the glass transition temperature (T_g) of the polymer, a low T_g is an important property to achieve when selecting suitable materials for solid electrolyte design. The melting temperature, T_m , however, is also a big shortcoming of PEO polymers; its semi-crystalline nature limits practical ionic conductivity to temperatures above melting (typically at around 60 °C). Although strategies used to mitigate crystallinity span from the use of nanoparticle fillers such as aluminum oxide (Al_2O_3), titanium dioxide (TiO_2), and silicon dioxide (SiO_2)^{3,29} to novel macromolecular architectures such as stars,^{30,31} combs,²⁸ and dendrimers,^{32,33} research in this field has not been widely commercialized.

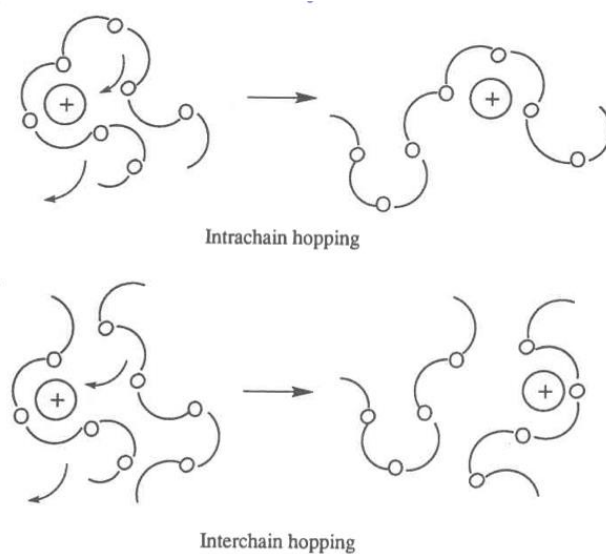


Figure 1.6 Intrachain (top) and interchain (bottom) hopping of ions facilitated by segmental motion of polymer chains.³⁴

1.1.6 Hybrid Electrolytes and Other Systems

The disadvantages presented in each type of homogeneous electrolyte have led to the development of hybrid or composite materials aimed to simultaneously mitigate the limitations and combine the benefits of individual components. As a result, crosslinked polymer matrices are frequently swelled with organic carbonate solutions or ionic liquids (also known as gel electrolytes). Often, however, the drawbacks of each constituent are still observed. For example, organic carbonate additives are added to polymer matrices to increase ionic conductivity, but produces compositions that are still considered flammable (Table 1.1).²⁷

Table 1.1 Example of hybrid electrolytes, as reported by Kim and coworkers in Chemistry of Materials.²⁷

Hybrid electrolyte	Ionic conductivity	Limitation
Organic liquid + polymer ³⁵	4.2×10^{-3} S/cm	Flammable
Ionic liquid + polymer ³⁶	0.18×10^{-3} S/cm	Less flammable
Ionic liquid + polymer + organic liquid ³⁷	0.81×10^{-3} S/cm	Less flammable

1.2 Perfluoropolyethers

The development of polytetrafluoroethylene (PTFE) has since garnered heavy interest in perfluoro- or polyfluoro- alkyl compounds; due to the strength of C-F chemical bonds, these materials are widely known to be chemically and thermally inert. Within this family, perfluoropolyethers (PFPEs) are an interesting subgroup, as they combine the typical properties of fluorinated organic compounds with unusual properties such as low T_g , low viscosity, low refractive index and high gas permeability.³⁸ Although herein we will primarily focus on linear hydroxy-terminated PFPEs and its derivatives, branched PFPEs and PFPEs with a wide range of fluorinated end group moieties also exist and are commercially available (Figure 1.7).

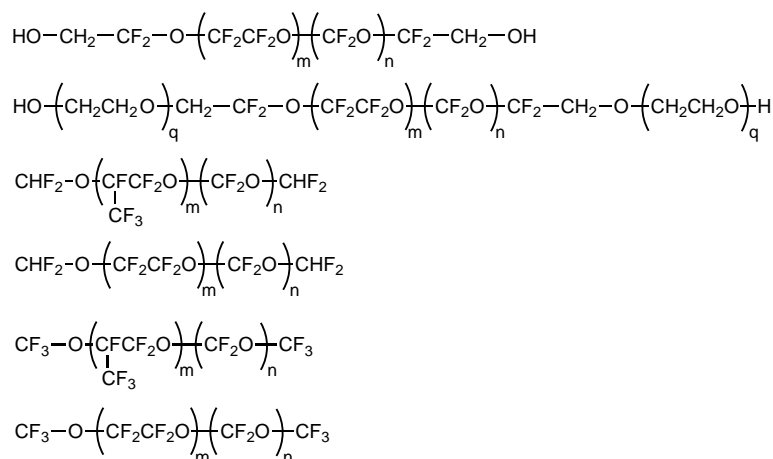


Figure 1.7 Different types of branched and linear PFPEs with various end group functionalities.

1.2.1 Methods Used to Synthesize PFPEs

1.2.1.1 Anionic Ring Opening Polymerization of Hexafluoropropylene Oxide

PFPEs are commonly synthesized by anionic ring-opening polymerization of hexafluoropropylene oxide (HFPO).³⁹ Cesium fluoride (CsF) was reported to be the most effective source of fluoride anions because of its low lattice energy and highly ionic nature. However, in order to facilitate the formation of active fluoride ions, strongly coordinated solvents must be used, tetraglyme (TG) is therefore frequently used in conjunction to complex cesium cations in order to generate free fluoride ions. The fluoride ions subsequently react with HFPO monomers to initiate the reaction (Figure 1.8). Chain transfer reactions are the predominant reactions under these conditions, and as a result only low molar mass PFPE oligomers are produced using this method.³⁹⁻⁴¹

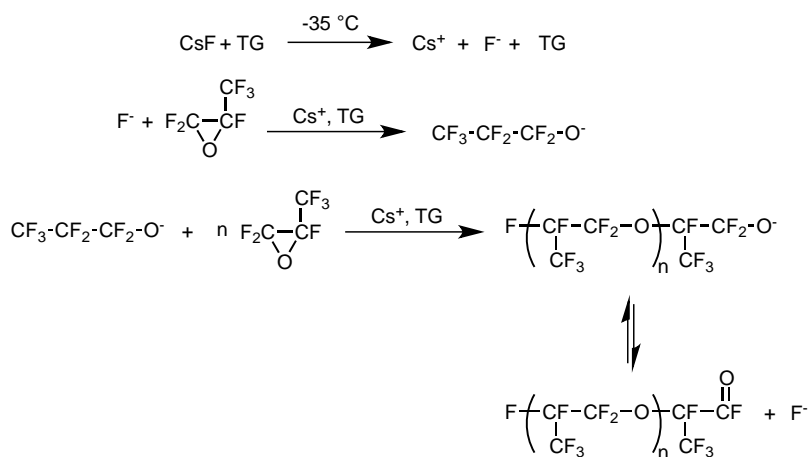


Figure 1.8 Anionic ring opening of HFPO in the presence of CsF and TG.⁴⁰

1.2.1.2 Direct Fluorination

The Lewis acid-catalyzed ring opening polymerization of 2,2,3,3-tetrafluorooxetane to synthesize PFPEs was first industrialized by Daikin Industries. 2,2,3,3-tetrafluorooxetane was first prepared from tetrafluoroethylene (TFE) and paraformaldehyde. Initiated by a fluoride ion, typically from CsF, 2,2,3,3-tetrafluorooxetane is subsequently polymerized in a nonprotic polar solvent like TG to produce a polyfluorinated polymer. The polymers are then treated with fluorine gas for direct fluorination of the hydrogen atoms in the backbone; this process is accelerated by ultraviolet (UV) irradiation (Figure 1.9).^{42,43}

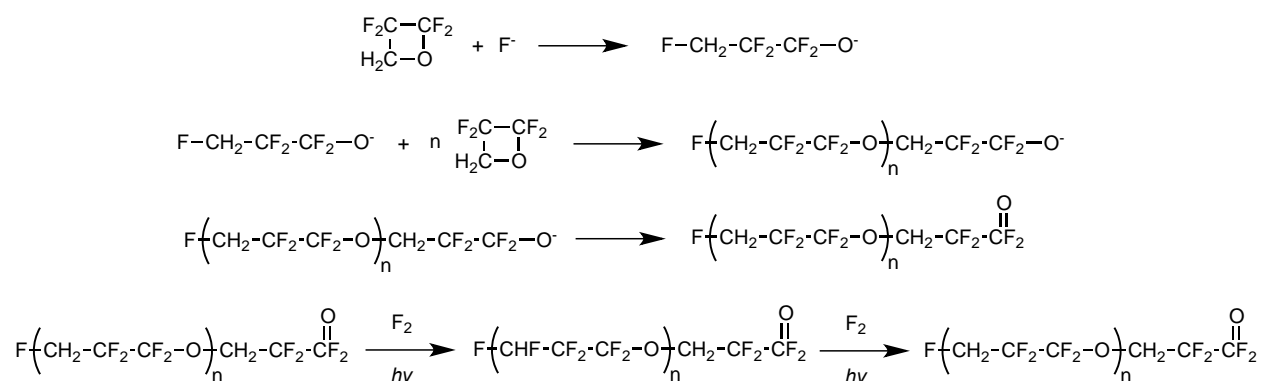


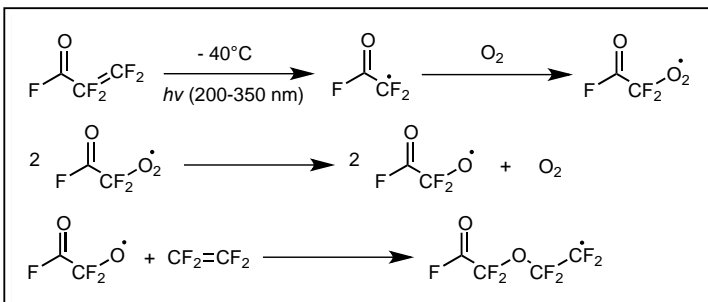
Figure 1.9 Lewis acid catalyzed ring opening polymerization of 2,2,3,3-tetrafluorooxetane following by direct fluorination under UV light.³⁹

Similarly, Lagow and coworkers⁴⁴⁻⁴⁶ developed a PFPE synthetic technique by direct fluorination of hydrogenated polyethers.³⁹ Known as the ‘LaMar’ process, this method involves a cryogenic reactor, and allows a vast range of perfluorinated compounds to be prepared using low concentrations of fluorine.^{42,47}

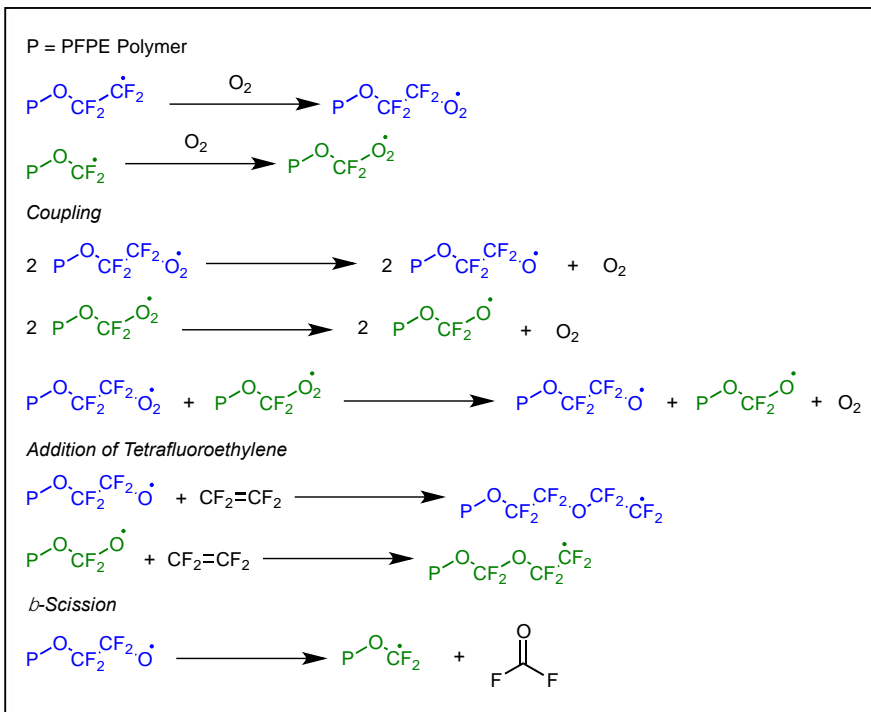
1.2.1.3 Photooxidation

The synthesis of PFPEs through photo-oxidative polymerization was first patented by Solvay Solexis.⁴⁸ In general, TFE is polymerized at low temperatures in a controlled partial pressure of oxygen gas (Figure 1.10). Initiator radicals are produced by exposing allyl acyl fluorides to ultraviolet light within the wavelengths of 200 to 350nm at -40°C. Polymerization propagation consists of rotating processes of oxygen gas (O₂) addition, coupling of two alkoxy radicals that releases O₂, and addition of TFE. Inevitable β-scission side reactions of perfluoro-ethoxy radicals, favored in higher temperatures, produce perfluoro-methoxy radicals and carbonyl fluoride. This results in random insertions of perfluoromethoxy units along the backbone of PFPE polymers. The propagating radicals are considered terminated when alkoxy radicals couple to produce interior peroxy units. Termed peroxidic perfluoropolyethers, the polymer chains are cleaved thermally or through catalytic reduction to produce the PFPE material functionalized with acyl fluorides on both terminal ends. Subsequent reactions of these highly reactive terminal groups allow for PFPEs to be functionalized with a variety of chemical moieties including hydroxyl groups.⁴⁹ Relative concentrations of initiator, oxygen, and tetrafluoroethylene are used to control and tune the average molecular weight of the final polymer; fluorine gas is also oftentimes used. Ratios of perfluoromethylether to perfluoroethylether repeating units using this method generally range from 0.5 to 3.0.^{48,49}

Initiation



Propagation



Termination

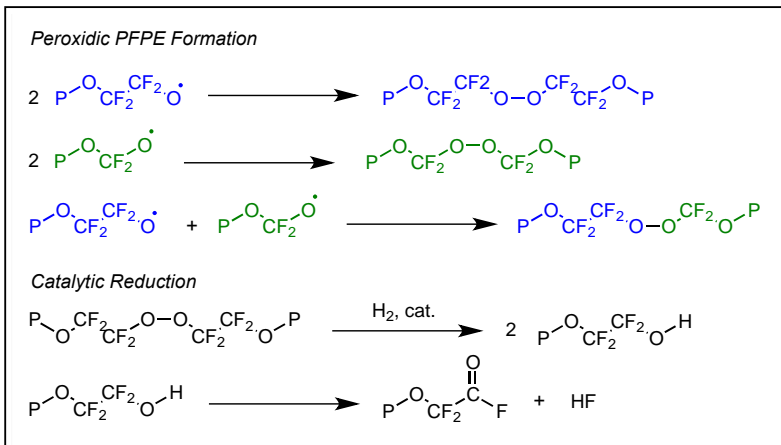


Figure 1.10 Synthetic schemes outlining the initiation, propagation, and termination of PFPE polymerization.⁴⁹

Our group has also previously developed a synthetic method for PFPEs through the photooxidation of HFP in liquid carbon dioxide. This strategy provides an environmentally friendly alternative to organic and fluorinated solvent systems such as dichlorodifluoromethane and exploit the benefits of utilizing an environmentally friendly and tunable continuous phase.^{39,50,51}

1.2.2 PFPE Uses and Applications

PFPEs are traditionally used as high performance lubricants and greases due to their favorable properties and stability even against extreme conditions. They are liquid at room temperature, as their aliphatic and ether linkages result in a totally amorphous morphology.³⁹ In addition to their nonflammable and chemical stability properties, PFPEs exhibit high viscosity indexes (approximately 350 (unitless)), low vapor pressure (less than 4×10^{-13} torr at 20 °C), and low surface tension (approximately 20 dyn/cm at 20 °C). The useful temperature range of PFPEs is also generally wider than mineral oils and polyol esters (Figure 1.11). For these reasons, typical applications of PFPEs in industry include aircraft instrument bearing grease, automotive braking systems, astronaut space suit bearing and breathing apparatus lubricants. In addition, PFPEs are frequently used lubricants in oxygen and reactive gas service applications, where conventional lubricants are unsuitable due to their reactivity with oxygen and halogens like chlorine, increasing the potential for explosion, fire and premature deterioration.^{52,53}

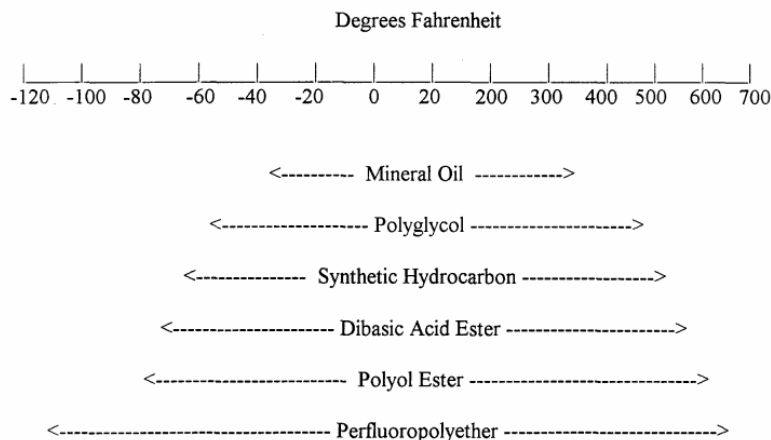


Figure 1.11 Temperature range of use of PFPEs relative to other lubricants and oils.⁵³

Academic research focusing on PFPEs has also expanded its potential applications; current efforts explore the use of PFPE-based materials in the fields of soft lithography, microfluidics (Figure 1.12),^{54,55} cosmetics,⁵⁶ fuel cells,⁵⁷ and biomedical corneal implants. For example, our group had previously reported in 2004 the first fabrication of a solvent compatible microfluidic device based on photocurable PFPE materials. These devices exhibit similar mechanical properties to polydimethylsiloxane (PDMS) systems based on Sylgard 184 from Dow Corning but swell significantly less and are more resistant to aqueous and organic solvents including water, toluene, methanol, and dichloromethane.⁵⁸ This makes PFPE-based devices more suitable for carrying out combinatorial chemical reactions and syntheses of polymers and oligonucleotides that require an organic phase. The moldability of photocurable PFPEs also resulted in increased development in patterning nanoscale inorganic oxide surfaces such as titanium oxide (TiO₂), tin oxide (SnO₂) and zinc oxide (ZnO)⁵⁹ as well as patternable biomaterials for cell culture and tissue engineering⁶⁰ using soft lithography methodologies.

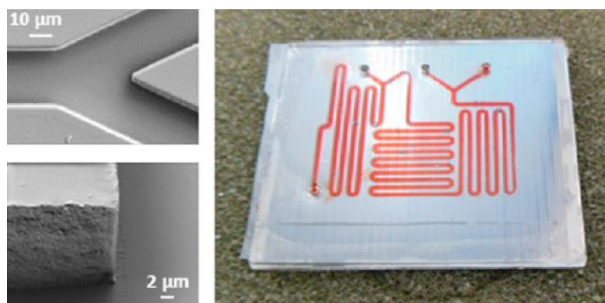


Figure 1.12 Microchannel section and sidewall of PFPE microfluidic device (left); PFPE device filled with colored water-based solution (as reported by Bongiovanni and coworkers in *Langmuir*).⁵⁴

The hydrophobicity and inertness of PFPE elastomers have also garnered interest in their uses as antibacterial⁶¹ and antifouling coatings for biomedical and marine applications. Our group has done extensive work in this regard.⁶² In 2009, Hu, DeSimone and coworkers reported that PFPE-based coatings fabricated from 4 kg/mol distyrenyl-modified PFPE macromolecules (sPFPE) and fluorinated styrenesulfonic ester monomers (SS) exhibit substantially lower settlement densities of *Ulva* spores than PDMS standards (Figure 1.13).⁶³ Furthermore, in a separate report, Hu, DeSimone and coworkers presented the surprising miscibility between hydrophobic PFPEs and hydrophilic low molar mass PEG, ultimately producing copolymerized amphiphilic networks (Figure 1.14).⁶⁴ This further widens the versatility of PFPEs and enhances the foulant releasing properties of the coating. Previous reports have claimed that a segregated surface with amphiphilic surface properties can successfully resist biofilm formation by presenting a rather ‘ambiguous’ surface to the protein or glycoprotein adhesives secreted by colonizing organisms. Indeed, the density of *Ulva* diatom cells was lower on surfaces composed of PFPE physically blended with PEG of molar mass of 300, 475, and 1100 g/mol respectively than coatings of pure PFPE (Figure 1.15).⁶⁵

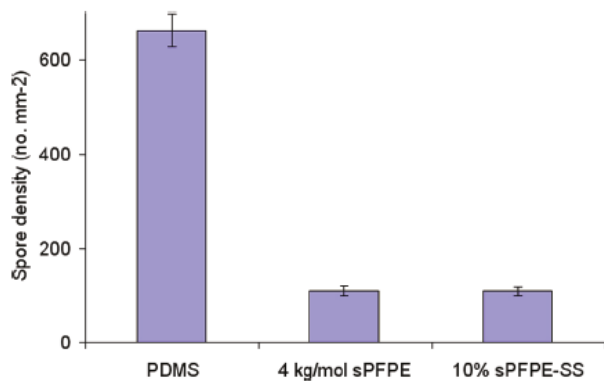


Figure 1.13 Density of attached spores of *Ulva* on PDMS and PFPE elastomers containing sPFPE and PFPE with 10% SS after a 1h settlement period, as reported by DeSimone and coworkers in *Macromolecules*. Bars show 95 % confidence limits.⁶⁶

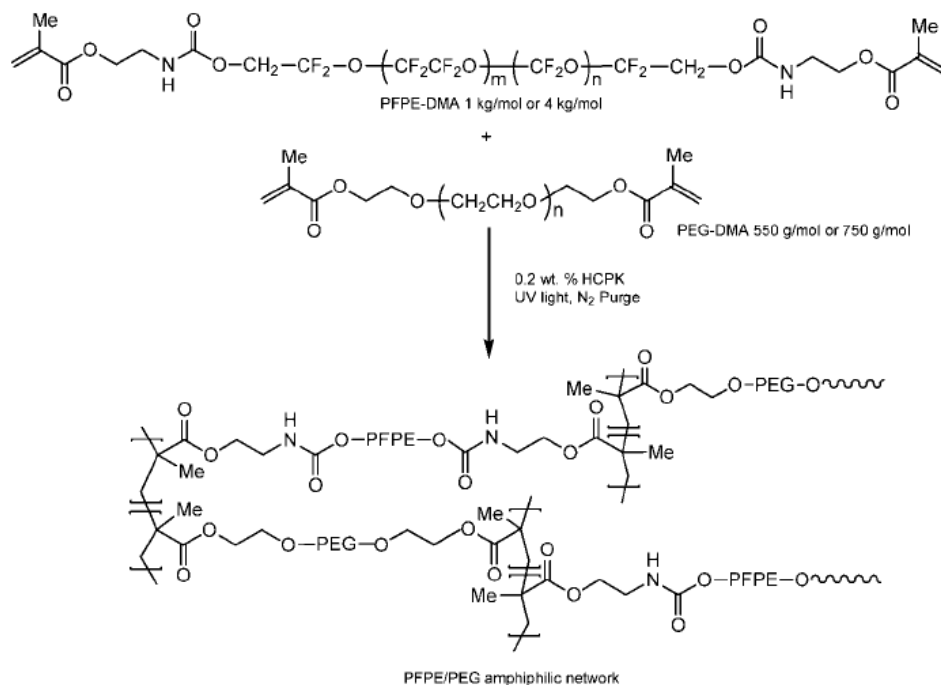


Figure 1.14 Synthetic scheme of PFPE/PEG networks via a precursor approach, as reported by DeSimone and coworkers in *the Journal of the American Chemical Society*.⁶⁴

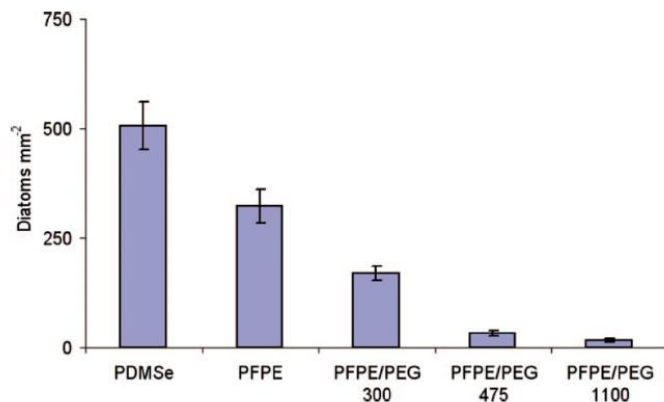


Figure 1.15 Final density of attached diatoms on PFPE/PEG coatings. Bars show 95% confidence limits, as reported by DeSimone and coworkers in *Biofouling*.⁶⁵

1.3 Techniques for Electrolyte Characterization

1.3.1 Physical and Thermal Characterization

For electrolytes, important physical and thermal properties include degree of lithium salt dissolution, thermal stability, and viscosity. Lithium salt dissolution is commonly measured qualitatively through visual observation (solubility frequently leads to production of clear colorless solutions) or quantitatively using mass spectroscopy. On the other hand, thermal stability and viscosity require more analytical experimentation. Thermal stability, an important indication of a material's robustness, against a wide range of temperatures when incorporated into a full battery, is usually characterized using thermogravimetric analysis (TGA) and differential scanning calorimetry (DSC) methodologies. In addition to these two techniques, electrolyte flammability is also characterized through a variety of methods.

1.3.1.1 Thermogravimetric Analysis

TGA is a common materials analysis technique used to study physical processes such as second-order phase transitions like vaporization or sublimation as well as chemical processes such as decomposition and oxidation. Experimentally, a typical TGA systems measure the

amount and rate of change in a sample's mass as a function of temperature or time in a controlled rate and atmosphere. Because materials tend to experience sample weight loss as a result of degradation or evaporation, changes in initial measured mass indicate valuable information regarding the stability, purity, and composition of materials. For example if a material that exhibits negligible or no mass change between 50 and 200 °C, this indicates that it is thermally stable within that temperature range. Furthermore, TGA is able to determine compositional analysis of blends or multicomponent samples based on the known characteristic vaporization temperatures of pure components.⁶⁷

1.3.1.2 Different Scanning Calorimetry

Similarly, DSC is a fundamental physical characterization method used to study the thermal behavior of materials.⁶⁸ One of the most important tools of DSC techniques is the determination of the first and second order transitions in polymers, which corresponds to the T_m (and T_c), and T_g respectively.

Experimentally, a typical DSC experiments treats a small quantity of sample enclosed in a pan to a controlled temperature program, pressure and atmosphere and monitors heat effects relative to a reference sample. The reference is usually an inert material or empty pan made out of aluminum. The different in heat flow, that is, the heat absorbed by the material in a unit of time $\left(\frac{dH}{dt}\right)$, is then monitored as the temperature of both the sample and the reference changes at a constant rate. In other words:⁶⁹

$$\Delta \frac{dH}{dt} = \left(\frac{dH}{dt}\right)_{sample} - \left(\frac{dH}{dt}\right)_{reference} \dots\dots\dots\text{equation 1.3}$$

The difference in heat flow can be positive or negative depending on whether the thermal phase transition is endothermic or exothermic. Therefore, endothermic processes like melting

and exothermic processes like crystallization result in a sudden positive and negative difference in heat flow respectively. On the other hand, second order processes such as glass transitions result in a broader increase or decrease in heat flow difference due to changes in the polymer's heat capacity below and above T_g (Figure 1.16).

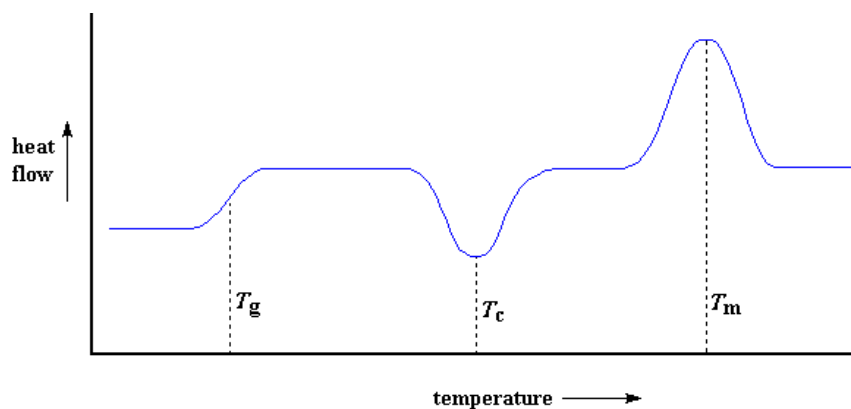


Figure 1.16 Sample DSC curve illustrating the T_g , T_c and T_m of a sample.⁷⁰

1.3.1.3 Flammability Tests

In order to determine the flammability of electrolytes, a variety of flame tests can be used; literature reports methods spanning from standardized flash point^{71,72} and sustained burning tests⁷² to customized ignition test set ups^{15,18} (Figure 1.17). For example, an instrument in accordance to the American Society of Testing and Materials (ASTM) is commonly used; Figure 1.18 is a schematic of an apparatus used to measure sustained burning of liquid materials in an open cup at a controlled temperature and pressure, a protocol known as ASTM D4206.⁷³ On the other hand, custom-built set ups commonly forego the use of an instrument and quantify flammability by describing thermal responses when a material is exposed to flame and measuring the duration in which the material burns once ignited.

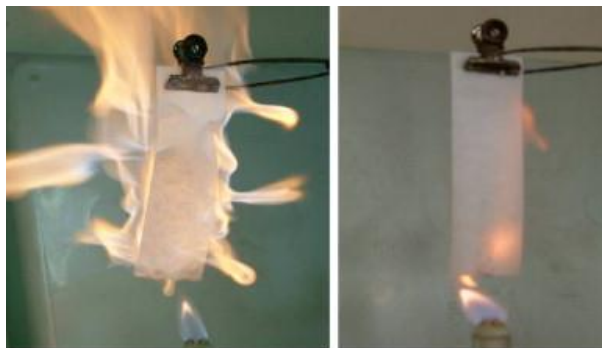


Figure 1.17 Example of a customized ignition test involving exposing a flame to an electrolyte-soaked membrane.⁷⁴

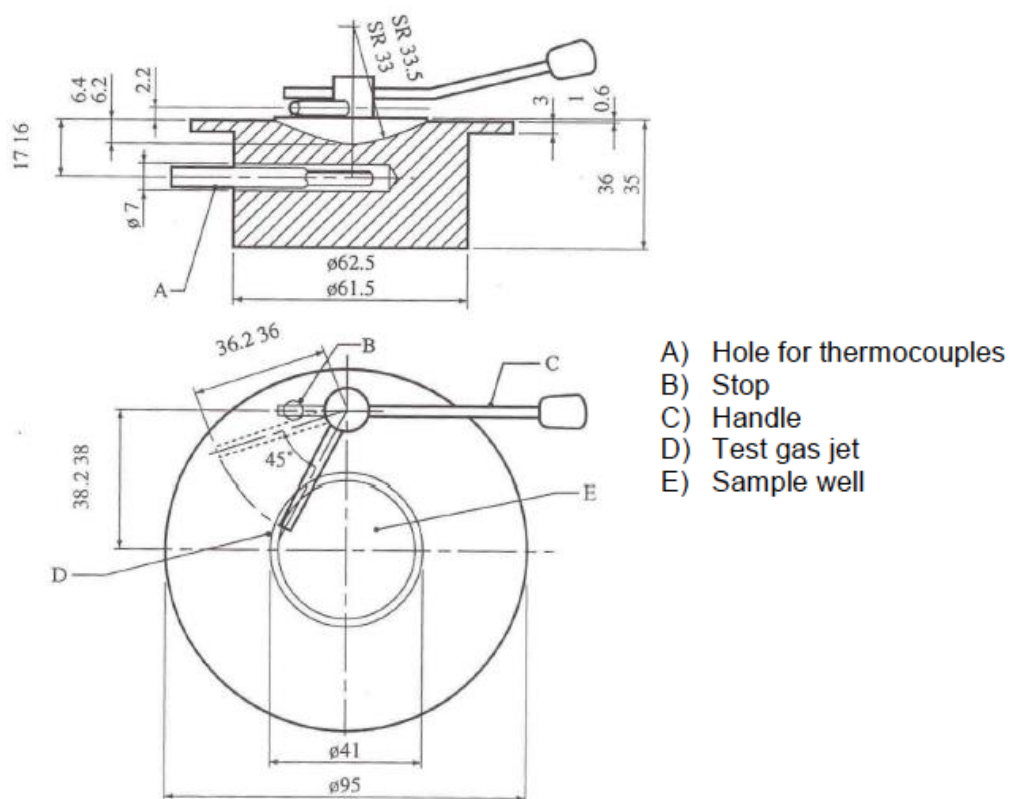


Figure 1.18 Sample apparatus of sustained burning test in accordance with ASTM D4206.⁷³

1.3.1.4 Viscosity

An electrolyte's viscosity, η , is an important parameter due to its relationship to ionic conductivity and its impact on battery assembly. It is generally believed that viscosity is related to ionic conductivity through the Nernst-Einstein and Stokes-Einstein equations:

$$\sigma = \frac{ne^2D}{kT} \dots\dots\dots\text{equation 1.4}$$

$$D = \frac{kT}{6\pi r\eta} \dots\dots\dots\text{equation 1.5}$$

where n is the number density of charge carriers, e is the electronic charge, k is the Boltzmann's constant, T is the temperature, D is the diffusion coefficient, and r is the effective radius of the diffusing species. Therefore, low viscosity materials tend to result in higher conductivity due to enhancement of Li-ion diffusion and migration.⁷⁵

Understanding viscosity behavior of electrolytes is also crucial in determining wetting time in the assembly of full batteries. Electrodes must be fully wetted with the electrolyte in order to achieve full electrode capacity potential. Insufficient time allotted for viscous electrolytes to wet the electrode surface tends to deteriorate Li-ion battery performance and shorten battery cycle life.⁷⁶ Conventional small molecular alkyl carbonates exhibit dynamic viscosities as low as 1.7 - 3.0 cP at 25 °C.⁷⁷

Although the glass capillary viscometer is traditionally one of the most common instruments used to measure kinematic viscosity (related to dynamic viscosity through the sample's density), the use of advanced rotational rheometers is becoming increasingly popular.

1.3.2 Characterization of Elastomers

Mechanical stability, or a material's ability to withstand mechanical deformation and stress, is not only important for solid-state electrolytes in wearable and flexible batteries, but also affects dendrite growth in electrolyte-electrode interfaces; studies have shown that the appropriate electrolyte stiffness and compressibility (approximately 10^9 Pa)⁷⁸ are crucial in suppressing detrimental lithium dendritic formation that reduces cycle life of batteries.⁷⁹ The tensile strength of materials, measured by a tensile test, is commonly characterized by stress-

strain curves as well as the determination of the Young's Modulus, E . The process involves applying a controlled force to elongate a test specimen along a direction until it fractures. The measured elongation is used to calculate the engineering strain, ϵ , using the equation:

$$\epsilon = \frac{L-L_0}{L_0} \dots \dots \dots \text{equation 1.6}$$

where L and L_0 is the final and initial length respectively. In response to an applied force, the engineering stress, σ , is determined with the equation:

$$\sigma = \frac{F_n}{A} \dots \dots \dots \text{equation 1.7}$$

where F_n and A is the tensile force and cross-sectional area of the sample respectively.⁸⁰

Measured stress and strain points are graphed into stress-strain curves (Figure 1.19). The

Young's modulus, or tensile modulus, a properties used to characterize stiffness, is subsequently calculated using the equation:

$$E = \frac{\sigma}{\epsilon} \dots \dots \dots \text{equation 1.8}$$

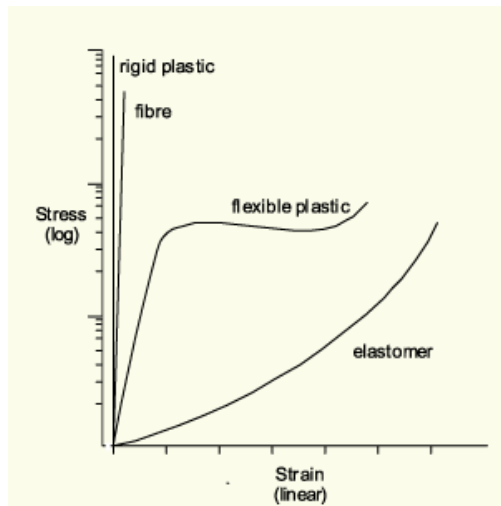


Figure 1.19 Stress strain plot and characteristic curves of rigid plastics, fibers, flexible plastics, and elastomers.⁸¹

1.3.3 Electrochemical Characterization

Extensive electrochemical characterization describes the behavior of an electrolyte and dissolved lithium salt in the presence of voltage and probes an electrolyte's short- and long- term viability as a reliable component of marketable Li-ion batteries. Important properties range from ionic conductivity and capacitance retention in batteries to more complex understanding of ion movement through Li-ion transference numbers.

1.3.3.1 Ionic Conductivity

Ionic conductivity, σ , is one of the most extensively studied properties for electrolytes for Li-ion batteries. It is a measure of an electrolyte's ability to conduct electricity and the mobility and speed of ions through the media. Sufficient ionic conductivities over wide temperature ranges must be achieved in order to obtain practical battery performance for portable electronics and transportation applications. Currently, state-of-the-art carbonate-based electrolytes exhibit ionic conductivities on the order of 3.4 – 11.1 mS/cm.⁷⁷

Ionic conductivity is determined by measuring the resistance, R , between two electrodes at a fixed distance, then calculated using the equation:

$$\sigma = \frac{L}{R \cdot A_{eff}} \dots \dots \dots \text{equation 1.9}$$

where L and A_{eff} is the length of electrode separate and effective cross-sectional area respective.

Since practical electrochemical processes exhibit complex behavior and responses in the presence of an applied potential, electrochemical impedance spectroscopy (EIS) is commonly used technique to measure resistance in non-ideal systems. Impedance similarly measures a circuit's ability to resist current flow, but eliminates simplifying assumptions such as frequency independence of resistance and consistency with Ohm's Law at all current and voltage levels.⁸²

The theory and concepts regarding EIS has been extensively reported and will not be covered

here; however it is important to note that potentiostats display EIS behavior in the form of Nyquist plots (Figure 1.20), from which resistance can be extracted from the x-intercept of the lowest radial frequency.

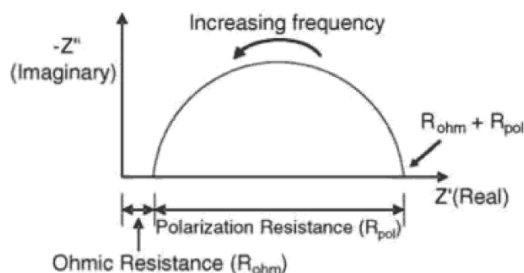


Figure 1.20 Sample Nyquist plot obtained from EIS.⁸³

1.3.3.2 Electrochemical Window

The electrochemical window of an electrolyte is an important parameter that indicates the stability and compatibility of that material against different cathodes and anodes. Commonly measured using cyclic voltammetry (CV) or linear sweep voltammetry, an electrochemical window represents the highest occupied molecular orbital and lowest unoccupied molecular orbital (also known as the HOMO and LUMO respectively) of a compound. Cathodes and anodes with potentials above and below the electrolyte's HOMO and LUMO respectively will not be well suited for the electrolyte. For example, if a cathode material exhibits a potential above the HOMO of the electrolyte, electron transfer from the electrolyte to the cathode will occur during battery cycling, leading to irreversible oxidation of the electrolyte and ultimately electrolyte degradation.²⁷ Novel electrolytes must therefore demonstrate an electrochemical window that is sufficiently wide enough to accommodate the oxidation and reduction potentials of different electrode materials. Researchers have addressed this challenge by including additives in the electrolyte that can develop a rapid solid electrolyte interface (SEI) layer during a fast first charge of the battery to prevent detrimental electrolyte breakdown. However, although the

formation of the SEI layer is commonly deemed a vital process in batteries, it oftentimes lack in film thickness consistency and structure homogeneity throughout the battery, ultimately and inevitably leading in an increase in cell internal impedance over time, causing reduction in capacity and cycle life.⁸⁴

1.3.3.3 Battery Performance

If an electrolyte exhibits practical ionic conductivity, the material can be coupled with electrodes and a separator in an assembled battery cell for further battery testing; the construction and components of a coin cell battery is shown in Figure 1.21. Characterization of Li-ion cells usually involves galvanostatic charges and discharges at various cycles and charge rates. During galvanostatic cycling, cells are cycled within a potential range depending on the electrochemical and redox stability of the electrolyte and electrodes. Charges and discharge current is often expressed as the charge rate or C-rate, calculated from the theoretical energy capacity of the electrodes; the C-rate is a measure of the rate required for a cell to be charged or discharged and the maximum capacitance achievable at that rate.⁸⁵ For example, a C-rate of 20 C indicates the necessary current applied or drained from the cell in order to completely charge or drain in 20 hours (Figure 1.22).

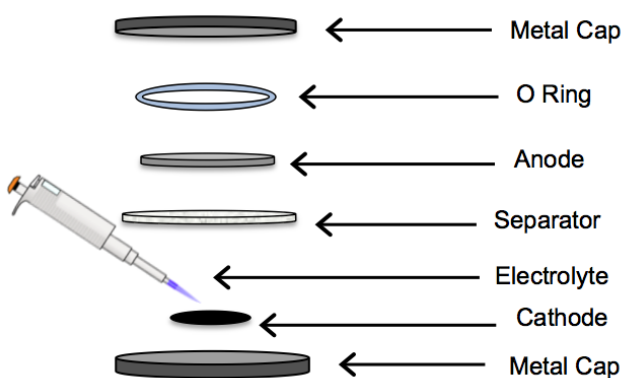


Figure 1.21 Components of an assembled battery coin cell.

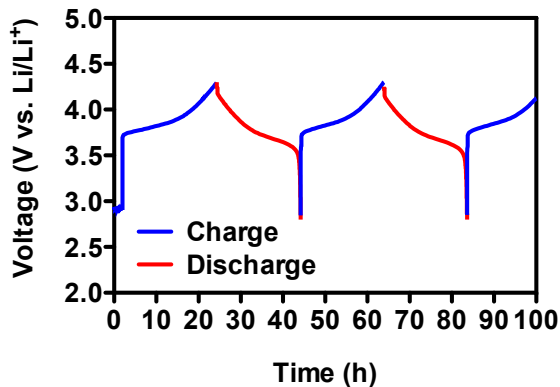


Figure 1.22 Sample galvanostatic cycling of a battery cell between 2.75 V and 4.25 V at a C-rate of 20 C.

1.3.4 Lithium-Ion Transference Number

Full electrochemical characterization of battery electrolytes would not be complete without a measure of charge transport, which includes determination of ion transference numbers, also known as t^+ . Only Li-ions are pertinent to cell charge and discharge; however, ionic conductivity measurements include mobility of both ionic species, the Li-ion and its counterion, Li-ion transference numbers are a more specific property that is defined as the contribution of total ionic conductivity that originates solely from Li-ions. In other words, it is the fraction of current contributed by the mobility of Li-ions, and is therefore a value between 0 and 1.

The concept of t^+ 's is important when considering the long-term performance of a battery cell. Electrolytes exhibiting low t^+ 's cause concentration gradients of the lithium salt to develop over time, which ultimately leads to poor high-rate performance and limitations in cell power output.⁸⁶ In fact, studies have suggested that electrolytes exhibiting high t^+ 's are far superior in applications that require a high discharge rate than electrolytes with low t^+ 's, even when the conductivity of the materials is reduced by over an order of magnitude.⁸⁷ Li-ion t^+ 's closest to unity, are therefore highly desired.

Four acceptable techniques for t^+ measurements exist in the literature for nonaqueous electrolytes: the potentiostatic polarization method, galvanostatic polarization method, electromotive force method, and pulsed-field gradient (pfg) NMR method.

1.3.4.1 Lithium-Ion Transference Number Using Pulsed Field Gradient NMR

Pfg-NMR is an experiment in the family of diffusion NMR techniques used to characterize long-range translational motion of a molecular or ionic species. This method couples radio-frequency pulses used in conventional NMR experiments with magnetic field gradients to extract spatial information along the Z-direction of the sample tube.⁸⁸ The concepts and theory regarding NMR and pfg-NMR is well studied, and will therefore not be described extensively herein. In brief, a typical pfg-NMR experiment involves application of a series of pulses at increments of increasing gradient strength and recording the intensity of the signals of interest as a function of magnetic field gradient strength (Figure 1.23).

Using intensity information from diffusion spectra, a plot of intensity as a function of gradient strength can be plotted (Figure 1.24). Diffusion can then be calculated by fitting the plot curve using the equation:⁸⁹

$$I = I_0 e^{-D\gamma^2 g^2 \delta^2 (\Delta - \frac{\delta}{3})} \dots \dots \dots \text{equation 1.10}$$

where I is the observed intensity, I_0 is the reference intensity, D is the diffusion coefficient, γ is the gyromagnetic ratio of the observed nucleus, g is the gradient strength, δ is the length of the gradient and Δ is the diffusion time.

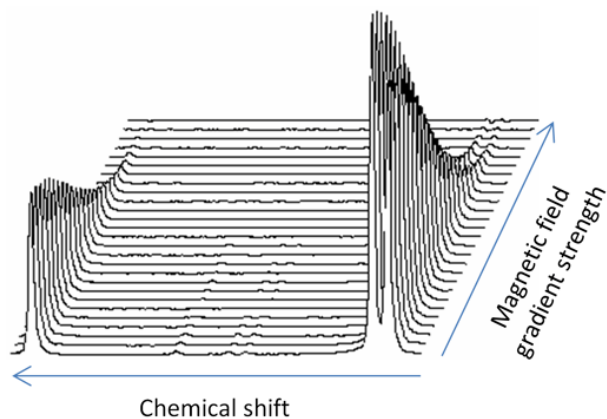


Figure 1.23 Sample diffusion spectrum of two signals decaying in intensity as magnetic field gradient strength increases.⁹⁰

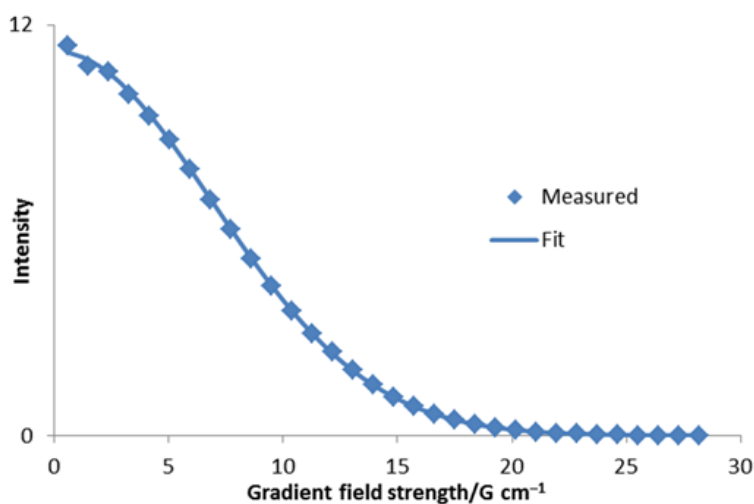


Figure 1.24 Sample plot of diffusion peak intensity as a function of gradient field strength.⁹⁰

The t^+ is ultimately calculated from determination of t^+ for both the lithium cation and counterion, and is described as

$$t^+ = \frac{D_+}{D_+ + D_-} \dots \dots \dots \text{equation 1.11}$$

where D_+ and D_- is the self diffusion coefficient of the cation and anion respectively. It is important to note that transference number measured using pfg-NMR methods tend to overestimate the t^+ value relative to the three other methods. This is because NMR detects both ion pairs and free ions independent of species charge. For this reason, pfg-NMR measurements

increase in accuracy only in dilute samples of lithium salt in the electrolyte. Alternatively, methods have been developed to determine the degree of salt dissociation and decouple measure diffusion coefficients from neutral ion pairs from solvated lithium ionic species.^{86 91,92} More details regarding pfg-NMR experiments are discussed in Chapter 5.

1.3.4.2 Other Methods of Measuring Li-ion t_+ 's

As previously mentioned, the other methods of measuring Li-ion t^+ 's in addition to pfg-NMR are the potentiostatic polarization method, galvaostatic polarization, and electromotive force method.

1.3.4.2.1 Potentiostatic Polarization

The potentiostatic polarization method, first reported by Dr. Peter Bruce and Dr. Colin Vincent, was developed to measure cationic t^+ 's in ideal solid polymer electrolytes.^{86,93} However, this method is also suitable for liquid solutions with diluted concentrations of lithium salt.^{86,94} In brief, the concept behind this method is to establish an electrochemical steady-state within a cell composed of the electrolyte of interest and two lithium metal electrodes. Application of a small constant potential on the electrolyte results in a decrease of the initial current value until a steady-state value is reached. In the absence of redox reactions, the current contributed by the anion will diminish in the steady-state, leaving behind current only contributed by the cations.⁹³ The t^+ of the electrolyte can then be calculated by the fraction of steady-state cationic current in the initial total current:^{86,95}

$$t^+ = \frac{I_{SS}(\Delta V - I_0 R_0)}{I_0(\Delta V - I_{SS} R_{SS})} \dots \dots \dots \text{equation 1.12}$$

where I_{SS} is the steady-state current, I_0 is the initial current, ΔV is the applied potential, R_0 is the electrode resistance before polarization, and R_{SS} is the steady-state resistance after polarization.

The potentiostatic method is a relatively quick measurement, but is restricted to dilute samples and binary electrolytes (only one cationic and anionic species).

1.3.4.2.2 Galvanostatic Polarization

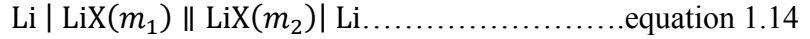
In 1995 Dr. John Newman and coworkers established a procedure using galvanostatic polarization for polymer electrolytes with concentrated lithium salt. This method combines three different parameters to calculate the t^+ : (i) the cell potential after galvanostatic polarization, (ii) salt diffusion coefficient, and (iii) concentration dependence of the potential difference. The cationic t_+ can then be calculated through the equation:^{86,96,97}

$$t^+ = 1 - \frac{mFc_\infty\sqrt{\pi D}}{4(d\Phi/d\ln c)} \dots\dots\dots \text{equation 1.13}$$

where c_∞ is the bulk salt concentration, F is the Faraday constant, D is the salt diffusion coefficient, $d\Phi/d\ln c$ is the concentration dependence of the potential Φ and m is the slope of the plot of cell potential as a function of current density and polarization time. Although this method is relatively more accurate than the potentiostatic polarization method and is capable of measuring concentrated electrolytes, the determination of three separate parameters is often time consuming.

1.3.4.2.3 Electromotive Force Method

The electromotive force method measures the transference number through determination of the diffusion potential (also known as the liquid junction potential) of an electrolyte and involves the use of an electrolytic cell composed of two half-cells with the same electrodes, but in different lithium salt concentrations (also known as a concentration cell). For example, a concentration cell with an electrolyte of interest and two lithium metal electrodes could be described as



where LiX is the lithium salt in the electrolyte, and m_1 and m_2 are different salt concentrations, commonly expressed in molalities (mol/kg).⁸⁶ In such concentration cell, the potential difference E_{trans} is described as

$$E_{\text{trans}} = -\frac{2RT}{F} t_- \ln \frac{m_2}{m_1} \dots \dots \dots \text{equation 1.15}$$

where R is the ideal gas constant, T is the temperature, F is the Faraday constant, and t_- is the anionic transference number for the lithium counterion in the electrolyte.⁸⁶ Following several measurements of the potential difference at various concentrations, a salt bridge is applied to the concentration cell between the sample solution and reference electrode, reducing the diffusion potential close to zero.⁹⁸ The resulting potential E is therefore

$$E = -\frac{2RT}{F} \ln \frac{m_2}{m_1} \dots \dots \dots \text{equation 1.16}$$

From the previous two equations t^- can be calculated as

$$t^- = \frac{dE_{\text{trans}}}{dE} \dots \dots \dots \text{equation 1.17}$$

t^- can then be interpreted as the slope of a plot of E_{trans} as a function of E at different lithium salt concentrations (Figure 1.25). From determination of t^- the cationic t^+ can then be simply calculated as $1 - t^-$.⁸⁶ One of the biggest limitations of this method is the assumption that the transference number is constant within the measured salt concentration range. This assumption is not always true.⁸⁶

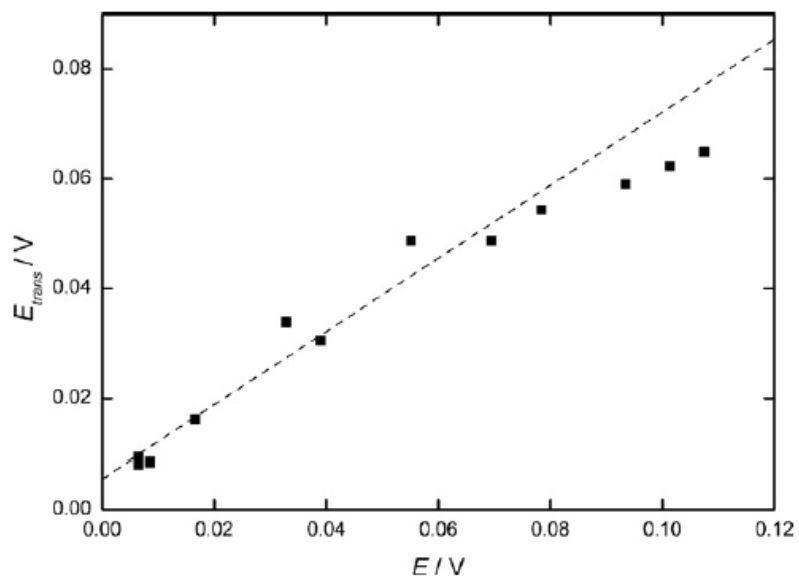


Figure 1.25 Sample E_{trans} vs. E plot produced by the electromotive force method for an EC/DEC electrolyte, as reported by Gores and coworkers in *Electrochimica Acta*.⁸⁶

REFERENCES

- (1) Carella, C. In *Frost & Sullivan* London 2013.
- (2) Mizushima, K.; Jones, P. C.; Wiseman, P. J.; Goodenough, J. B. *Materials Research Bulletin* **1980**, *15*, 783.
- (3) Tarascon, J. M.; Armand, M. *Nature* **2001**, *414*, 359.
- (4) O'Dell, J. In *Green Car Advisor* 2008.
- (5) Loveday, E. In *Green Car Advisor* 2010.
- (6) Bulkeley, W. M. In *The Wall Street Journal* 2005.
- (7) Newman, J. In *Time* 2013.
- (8) Anthony, S. In *ExtremeTech* 2014.
- (9) Brain, M. <http://electronics.howstuffworks.com/everyday-tech/lithium-ion-battery.htm>, 2006.
- (10) Hammami, A.; Raymond, N.; Armand, M. *Science* **2003**, *301*, 635.
- (11) Mandal, B. K.; Padhi, A. K.; Shi, Z.; Chakraborty, S.; Filler, R. *Journal of Power Sources* **2006**, *161*, 1341.
- (12) Cooper, A. In *CNN* 2013.
- (13) In *BBC News* 2014
- (14) Stibbe, M. In *Forbes* 2013.
- (15) Wu, L.; Song, Z.; Liu, L.; Guo, X.; Kong, L.; Zhan, H.; Zhou, Y.; Li, Z. *Journal of Power Sources* **2009**, *188*, 570.
- (16) Granzow, A. *Accounts of Chemical Research* **1978**, *11*, 177.
- (17) Zhang, S. S. *Journal of Power Sources* **2006**, *162*, 1379.
- (18) Xu, K.; Ding, M. S.; Zhang, S.; Allen, J. L.; Jow, T. R. *Journal of The Electrochemical Society* **2002**, *149*, A622.
- (19) Feast, W. J.; Tweedale, P. J. *British Polymer Journal* **1977**, *16*, 314.

- (20) Ohmi, N.; Nakajima, T.; Ohzawa, Y.; Koh, M.; Yamauchi, A.; Kagawa, M.; Aoyama, H. *Journal of Power Sources* **2013**, *221*, 6.
- (21) Nagasubramanian, G.; Orendorff, C. J. *Journal of Power Sources* **2011**, *196*, 8604.
- (22) Smart, M. C.; Ratnakumar, B. V.; Ryan-Mowrey, V. S.; Surampudi, S.; Prakash, G. K. S.; Hu, J.; Cheung, I. *Journal of Power Sources* **2003**, *119-121*, 359.
- (23) Moller, K.-C.; Hodal, T.; Appel, W. K.; Winter, M.; Besenhard, J. O. *Journal of Power Sources* **2001**, 595.
- (24) Galiński, M.; Lewandowski, A.; Stępnia, I. *Electrochimica Acta* **2006**, *51*, 5567.
- (25) Wasserscheid, P.; Keim, W. *Angew. Chem. Int. Ed.* **2000**, 3772.
- (26) Sun, J.; Forsyth, M.; MacFarlane, D. R. *J. Phys. Chem. B* **1998**, 8858.
- (27) Goodenough, J. B.; Kim, Y. *Chemistry of Materials* **2010**, *22*, 587.
- (28) Sun, J.; Stone, G. M.; Balsara, N. P.; Zuckermann, R. N. *Macromolecules* **2012**, *45*, 5151.
- (29) Croce, F.; Appetecchi, G. B.; Persi, L.; Scrosati, B. *Nature* **1998**, *394*, 456.
- (30) Niitani, T.; Amai, M.; Nakano, H.; Dokko, K.; Kanamura, K. *Journal of The Electrochemical Society* **2009**, *156*, A577.
- (31) Nishimoto, A.; Watanabe, M.; Ikeda, Y.; Kohjiya, S. *Electrochimica Acta* **1998**, *43*, 1177.
- (32) Hawker, C. J.; Chu, F.; Pomery, P. J.; Hill, D. J. T. *Macromolecules* **1996**, *29*, 3831.
- (33) Watanabe, M.; Hirakimoto, T.; Mutoh, S.; Nishimoto, A. *Solid State Ionics* **2002**, *148*, 399.
- (34) Gray, F. M. *Polymer Electrolytes* The Royal Society of Chemistry Cambridge, 1997.
- (35) Appetecchi, G. B.; Croce, F.; Marassi, R.; Persi, L.; Romagnoli, P.; Scrosati, B. *Electrochimica Acta* **1999**, *45*, 23.
- (36) Ye, H.; Huang, J.; Xu, J. J.; Khalfan, A.; Greenbaum, S. G. *Journal of The Electrochemical Society* **2007**, *154*, A1048.

- (37) Sirisopanaporn, C.; Fernicola, A.; Scrosati, B. *Journal of Power Sources* **2009**, *186*, 490.
- (38) Solvay Solexis: Italy 2002.
- (39) Kelly, J. Y., University of North Carolina at Chapel Hill, 2008.
- (40) Kostjuk, S. V.; Ortega, E.; Ganachaud, F.; Ameduri, B.; Boutevin, B. *Macromolecules* **2009**, *42*, 612.
- (41) Ebnesajjad, S. *Fluoroplastics, Volume 1: Non-Melt Processible Fluoropolymers - The Definitive User's Guide and Data Book*; Elsevier Waltham 2000.
- (42) Joel, A. K., Durham University, 1992.
- (43) Banks, R. E.; Smart, B. E.; Tatlow, J. C. *Organofluorine Chemistry: Principles and Commercial Applications*; Plenum Press New York 1994.
- (44) Lagow, R. J.; Margrave, J. L. *Prog. Inorg. Chem.* **1979**, *26*, 161.
- (45) Lagow, R. J.; Margrave, J. L. *J. Polym. Sci. Polym. Lett. Edn.* **1974**, *12*, 777.
- (46) Lagow, R. J.; Margrave, J. L. *J. Fluorine Chem.* **1970**, *4*, 371.
- (47) Ameduri, B.; Boutevin, B. *Well-Architected Fluoropolymers: Synthesis, Properties, and Applications*; Elsevier Amsterdam 2004.
- (48) Marchionni, G., Guarda, P.A. ; Solvay Solexis: 2005; Vol. European Patent 1 568730 A1.
- (49) Lorenzo, R. A. D., University of Toronto 2012.
- (50) Bunyard, W. C.; Romack, T. J.; DeSimone, J. M. *Macromolecules* **1999**, *32*, 8224.
- (51) Du, L.; Kelly, J. Y.; Roberts, G. W.; DeSimone, J. M. *J. of Supercritical Fluids* **2009**, *47*, 447.
- (52) Kaldonski, T.; Wojdyna, P. P. *Journal of KONES Powertrain and Transport* **2011**, *18*, 163.
- (53) Fowzy, M. A. *PFPE, A Unique Lubricant for a Unique Application* Castrol Industrial North America 1998.
- (54) Vitale, A.; Quaglio, M.; Marasso, S. L.; Chiodoni, A.; Cocuzza, M.; Bongiovanni, R. *Langmuir* **2013**, *29*, 15711.

- (55) Vitale, A.; Quaglio, M.; Cocuzza, M.; Pirri, C. F.; Bongiovanni, R. *European Polymer Journal* **2012**, 48, 1118.
- (56) Pantini, G. *Clinics in Dermatology*, 26, 387.
- (57) Gola, M.; Sansotera, M.; Navarrini, W.; Bianchi, C. L.; Gallo Stampino, P.; Latorrata, S.; Dotelli, G. *Journal of Power Sources* **2014**, 258, 351.
- (58) Rolland, J. P.; Van Dam, R. M.; Schorzman, D. A.; Quake, S. R.; DeSimone, J. M.; *Journal of the American Chemical Society* **2004**, 126, 2322.
- (59) Hampton, M. J., Williams, S.S., Zhou, Z., Nunes, J., Ko, D.-H., Templeton, J.L., Samulski, E.T., DeSimone, J.M. *Adv Mater* **2008**, 2667.
- (60) Schulte, V. A.; Hu, Y.; Diez, M.; Bünger, D.; Möller, M.; Lensen, M. C. *Biomaterials* **2010**, 31, 8583.
- (61) Stobie, N.; Duffy, B.; Hinder, S. J.; McHale, P.; McCormack, D. E. *Colloids and Surfaces B: Biointerfaces* **2009**, 72, 62.
- (62) Kim, J.; Rolland, J. P.; Carbonell, R. G.; DeSimone, J. M. *Chemistry of Materials* **2010**, 22, 2411.
- (63) Hu, Z.; Finlay, J. A.; Chen, L.; Betts, D. E.; Hillmyer, M. A.; Callow, M. E.; Callow, J. A.; DeSimone, J. M. *Macromolecules* **2009**, 42, 6999.
- (64) Hu, Z.; Chen, L.; Betts, D. E.; Pandya, A.; Hillmyer, M. A.; DeSimone, J. M. *Journal of the American Chemical Society* **2008**, 130, 14244.
- (65) Wang, Y.; Pitet, L. M.; Finlay, J. A.; Brewer, L. H.; Cone, G.; Betts, D. E.; Callow, M. E.; Callow, J. A.; Wendt, D. E.; Hillmyer, M. A.; DeSimone, J. M. *Biofouling* **2011**, 27, 1139.
- (66) Hu, Z. K.; Finlay, J. A.; Chen, L.; Betts, D. E.; Hillmyer, M. A.; Callow, M. E.; Callow, J. A.; DeSimone, J. M. *Macromolecules* **2009**, 42, 6999.
- (67) Sichina, W. J.; Perkin Elmer Instruments.
- (68) Gregorova, A.; InTech: 2013.
- (69) Colby College: <http://www.colby.edu/chemistry/PChem/lab/DiffScanningCal.pdf>, 2007.
- (70) <http://plastics.tamu.edu/content/thermal-analysis-polymers>: 2012.

- (71) Mikolajczak, C.; Kahn, M.; White, K.; Long, R. T. *Lithium-Ion Batteries Hazard and Use Assessment* The Fire Protection Research Foundation 2011.
- (72) Wong, D. H. C.; Thelen, J. L.; Fu, Y.; Devaux, D.; Pandya, A. A.; Battaglia, V. S.; Balsara, N. P.; Desimone, J. M. *Proc Natl Acad Sci U S A* **2014**, *111*, 3327.
- (73) Sorinmade, K. *Determination of Sustained Burning of Seven Polymer Solutions*, Kidde-Fenwal, Inc. , 2012.
- (74) Tsujikawa, T.; Yabuta, K.; Matsushita, T.; Matsushima, T.; Hayashi, K.; Arakawa, M. *Journal of Power Sources* **2009**, *189*, 429.
- (75) Mun, J.; Yim, T.; Park, J. H.; Ryu, J. H.; Lee, S. Y.; Kim, Y. G.; Oh, S. M. *Sci. Rep.* **2014**, *4*.
- (76) Lee, S. G.; Jeon, D. H. *Journal of Power Sources* **2014**, *265*, 363.
- (77) Xu, K. *Chem. Rev.* **2004**, *104*, 4303.
- (78) Monroe, C.; Newman, J. *Journal of The Electrochemical Society* **2003**, *150*, A1377.
- (79) Kalnaus, S.; Sabau, A. S.; Tenhaeff, W. E.; Dudney, N. J.; Daniel, C. *Journal of Power Sources* **2012**, *201*, 280.
- (80) Rubinstein, M.; Colby, R. H. *Polymer Physics*; Oxford University Press: New York, 2003.
- (81) Tarr, M.; University of Bolton: http://www.ami.ac.uk/courses/topics/0210_pt/.
- (82) Ulgut, B.; Gamry Instruments 2014.
- (83) Sai Scribner Associates, Inc. : <http://www.scribner.com/scribner-associates-support/knowledgebase>.
- (84) Lu, P.; Li, C.; Schneider, E. W.; Harris, S. J. *The Journal of Physical Chemistry C* **2013**, *118*, 896.
- (85) Metrohm Autolab B.V. http://www.ecochemie.nl/download/Applicationnotes/Autolab_Application_Note_BAT02.pdf.
- (86) Zugmann, S.; Fleischmann, M.; Amereller, M.; Gschwind, R. M.; Wiemhöfer, H. D.; Gores, H. J. *Electrochimica Acta* **2011**, *56*, 3926.
- (87) Doyle, M.; Fuller, T. F.; Newman, J. *Electrochimica Acta* **1994**, *39*, 2073.
- (88) Khalfan, A., City University of New York 2007.

- (89) Kerssebaum, R.; Bruker BioSpin GmbH: Rheinstetten, Germany, 2002.
- (90) Hoffman, R.; The Hebrew University
<http://chem.ch.huji.ac.il/nmr/techniques/other/diff/diff.html>, 2013.
- (91) Hayamizu, K.; Aihara, Y.; Arai, S.; Martinez, C. G. *Journal of Physical Chemistry B* **1998**, *103*, 519.
- (92) Williamson, M. J.; Hubbard, H. V. S. A.; Ward, I. M. *Polymer* **1999**, *40*, 7177.
- (93) Bruce, P. G.; Vincent, C. A. *Journal of Electroanalytical Chemistry and Interfacial Electrochemistry* **1987**, *225*, 1.
- (94) Mauro, V.; D'Aprano, A.; Croce, F.; Salomon, M. *Journal of Power Sources* **2005**, *141*, 167.
- (95) Evans, J.; Vincent, C. A.; Bruce, P. G. *Polymer* **1987**, *28*, 2324.
- (96) Hafezi, H.; Newman, J. *Journal of The Electrochemical Society* **2000**, *147*, 3036.
- (97) Ma, Y. P.; Doyle, M.; Fuller, T. F.; Doeff, M. M.; Dejonghe, L. C.; Newman, J. *Journal of The Electrochemical Society* **1995**, *142*.
- (98) Mussini, P. R.; Mussini, T. *Journal of Applied Electrochemistry* **1998**, *28*, 1305.

CHAPTER 2

PFPE/PEG BLENDS AS LI-ION BATTERY ELECTROLYTESⁱ

2.1 Introduction to Perfluoropolyether/Poly(ethylene glycol) Blends

Rechargeable batteries are integral to technological development in our society.^{1,2} State-of-the-art lithium-ion (Li-ion) batteries are not only incorporated in zero-emission vehicles and aircraft, but also have garnered interest for space and military applications.³ However, the thermal stability of Li-ion batteries- in particular, that of the electrolyte- is a critical issue to address. Traditional alkyl carbonates, the most common class of electrolytes for lithium-ion batteries, face a high risk of ignition under most operation conditions; this intrinsic instability is increased at high temperatures, and exothermic electrolyte breakdown can lead to thermal runaway.^{4,5} Additionally, the relatively high freezing point of carbonate-based solvents limits performance and precludes their use at low temperatures required for military and aerospace missions.^{3,6,7}

Amorphous, low glass transition temperature (T_g) polymeric electrolytes are promising candidates for the development of thermally robust Li-ion batteries. Eliminating the use of flammable solvents significantly enhances battery safety and improves high temperature performance. Poly(ethylene glycol) (PEG), also known as poly(ethylene oxide) (PEO), is the most commonly studied polymer in this regard. Although the ionic conductivity of PEG/salt

ⁱ This chapter previously appeared as an article in *Chemistry of Materials*. The original citation is as follows: Wong, D. H. C.; Vitale, A.; Devaux, D.; Taylor, A.; Pandya, A. A.; Hallinan, D. T.; Thelen, J. L.; Mecham, S. J.; Lux, S. F.; Lapidés, A. M.; Resnick, P. R.; Meyer, T. J.; Kostecki, R. M.; Balsara, N. P.; DeSimone, J. M. *Chemistry of Materials* **2015**, *in press*.

mixtures can be as high as 10^{-3} S/cm at temperatures above the PEG crystalline melting temperature (typically above 60 °C),⁸ the semi-crystalline nature of PEG renders it impractical for use at ambient or low temperatures.^{9,10} Extensive studies dedicated to mitigating PEG crystallinity through strategies that include the addition of copolymers^{11,12} and composite materials,^{13,14} as well as the development of star,¹¹ comb or brush,¹⁵⁻¹⁸ and dendritic¹⁹ polymeric architectures, have resulted in bulk conductive properties that are oftentimes drastically compromised. In addition, multi-step sophisticated synthetic schemes can increase the cost and complexity of electrolyte preparation.¹⁰

Alternatively, miscible polymer blends could provide a facile and cost-effective method for tuning electrolyte properties. Physical, thermal, and electrochemical properties of miscible polymer blends can be controlled by varying the ratios of pure components without synthesis of new materials.²⁰ We have previously reported the surprising miscibility between low molecular weight PEG and perfluoropolyethers (PFPEs) (Figure 2.1).^{21,22} Previous studies have also established that PFPEs belong to a unique class of chemically resistant, non-crystalline and nonflammable fluoropolymers that exhibit low T_g 's and low toxicity.^{21,23} Interestingly, PFPEs can also solvate bis(trifluoromethane)sulfonimide lithium salt (LiTFSI),²⁴ a commonly used salt in lithium batteries.²⁵

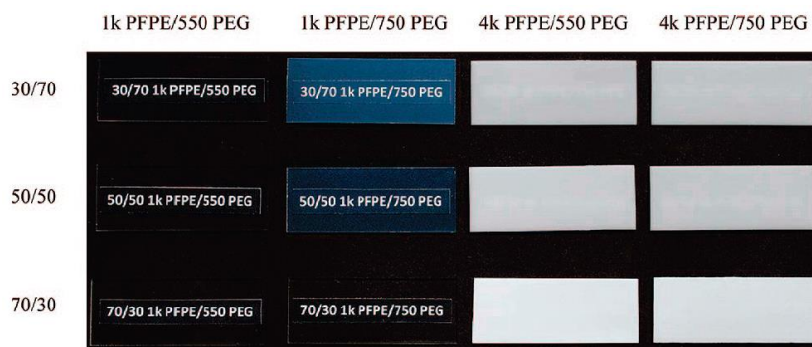


Figure 2.1 Photograph of PFPE/PEG blend films that are transparent or opaque based on composition ratios and molar masses, as reported by DeSimone and coworkers in *the Journal of*

the American Chemical Society. X-axis denotes the molar mass of PFPE and PEG and Y-axis represent composition ratios.²²

2.1.1 Investigations of Blends of Oligomers of PFPE and PEG with a Lithium Salt

Herein we report on the phase behavior and electrochemical properties of LiTFSI solvated in physical blends of PFPE₁₀₀₀-diol and PEG₄₀₀-diol electrolytes²⁶ (the subscripts and hyphen after PFPE and PEG indicate the molar masses of the polymers in g/mol and their end-groups respectively); chemical structures are shown in Figure 2.2. Here, PFPE is a random copolymer of perfluoroethylene and perfluoromethylene repeating units; the number of perfluoroethylene units, *m*, and the number of perfluoromethylene units, *n*, was determined through ¹⁹F NMR (discussed in more detail in Chapter 3) and was determined to be 7 and 3 respectively. To our knowledge, there is little precedent for investigating the potential use of miscible PFPE/PEG as lithium battery electrolytes. Our research presents the miscibility windows of ternary PFPE₁₀₀₀-diol/PEG₄₀₀-diol/LiTFSI mixtures, followed by the use of Fourier transform infrared spectroscopy (FTIR) and NMR spectroscopy to study the interactions between LiTFSI and the oligomers. Crystallization, identifying the presence of a semi-crystalline phase due to the PEG, is studied by differential scanning calorimetry (DSC). Ionic conductivity and transference number are determined by alternating (AC) impedance and direct current (DC) measurements.

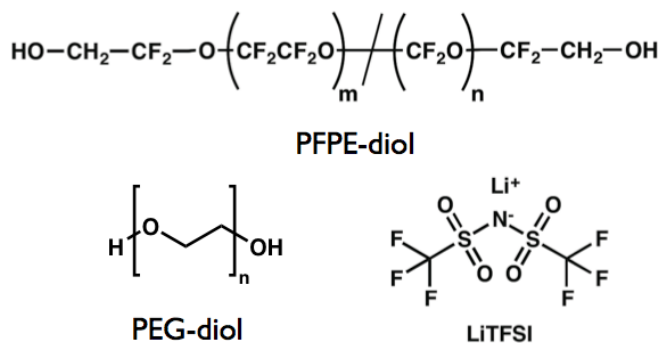


Figure 2.2 Chemical structures of PFPE-diol, PEG-diol, and LiTFSI.

2.2 Materials

PEG, average M_n 400, (PEG-400-diol) and LiTFSI were obtained from Sigma Aldrich. Perfluoropolyether Fluorolink D10 (PFPE-1000-diol) was obtained from Solvay-Solexis and Santa Cruz Biotechnology. All materials were dried at 90 °C under vacuum in a glovebox antechamber or vacuum oven for at least 24 h prior to use. LiTFSI, PFPE, and PEG were mixed together and stirred at room temperature for at least 12 h. Argon glove boxes (MBraun and Vacuum Atmospheres Company) with low oxygen and water concentration at sub-ppm levels were used for electrochemical sample preparation and characterization.

2.3 Experimental

2.3.1 Characterization of Physical and Thermal Properties

Ultraviolet visible absorption spectroscopy (UV-Vis) measurements were measured using a Varian Cary 50Bio UV-Visible Spectrometer over the wavelength range of 200 to 800 nm. FTIR spectroscopy was performed using a Bruker ALPHA FT-IR instrument from 4000 to 500 cm^{-1} at 4 cm^{-1} resolution under ambient conditions using an attenuated total reflectance (ATR) attachment. DSC thermograms were recorded using a TA Instruments DSC Q200 on samples which were prepared in air over the temperature range from -130 °C to 100 °C using a heat/cool/heat method at a heating and cooling rate of 10 °C and 5 °C/minute respectively. TGA were run using a Perkin Elmer Pyris 1 TGA apparatus under nitrogen and air from ambient to 600°C with a heating rate of 20°C/minute. Sustained burning data was determined per American Society of Testing and Materials (ASTM) D4206, conducted by Kidde Fenwal Combustion Research Center.

2.3.2 Electrochemical Characterization

AC impedance spectroscopy was obtained in a procedure previously developed by Balsara and coworkers.²⁵ In brief, the electrolytes were placed in conductivity cells; sample thicknesses were determined by subtracting the thickness of the lower and upper electrodes from the overall assembled cell thickness. The thicknesses ranged from 1 to 2.5 mm. A custom-made temperature controlled box was used to house the cells during the electrochemical experiments. The ac impedance spectroscopy measurements, performed using a 16-channel Bio-Logic VMP3 potentiostat, were made across the frequency range of 1 MHz to 1 Hz at a peak-to-peak amplitude voltage of 20 mV. The electrolyte resistance was determined by the low-frequency minimum on a Nyquist impedance plot. Measurements were made at a series of temperatures with a minimum of 3 h calibration at each temperature. All data presented in this work are from an initial heating run from 30°C to 120 °C, followed by a cooling period until room temperature and a final 10 h stabilization period at -0.5 °C. Standard 2325 coin cells comprising a Celgard 2500 separator impregnated with liquid electrolyte between two Li metal electrodes were assembled. A steady potential of 0.02 V was applied for 10 h after cell stabilization at -0.5°C, and the cell resistance that includes electrolyte and interface contributions was measured every hour by ac impedance spectroscopy using a DC signal of 0.02 V and an ac signal of 10 mV. The approximate transference number was calculated using methods previously proposed in the literature.²⁷

2.4 Results and Discussion

PFPE/PEG/LiTFSI mixtures (all of the subsequent experiments discussed were conducted using PFPE₁₀₀₀-diol and PEG₄₀₀-diol unless otherwise noted) were quantitatively evaluated by measuring the percent light transmittance and T_g using UV-Vis spectroscopy and

DSC respectively. Mixtures were considered miscible if they showed high transmittance of at least 90% in the range of 400 to 800 nm and a single T_g . In contrast, immiscible mixtures exhibited two distinct T_g 's (Figure 2.3) and were opaque (photograph in Figure 2.4), indicating coexistence of phase separated domains. The UV-Vis transmittance of phase separated mixtures was less than 25%. Immiscible solutions frequently separated into two distinct phases within a few hours. In contrast, miscible solutions were stable on the time scale examined (hours to weeks). Figure 2.4 also shows the miscibility windows of PFPE/PEG/LiTFSI solutions on a ternary phase diagram. The regions shaded in purple (darker regions) represent the miscible mixtures that were transparent. The region shaded in blue (lighter regions) represents the immiscible mixtures, which were opaque. Concentrations of the three components are specified in terms of weight (wt.) fractions.

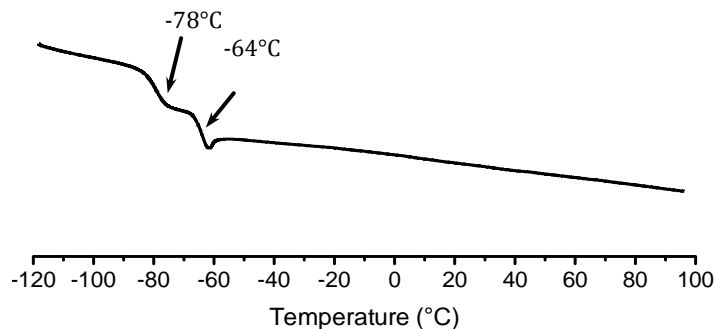


Figure 2.3 Representative DSC heating curve of an immiscible ternary blend (PFPE with 0.10 and 0.45 wt. fractions of LiTFSI and PEG respectively), exhibiting two distinct T_g 's at -78 °C and -64 °C.

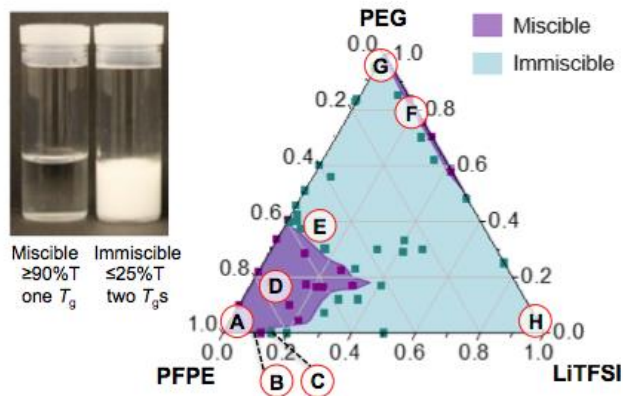


Figure 2.4 Photograph of miscible and immiscible ternary blends PFPE/PEG/LiTFSI and ternary phase diagram of PFPE, PEG, and LiTFSI physical blends expressed in wt. fractions.

The phase behavior of the PFPE/PEG-diol systems is consistent with previously reported binary mixtures of dimethacryloxy-terminated PFPE (1000 g/mol) (PFPE-DMA) and dimethacryloxy-terminated PEG (700 g/mol) (PEG-DMA) without LiTFSI, where multiple T_g s and low optical transparencies were also observed in immiscible blends. Immiscibility was also shown to occur in PFPE-DMA and 700 g/mol PEG-DMA blends that consisted of high weight fractions of PEG-DMA.²²

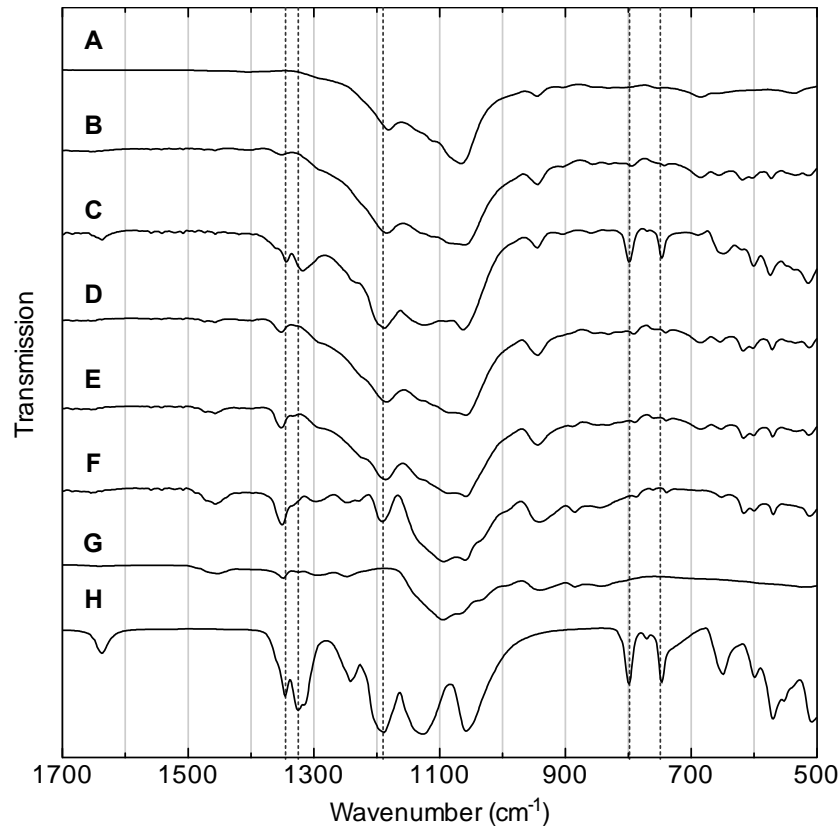
Binary mixtures of PFPE and PEG are miscible when the weight fraction of PFPE exceeds 0.6, consistent with previous studies.²² The large region of miscibility in Figure 2.4 comprising ternary mixtures rich in PFPE can be anticipated from the phase behavior of PFPE/PEG and PFPE/LiTFSI binary mixtures. Binary PEG/LiTFSI mixtures are also miscible when the PEG weight fraction exceeds 0.5. Interestingly, adding exceedingly small quantities of PFPE to these mixtures renders them immiscible indicating that the polymer/polymer interactions govern the overall phase behavior of the ternary mixture.

Fourier transform infrared spectroscopy was conducted in order to gain a better understanding of the solubility and phase behavior of these blends. Figure 2.5 shows the FTIR

spectra in the range of 1700 and 500 cm^{-1} wavenumbers of several binary and ternary systems compared to the spectra of pure LiTFSI, PFPE, and PEG. The compositions of the systems of interest are identified by the letters A through H in Figure 2.4

Pure solid LiTFSI (H; 0 wt. fraction of PFPE and PEG) exhibits characteristic bands at 1190 cm^{-1} , from SO_2 asymmetric stretching, at 1325 and 1345 cm^{-1} , from CF_3 asymmetric stretching, and at 748 and 798 cm^{-1} which originate from symmetric S-N-S stretching. The presence of these peaks in mixtures is commonly taken as indication of the presence of LiTFSI aggregates.^{10,28-32} All of the miscible solutions (B (PFPE with 0.10 wt. fraction of LiTFSI), D (PFPE with 0.18 wt. fraction of PEG and 0.10 wt. fraction of LiTFSI) and F (PEG with 0.20 wt. fraction of LiTFSI)) show a substantial reduction in peak intensity at 748, 798, 1190, 1325 and 1345 cm^{-1} indicating the absence of LiTFSI aggregates. These observations are thus consistent with the presence of dissociated TFSI⁻ ions.^{24,33}

Interestingly, signatures of dissociated TFSI were also observed in the FTIR spectra of some immiscible ternary mixtures (e.g. E (PFPE with 0.35 wt. fraction of PEG and 0.12 wt. fraction of LiTFSI)). This suggests that immiscibility in this mixture is mainly driven by the limited miscibility of the two polymers rather than the limit of solubility of LiTFSI in the polymers. While blend E contains PEG-rich and PFPE-rich phases with LiTFSI dissolved in both phases, the immiscible binary PFPE/LiTFSI mixture (C (PFPE with 0.20 wt. fraction of LiTFSI)) shows bands at 748 and 798 cm^{-1} indicating the presence of LiTFSI aggregates in this system. Increased absorption at 1190, 1325 and 1345 cm^{-1} is also observed in mixture C.



- A- Pure PFPE
- B- PFPE with 0.10 wt. fraction of LiTFSI (miscible)
- C- PFPE with 0.20 wt. fraction of LiTFSI (immiscible)
- D- PFPE with 0.18 wt. fraction of PEG and 0.10 wt. fraction of LiTFSI (miscible)
- E- PFPE with 0.35 wt. fraction of PEG and 0.12 wt. fraction of LiTFSI (immiscible)
- F- PEG with 0.20 wt. fraction of LiTFSI (miscible)
- G- Pure PEG
- H- Solid LiTFSI

Figure 2.5 FTIR spectra of PFPE, PEG, LiTFSI and blended solutions at various molar ratios. Highlighted guidelines are shown at 748, 798, 1190, 1325 and 1345 cm⁻¹ respectively.

The crystallization behavior of binary PFPE/PEG blends is shown in Figure 2.6 and Figure 2.7. Increasing amounts of PFPE reduces the enthalpy of crystallization (Figure 2.6). Complex crystallization behavior is observed in immiscible PFPE/PEG blends where PFPE weight fractions are below 0.6. No crystallization is observed in miscible PFPE/PEG blends with PFPE weight fraction greater than 0.8. The degree of crystallinity, X_c , is given by:

$$X_c = \left(\frac{\Delta H}{\Delta H_0} \right) \times 100 \dots \dots \dots \text{equation 2.1}$$

where ΔH is the crystallization enthalpy of the blend and ΔH_0 is that of a 100% crystalline PEO, reported as 166 J/g.³⁴ As shown in Figure 2.7, crystallinity decreases as the weight fraction of PFPE increases and falls to zero when the PFPE weight fraction exceeds 0.7.

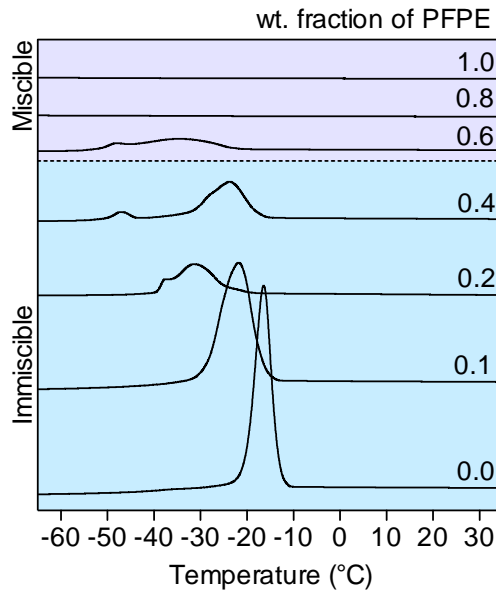


Figure 2.6 DSC cooling traces of PFPE and PEG blends at various PFPE wt. fractions

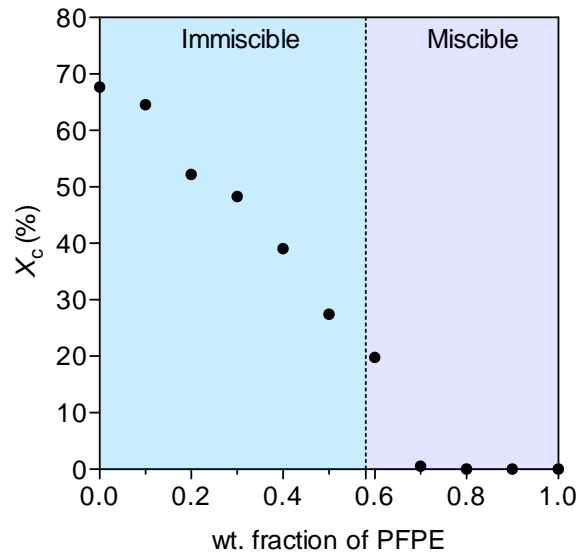


Figure 2.7 Percent crystallinity, expressed in X_c , as a function of PFPE wt. fraction.

It is generally assumed that amorphous polymer/salt mixtures are ideally suited for battery electrolyte applications. We thus chose to study ternary mixtures wherein the weight fraction of PFPE in the liquid components is 0.8. In other words, the weight ratio of PFPE to PEG remains consistently at 80 to 20 even as LiTFSI is added; this blend is henceforth referred to as PFPE+PEG. This blend is non-crystalline (no detection of melting temperature or crystallization temperature (T_m or T_c)), exhibits a single low T_g of -86 °C, and shows good thermal stability (degradation temperature at 5 % weight loss (T_d (5%)) is 198 °C in nitrogen, 207 °C in air) (Figure 2.8). Moreover, PFPE+PEG is nonflammable even with dissolved LiTFSI (Table 2.1). In the discussion below, we compare the properties of this PFPE+PEG blend with added LiTFSI to that of PFPE/LiTFSI and PEG/LiTFSI blends. For all three systems, the salt concentration is quantified by r , defined as the ratio of Li^+ ions to oxygen atoms. This is because of the well-established fact that the solvation shells surrounding dissociated ions are rich in oxygen.

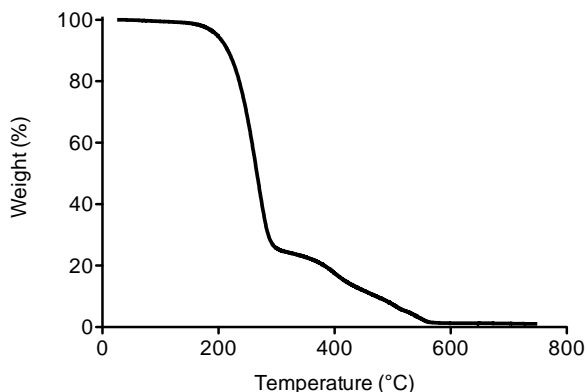


Figure 2.8 Thermogram of PFPE/PEG Blend ($[\text{PFPE}]/[\text{PEG}]=1.6$) with LiTFSI concentration $r = 0.026$. (T_d (5%) = 197.84 °C) in N_2 .

Table 2.1 Sustained burning information for PFPE+PEG Electrolyte ($r = 0.026$)

Test Temperature (°C)	Sustained Burning Time	Sustained Burning Observed
235	Not detected	No

In order to study the effect of LiTFSI on the thermal properties of the PFPE+PEG blends, DSC experiments were performed on binary and ternary blends containing LiTFSI. Figure 2.9 shows the linear increase of T_g with increasing salt concentration r in all three systems (r , defined as the molar ratio of lithium ion and repeating units on a polymer backbone, is a common notation used to describe lithium salt concentration in polymers electrolytes). This is expected, as molecular dynamics simulations and neutron diffraction data indicate that oxygen atoms in the PEG backbone coordinate with lithium ions to form temporary crosslinks,^{16,35-37} limiting polymer chain mobility and resulting in a higher T_g . Interestingly, the slope of T_g versus r is larger for PEG than PFPE and PFPE+PEG blend, indicating that the T_g of PEG is more sensitive to LiTFSI concentration. The effect of r on T_g is less pronounced in PFPE-containing electrolytes, as the ether oxygens are less nucleophilic due to the strongly electron withdrawing fluorines in the PFPE backbone, which, in turn, weakens interactions between Li^+ and O. The PFPE+PEG blend demonstrates T_g vs. r behavior similar to PFPE. More importantly, it is clear that blending PFPE with PEG reduces T_g relative to pure PEG; In the absence of LiTFSI, the measured T_g of pure PFPE+PEG blend is within 3 °C of the calculated T_g as predicted by the Fox equation³⁸ for miscible binary systems:

$$\frac{1}{T_g} = \frac{x_1}{T_{g,1}} + \frac{x_2}{T_{g,2}} \dots \dots \dots \text{equation 2.2}$$

where $T_{g,1}$ and $T_{g,2}$ pertain to the pure components, and x_1 and x_2 are the weight fractions of each component in the blend. Agreement with the Fox equation further confirms the miscibility of the two polymers. At constant $r = 0.026$, the T_g of the blended electrolyte is also almost 20 °C lower than PEG, successfully extending the temperature range in which the electrolyte remains amorphous.

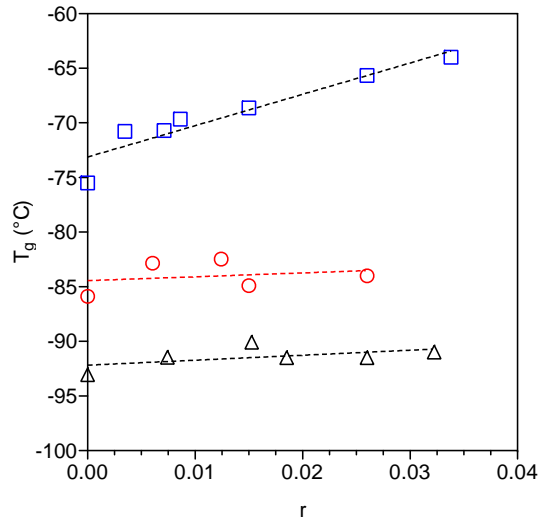


Figure 2.9 T_g of PFPE (Δ), PEG (\square), and PFPE+PEG blend (\circ) electrolytes as a function of salt concentration r ; dotted lines represent fitted linear regressions.

Interactions between LiTFSI and polymer chains were also investigated via ^{19}F NMR. Figure 2.10 depicts the ^{19}F NMR spectra of PFPE, PEG, and PFPE+PEG blend electrolytes all with $r = 0.026$ compared to a 0.05 M solution of LiTFSI in deuterium oxide (D_2O) and pure PFPE. Each sample contains a coaxial insert spiked with a 5 wt. % solution of trifluoroacetic acid in D_2O whose signal was calibrated to -76.5 ppm for referencing.

Since this PFPE is a random linear copolymer: $\text{X-O}[(\text{CF}_2\text{CF}_2\text{O})_m(\text{CF}_2\text{O})_n]\text{-X}$ where $m/n \approx 7/3$ and $\text{X} = -\text{CF}_2\text{CH}_2\text{OH}$, chemical shifts in the ^{19}F NMR spectra of the PFPEs are sensitive to the distinct location of the fluorinated atoms along the chain and can be categorized into three distinct regions (i) interior CF_2 groups give rise to peaks between -55 and -60 ppm, (ii) terminal CF_2 groups give rise to peaks between -82 and -87 ppm, and (iii) interior $\text{CF}_2\text{-CF}_2$ groups give rise to peaks between -90 and -95 ppm (Figure 2.10). The multiple peaks in each region arise from the different combinations of neighboring repeating units.^{39,40} For example, the most downfield peak in region (i) (-55 to -60 ppm) is assigned to the fluorines in a CF_2O unit neighboring two $\text{CF}_2\text{CF}_2\text{O}$ units on each side. Likewise, the middle peak corresponds to the

fluorines in a CF₂O unit in between a CF₂O and CF₂CF₂O group, and the most upfield peak in that region corresponds to fluorines in a CF₂O unit in between two CF₂O groups.

The chemical shifts and full width at half maximum (FWHM) of NMR peaks in the LiTFSI region and region (ii) of PFPE are listed in Table 1. The FWHM values of peaks associated with LiTFSI in both PEG and D₂O are 3 Hz. This suggests the presence of mobile TFSI⁻ ions in these systems. In contrast, the FWHM of the same peak in PFPE and PFPE+PEG blend is 11 and 6 Hz, respectively. There are two possible reasons for this observation: (1) a substantial decrease in the mobility of TFSI⁻ ions, (2) an increase in the number of microenvironments surrounding the fluorinate fluorine atoms. A decrease in the mobility of the anion dissolved in the PEG, PFPE/PEG, and PFPE respectively should effectively increase the Li⁺ transference number, t^+ , of the electrolyte, defined as the fraction of the overall current carried by the Li ions; this is consistent with our results discussed later.

The FWHM of the fluorine peaks in region (ii) of PFPE is 38 Hz for pure PFPE, 39 Hz for PFPE/LiTFSI and 72 Hz for PFPE+PEG/LiTFSI. There are two possible explanations for these observations: (1) the addition of high T_g PEG slows down segmental motion of PFPE, (2) an increase in the number of microenvironments surrounding the fluorinate atoms. Note that the addition of PEG to PFPE/LiTFSI decreases FWHM in the LiTFSI fluorine region but increases the FWHM in the PFPE fluorine end group region (ii). The addition of PEG to PFPE/LiTFSI results in an upfield shift of the peak position in both LiTFSI and PFPE regions (see first three entries in Table 2.2). This is primarily due to changes in solvent polarity. The TFSI⁻ ions are more deshielded in the presence of PEG, as it is more polar than PFPE. Further upfield shifts in the TFSI region are seen in PEG and D₂O samples due to this polarity effect.

In the PFPE/PEG blend, the TFSI⁻ fluorine signal arises as a single peak, with a chemical shift in between that of TFSI⁻ in PFPE and PEG. This indicates, on the timescale faster than experimental NMR acquisition, the average electronic environment experienced by TFSI⁻ is homogenous. This also crucially implies that miscible solutions of PFPE/PEG blends do not simply offer a combination of ionic environments from pure PFPE and PEG (which would have likely resulted in TFSI⁻ peak splitting or two separate peaks), but produces a uniform environment intermediate of both materials.

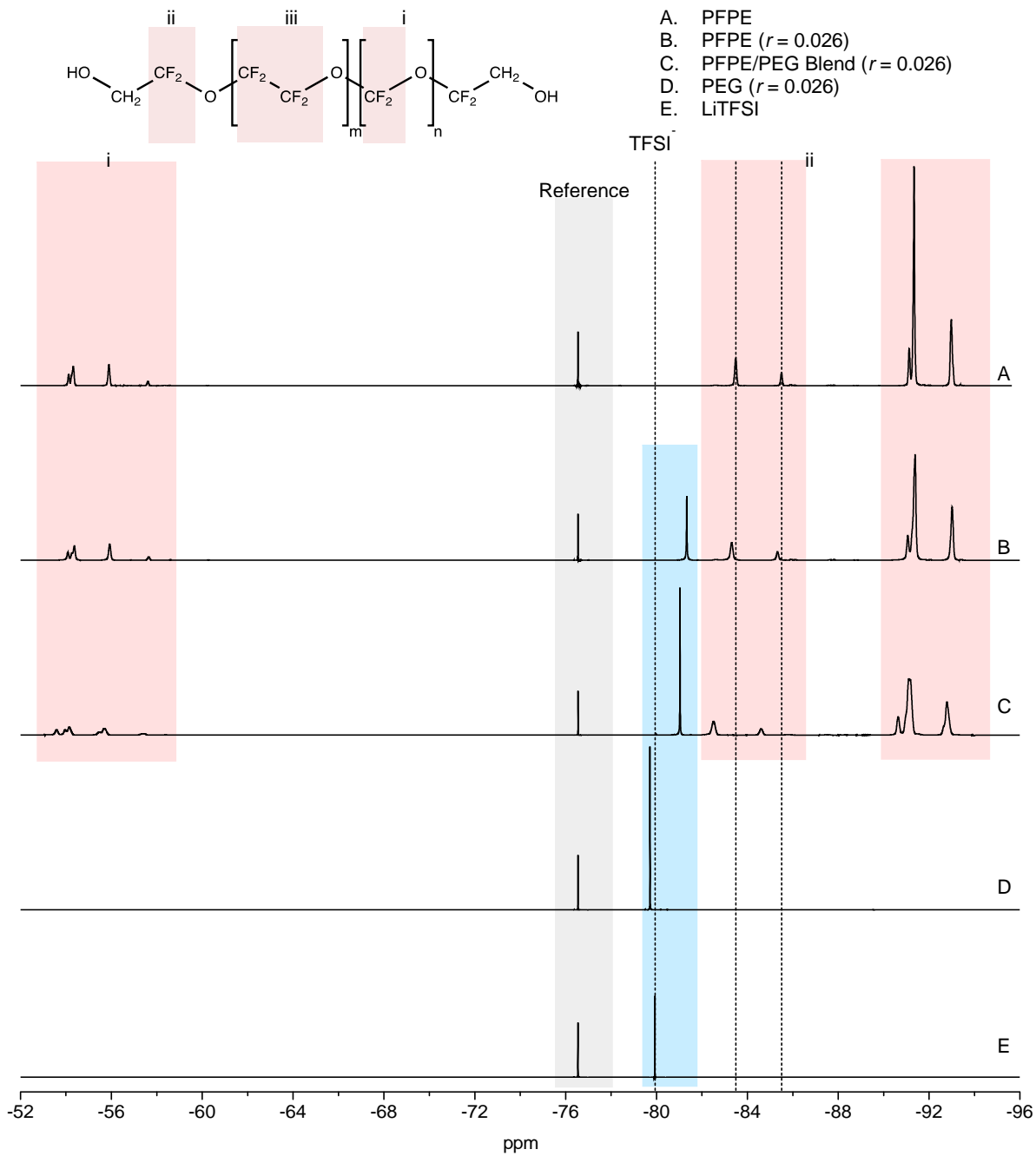


Figure 2.10 ^{19}F NMR spectra of PFPE, PEG, and PFPE+PEG electrolytes in reference to 0.05M LiTFSI in D_2O and pure PFPE. Highlighted guidelines are shown at -79.94, -83.49, and -85.51 ppm.

Table 2.2 Selected peaks and full widths at half maximum of ^{19}F NMR for PEG, PFPE+PEG and PFPE electrolytes (n.a. = not available)

Sample	LiTFSI		PFPE (Region ii)	
	Chemical shift (ppm)	FWHM (Hz)	Chemical shift (ppm)	FWHM (Hz)
PFPE	n.a.	n.a.	-83.5, -85.5	46, 38
PFPE ($r = 0.026$)	-81.4	11	-83.3, -85.3	59, 49
PFPE+PEG Blend ($r = 0.026$)	-81.0	6	-82.5, -84.6	82, 72
PEG ($r = 0.026$)	-79.7	3	n.a.	n.a.
LiTFSI in D_2O	-79.9	3	n.a.	n.a.

The ionic conductivity of PFPE, PEG, and PFPE+PEG blend electrolytes was measured at a salt concentration of $r = 0.026$ at temperatures between $0\text{ }^\circ\text{C}$ and $120\text{ }^\circ\text{C}$, as shown in Figure 2.11. Pure PEG exhibits conductivity of between 3×10^{-5} to 4×10^{-3} S/cm in this temperature range, similar to values previously reported for low molar mass PEGs.^{12,25} On the other hand, the PFPE+PEG blend exhibits conductivity between 1×10^{-5} to 2×10^{-3} S/cm, lower than pure PEG but drastically higher than pure PFPE. The conductivities of these electrolytes are lower than conventional carbonate electrolytes ($\sim 7 \times 10^{-3}$ S/cm at room temperature),⁴¹ but are comparable to other nonflammable electrolyte systems with low T_g .⁴² In each case, the ionic conductivity also increases with increasing temperature, typical of polymer electrolytes. The temperature dependence of the ionic conductivity of these materials was found to be well-described by the Vogel-Tamman-Fulcher (VTF) equation:⁴³⁻⁴⁵

$$\sigma(T) = \frac{A}{\sqrt{T}} \exp\left(\frac{-B}{R(T-T_0)}\right) \dots \dots \dots \text{equation 2.3}$$

where σ is the ionic conductivity, A is a constant proportional to the number of charge carriers, B is equivalent to the activation energy for ion motion, R is the gas constant, T is the experimental temperature, and T_0 is an empirical reference temperature taken as the idealized temperature corresponding to zero configurational entropy, typically chosen to be 50 K below the T_g of each

sample.¹⁰ Fits to this equation are shown in Figure 2.11 as solid lines for each data set, and the corresponding parameters are shown in Table 2.3.

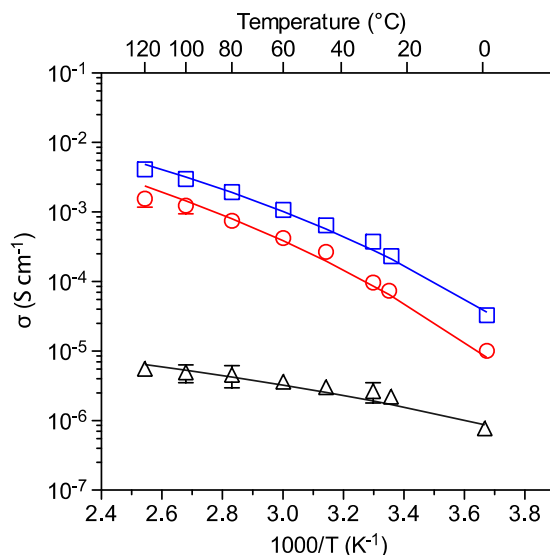


Figure 2.11 Temperature-dependent ionic conductivities of PFPE (black Δ), PEG (blue \square), and PFPE/PEG blend (red \circ) electrolytes ($r = 0.026$); each sample follow VTF behavior.

Table 2.3 VTF fitted parameters for PEG, PFPE+PEG and PFPE electrolytes containing LiTFSI ($r = 0.026$).

Electrolyte	A ($\text{S cm}^{-1} \text{K}^{+0.5}$)	B (KJ mol^{-1})	T_0 (K)
PEG	12.3	9.5	157
PFPE+PEG Blend	12.3	10.9	157
PFPE	1.6×10^{-3}	5.5	132

By fitting measured conductivity using the VTF equation, it is clear that despite lower T_0 and activation energy parameters, the ionic conductivity of pure PFPE is low due to a significantly lower amount of charge carriers. Addition of PEG clearly enhances the number of charge carriers and conductivity for the overall electrolytes while retaining PFPE-like thermal properties (see Figure 2.9).

We have previously reported that pure PFPE-based electrolytes exhibit Li-ion transference numbers, t^+ , close to unity.²⁴ We use the same method described in reference 27 to

estimate t^+ of PFPE, PEG, PFPE+PEG electrolytes, with $r = 0.026$, at $-2\text{ }^\circ\text{C}$. We obtained t^+ values of 0.84 (PFPE), 0.17 (PEG), and 0.29 (PFPE+PEG). It is important to know that our method becomes increasingly inaccurate as the transference number decreases. The addition of PEG dramatically reduces the transference number of the PFPE blend electrolytes.

2.5 Conclusion

Physical blends of oligomeric PFPE and PEG were prepared. Their miscibility, ability to solvate LiTFSI, thermal properties, and electrochemical properties were explored. An optimal ratio of PFPE to PEG was selected for electrochemical characterizations. Conductivity of this electrolyte at LiTFSI concentration $r = 0.026$ was measured to be $2 \times 10^{-4}\text{ S/cm}$ at $30\text{ }^\circ\text{C}$, slightly lower than that of pure PEG at the same salt concentration but approximately two orders of magnitude higher than pure PFPE electrolytes. In addition, blending PEG with PFPE reduces the T_g and prevents crystallization. The uniqueness of PFPE+PEG electrolytes arises from the fact that they enable control over physical, thermal, and electrochemical properties of a polymer electrolyte by simple blending rather than schemes involving new chemical synthesis.

REFERENCES

- (1) Tarascon, J. M.; Armand, M. *Nature* **2001**, *414*, 359.
- (2) Goodenough, J. B.; Park, K. S. *Journal of the American Chemical Society* **2013**, *135*, 1167.
- (3) Plichta, E. J.; Hendrickson, M.; Thompson, R.; Au, G.; Behl, W. K.; Smart, M. C.; Ratnakumar, B. V.; Surampudi, S. *Journal of Power Sources* **2001**, *94*, 160.
- (4) Hammami, A.; Raymond, N.; Armand, M. *Nature* **2003**, *424*, 635.
- (5) Mandal, B. K.; Padhi, A. K.; Shi, Z.; Chakraborty, S.; Filler, R. *Journal of Power Sources* **2006**, *161*, 1341.
- (6) Smart, M. C.; Ratnakumar, B. V.; Surampudi, S. *Journal of The Electrochemical Society* **1999**, *146*, 486.
- (7) Xiao, L. F.; Cao, Y. L.; Ai, X. P.; Yang, H. X. *Electrochimica Acta* **2004**, *49*, 4857.
- (8) Hallinan, D. T.; Balsara, N. P. *Annual Review of Materials Research* **2013**, *43*, 503.
- (9) Berthier, C.; Gorecki, W.; Minier, M.; Armand, M. B.; Chabagno, J. M.; Rigaud, P. *Solid State Ionics* **1983**, *11*, 91.
- (10) Barteau, K. P.; Wolffs, M.; Lynd, N. A.; Fredrickson, G. H.; Kramer, E. J.; Hawker, C. J. *Macromolecules* **2013**, *46*, 8988.
- (11) Niitani, T.; Amaike, M.; Nakano, H.; Dokko, K.; Kanamura, K. *Journal of The Electrochemical Society* **2009**, *156*, A577.
- (12) Panday, A.; Mullin, S.; Gomez, E. D.; Wanakule, N.; Chen, V. L.; Hexemer, A.; Pople, J.; Balsara, N. P. *Macromolecules* **2009**, *42*, 4632.
- (13) Choi, J.-W.; Cheruvally, G.; Kim, Y.-H.; Kim, J.-K.; Manuel, J.; Raghavan, P.; Ahn, J.-H.; Kim, K.-W.; Ahn, H.-J.; Choi, D. S.; Song, C. E. *Solid State Ionics* **2007**, *178*, 1235.
- (14) Quartarone, E.; Mustarelli, P. *Chemical Society Reviews* **2011**, *40*, 2525.
- (15) Zhang, Y.; Costantini, N.; Mierzwa, M.; Pakula, T.; Neugebauer, D.; Matyjaszewski, K. *Polymer* **2004**, *45*, 6333.
- (16) Sun, J.; Stone, G. M.; Balsara, N. P.; Zuckermann, R. N. *Macromolecules* **2012**, *45*, 5151.

- (17) Watanabe, M.; Endo, T.; Nishimoto, A.; Miura, K.; Yanagida, M. *Journal of Power Sources* **1999**, *81*, 786.
- (18) Zheng, T.; Zhou, Q.; Li, Q.; Zhang, L.; Li, H.; Lin, Y. *Solid State Ionics* **2014**, *259*, 9.
- (19) Gong, A.; Liu, C.; Chen, Y.; Chen, C.; Xi, F. *Polymer* **2000**, *41*, 6103.
- (20) Ghelichi, M.; Qazvini, N. T.; Jafari, S. H.; Khonakdar, H. A.; Farajollahi, Y.; Scheffler, C. *Journal of Applied Polymer Science* **2013**, *129*, 1868.
- (21) Hu, Z.; Chen, L.; Betts, D. E.; Pandya, A.; Hillmyer, M. A.; DeSimone, J. M. *Journal of the American Chemical Society* **2008**, *130*, 14244.
- (22) Hu, Z.; Chen, L.; Betts, D. E.; Pandya, A.; Hillmyer, M. A.; DeSimone, J. M. *Journal of the American Chemical Society* **2008**, *130*, 14244.
- (23) Rolland, J. P.; Van Dam, R. M.; Schorzman, D. A.; Quake, S. R.; DeSimone, J. M. *Journal of the American Chemical Society* **2004**, *126*, 2322.
- (24) Wong, D. H. C.; Thelen, J. L.; Fu, Y.; Devaux, D.; Pandya, A. A.; Battaglia, V. S.; Balsara, N. P.; Desimone, J. M. *Proc Natl Acad Sci U S A* **2014**, *111*, 3327.
- (25) Teran, A. A.; Tang, M. H.; Mullin, S. A.; Balsara, N. P. *Solid State Ionics* **2011**, *203*, 18.
- (26) Wong, D. H. C.; Vitale, A.; Devaux, D.; Taylor, A.; Pandya, A. A.; Hallinan, D. T.; Thelen, J. L.; Mecham, S. J.; Lux, S. F.; Lapidus, A. M.; Resnick, P. R.; Meyer, T. J.; Kostecki, R. M.; Balsara, N. P.; DeSimone, J. M. *Chemistry of Materials* **2015**, *in press*.
- (27) Bruce, P. G.; Vincent, C. A. *Journal of Electroanalytical Chemistry and Interfacial Electrochemistry* **1987**, *225*, 1.
- (28) Rey, I.; Lassegues, J. C.; Grondin, J.; Servant, L. *Electrochimica Acta* **1998**, *43*, 1505.
- (29) Huang, W.; Wheeler, R. A.; Frech, R. *Spectrochimica Acta Part A: Molecular Spectroscopy* **1994**, *50*, 985.
- (30) Wen, S. J.; Richardson, T. J.; Ghantous, D. I.; Striebel, K. A.; Ross, P. N.; Cairns, E. J. *Journal of Electroanalytical Chemistry* **1996**, *408*, 113.
- (31) Hu, Y.; Wang, Z.; Li, H.; Huang, X.; Chen, L. *Spectrochimica Acta Part A: Molecular and Biomolecular Spectroscopy* **2005**, *61*, 2009.
- (32) Li, J.; Huang, X.; Chen, L. *Journal of The Electrochemical Society* **2000**, *147*, 2653.

- (33) Wen, S. J.; Richardson, T. J.; Ghantous, D. I.; Striebel, K. A.; Ross, P. N.; Cairns, E. J. *Journal of Electroanalytical Chemistry* **1996**, *408*, 113.
- (34) Minelli, M.; Giacinti Baschetti, M.; Hallinan, D. T.; Balsara, N. P. *Journal of Membrane Science* **2013**, *432*, 83.
- (35) Allcock, H. R.; Kellam Iii, E. C. *Solid State Ionics* **2003**, *156*, 401.
- (36) Borodin, O.; Smith, G. D. *Macromolecules* **1998**, *31*, 8396.
- (37) Saboungi, M.-L.; Price, D. L.; Mao, G.; Fernandez-Perea, R.; Borodin, O.; Smith, G. D.; Armand, M.; Howells, W. S. *Solid State Ionics* **2002**, *147*, 225.
- (38) Fox, T. G. *Bulletin of the American Physical Society* **1956** *1*, 123.
- (39) Tchistiakov, A.; Fontana, S.; Tonelli, C.; Solvay Solexis S.p.A: US 2006; Vol. US 2006/0009660 A1.
- (40) Di Lorenzo, R. A., University of Toronto, 2012.
- (41) Goodenough, J. B.; Kim, Y. *Chemistry of Materials* **2010**, *22*, 587.
- (42) Zhang, L.; Luo, H.; Zhao, X.; United States 2013; Vol. US 2013/0084490 A1.
- (43) Vogel, H. *Physikalische Zeitschrift* **1921**, *22*, 645.
- (44) Fulcher, G. S. *Journal of the American Ceramic Society* **1925**, *8*, 339.
- (45) Tammann, G.; Hesse, W. *Zeitschrift für anorganische und allgemeine Chemie* **1926**, *156*, 245.

CHAPTER 3
NOVEL PERFLUOROPOLYETHER-BASED ELECTROLYTESⁱⁱ

3.1 Investigations of Perfluoropolyether/carbonate Electrolytes

Large scale rechargeable batteries are expected to play a key role in today's emerging sustainable energy landscape.^{1,2} State-of-the-art lithium (Li) batteries are not only used to power zero emission electric vehicles, but they are currently gaining traction as backup power in aircrafts and smart grid applications.^{3,4} The electrolyte used in these batteries, however, hinders their use in large scale applications: it contains a flammable mixture of alkyl carbonate solvents that frequently lead to safety issues. Dimethyl carbonate (DMC), an important component in commercial lithium-ion (Li-ion) battery electrolytes, has a Hazardous Materials Identification Systems (HMIS) flammability rating of 3 on a scale of 0 - 4, indicating a high risk of ignition under most operating conditions. The intrinsic instability of carbonate-based solvents increases at higher temperatures, where exothermic electrolyte breakdown often leads to thermal runaway,^{5,6} resulting in catastrophic failure of the battery. While this failure rate stands at about one in ten million systems, it is intolerable for large-scale applications where cost and user safety could be heavily compromised. This necessitates the development of radically new electrolytes with improved safety.

Desirable electrolyte properties include a large window of phase stability (no vaporization or crystallization), complete nonflammability, a wide electrochemical stability window, and

ⁱⁱ This chapter previously appeared as an article in *Proc Natl Acad Sci U S A*. The original citation is as follows: Wong, D. H. C.; Thelen, J. L.; Fu, Y.; Devaux, D.; Pandya, A. A.; Battaglia, V. S.; Balsara, N. P.; DeSimone, J. M. *Proc Natl Acad Sci U S A* **2014**, *111*, 3327.

suitable ionic transport for the targeted application. There are many approaches to synthesizing materials with these properties, e.g. ionic liquids,^{7,8} gel-polymer matrices,^{9,10} and small molecule additives.¹¹⁻¹³ Systems utilizing poly(ethylene oxide) (PEO) are also well-studied.^{14,15} PEO can solvate high concentrations of lithium salts, and is considered nonflammable. Unfortunately, practical conductivity is often limited to a higher than desired temperature range¹⁴ and it is well known that in these systems, the motion of the Li ion carries only a small fraction of the overall current (also known as the Li-ion transference number, t^+). PEO-based electrolytes typically exhibit t^+ values between 0.1 and 0.5,¹⁶⁻²⁰ leading to strong salt concentration gradients across the electrolytes that limit power density. Recently we reported the surprising miscibility of PEO with a class of perfluorinated ethers known as perfluoropolyethers (PFPEs).²¹ Building upon this work, we found that not only were various lithium salts soluble in blends of PEO and PFPEs, but also directly in pure PFPEs.

Herein we report the functionalization synthesis and characterization of a new class of nonflammable liquid electrolytes for lithium batteries based on neat functionalized perfluoropolyethers. PFPEs are a unique class of fluoropolymers with low glass transition temperature (T_g) ($T_g < -80$ °C) and low viscosity over a wide and useful temperature range encompassing ambient conditions, exhibit low toxicity, and are extremely chemically resistant.²² Our approach is to use PFPEs as an intrinsically fireproof platform that can be chemically tailored to achieve the desired conductive properties for Li-ion batteries. We have found that functionalized PFPEs can solvate the well-known lithium salt bis(trifluoromethane)sulfonimide lithium salt (LiTFSI) and conduct Li-ions with a high t^+ close to unity. We demonstrate successful cycling of Li/Li nickel manganese cobalt oxide ($\text{Ni}_{1/3}\text{Co}_{1/3}\text{Mn}_{1/3}\text{O}_2$, NMC) cells with a

PFPE/LiTFSI electrolyte, confirming the viability of using this new material towards the development of inherently safe batteries.

3.2 Materials

Fluorolink D10 (kinematic viscosity 70 cSt), Fluorolink D10/H, Fomblin ZDOL, and Fomblin ZDOL 4000 were obtained from Solvay Solexis. LiTFSI was obtained from Acros Organics. LiNMC powder was obtained from Umicore (Cellcore® MX-6). Battery-grade acetylene black (AB) with an average particle size of 40 nm and a material density of 1.95 g/cm³ was acquired from Denka Singapore Private Limited. The binder polyvinylidene fluoride (PVDF 1100) was supplied by Kureha, Japan. Anhydrous N-methylpyrrolidone (NMP) was purchased from Aldrich Chemical Company.

3.3 Experimental

3.3.1 Synthesis of PFPE-Dimethyl Carbonate

Fluorolink D10 (1000 g/mol, 0.02 moles) and triethylamine (TEA) (0.7255 g/mL, 0.05 moles) were dissolved in 1,1,1,3,3-pentafluorobutane (500 mL) at 0 °C in an ice bath under stirring conditions using a magnetic stirrer in a nitrogen atmosphere. A solution of methyl chloroformate (1.223 g/mL, 0.05 moles) was then added drop wise (over approximately 1 minute), after which the mixture was allowed to return to ambient conditions and stirred for 12 h sealed under nitrogen gas. The resulting mixture was gravity filtered and the filtrate was washed with equal amounts of water three times and brine two times to remove residual triethylammonium hydrochloride salt. The remaining organic layer was dried over magnesium sulfate, filtered, and the solvent in the filtrate was evaporated under reduced pressure, providing the product PFPE-dimethyl carbonate (PFPE-DMC), as a pale yellow translucent liquid. (Yield: 85%+) Fourier transform infrared spectroscopy (FTIR) (neat): 2886 cm⁻¹ (C-H), 1752 cm⁻¹

(C=O), 1184 cm^{-1} (C-H), 1085 cm^{-1} (C-O). ^1H nuclear magnetic resonance spectroscopy (NMR) (400 MHz; CDCl_3 ; TMS; ppm): $\delta = 3.87$ (s, 6 H), 4.52 (m, 4 H). This procedure was repeated with Fluorolink D10/H, Fomblin ZDOL, and Fomblin ZDOL 4000 to produce PFPE₁₄₀₀-DMC, PFPE₂₀₀₀-DMC, and PFPE₄₀₀₀-DMC respectively (using same molar ratio of reagents) (Reaction scheme shown in Figure 3.6).

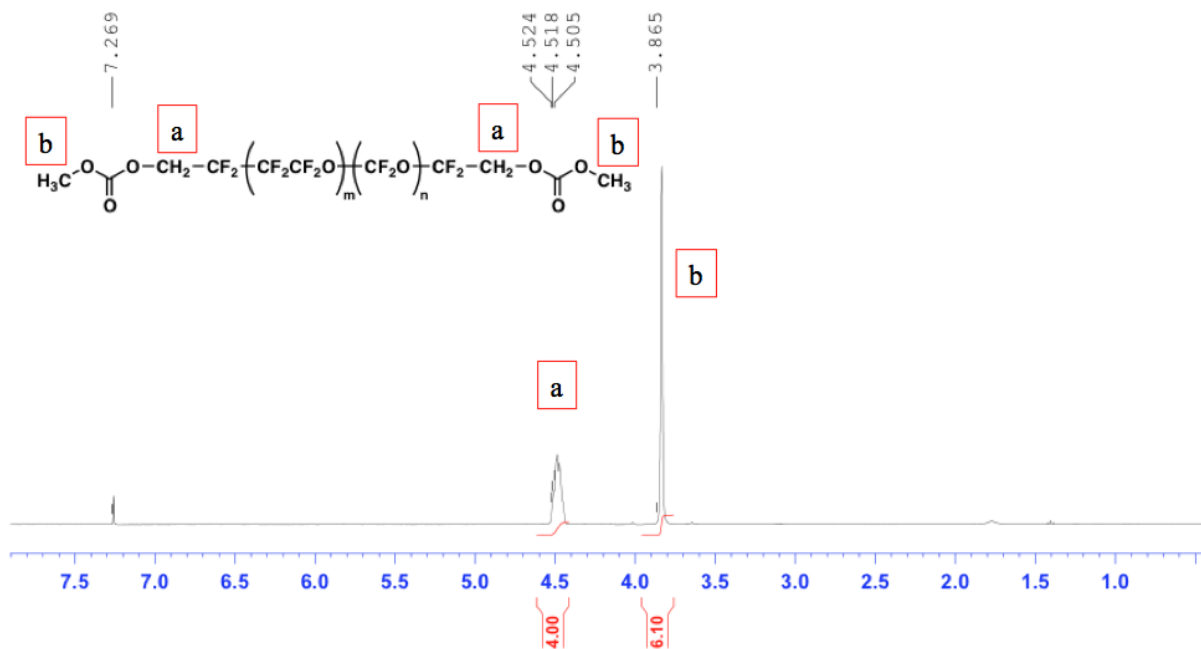


Figure 3.1 ^1H NMR of PFPE₁₀₀₀-DMC in CDCl_3 .

3.3.2 Physical and Thermal Characterization

All materials were dried in argon glove-boxes with oxygen and water at sub-ppm levels for 24 h. Afterwards, LiTFSI was added directly to the PFPE samples and stirred at room temperature overnight. Li-ion concentration in PFPE electrolyte was determined using inductively coupled plasma mass spectroscopy (ICPMS) after excess non-solvated LiTFSI was removed through centrifugation. Thermogravimetric analysis (TGA) was performed using a Perkin Elmer, Pyris 1 TGA apparatus. Scans were made from 20 $^\circ\text{C}$ to 600 $^\circ\text{C}$ with a heating rate of 10 $^\circ\text{C}$ /minute. T_g 's, crystallization temperatures (T_c 's), and melting temperature (T_m 's)

were measured using differential scanning calorimetry (DSC) (TA Instruments, DSC Q 200) in air using the method of heat/cool/heat at a heating and cooling rate of 10°C and 5°C/minute respectively, over a temperature range of -150 °C to 100 °C. The T_g was determined using the midpoint method on the second heating cycle thermogram. The T_c and T_m were determined as the peak maximum and minimum of the first cooling and second heating cycle respectively. Sustained burning characteristics and flash point data were determined using a Rapid Flash Tester in accordance with ASTM D-4206 and ASTM D3278 respectively. FTIR spectroscopy was performed using a Bruker ALPHA FT-IR spectrometer in attenuated total reflectance (ATR) mode (from 500 to 4000 cm^{-1} at resolution of 4 cm^{-1}).

3.3.3 NMR Characterization of PFPEs

The chemical structure and analysis of a ^{19}F NMR spectrum of PFPE was previously discussed in Chapter 2. The number of perfluoroethylene repeating units, m , the number of perfluoromethylene repeating units, n , and the number of terminal units are determined by integration of peaks observed in the ^{19}F NMR spectrum of PFPE.²³ For example, Figure 3.2 and Table 3.1 describe PFPE₁₀₀₀-diol (the subscripts and hyphen after PFPE indicate the molar masses of the polymers in g/mol and their end-groups respectively) and assign peaks a-h to the perfluoroethylene repeating unit, the perfluoromethylene repeating unit, and the terminal unit. The ratio $m : n$ is calculated to be 7 : 3 and the total number of repeating units, $m + n$, is 10. This analysis was repeated for all different molecular weights of PFPE-diols (PFPE₁₄₀₀-diol, PFPE₂₀₀₀-diol, and PFPE₄₀₀₀-diol) studied (Table 3.2). Because the synthesis of PFPE-DMC was based on end group modification without changes to the oligomer backbone, the number of repeating units is assumed to be the same as its PFPE-diol reagent. In other words, PFPE₁₀₀₀-

DMC, PFPE₁₄₀₀-DMC, PFPE₂₀₀₀-DMC, and PFPE₄₀₀₀-DMC have the identical m:n ratio as PFPE₁₀₀₀-diol, PFPE₁₄₀₀-diol, PFPE₂₀₀₀-diol, and PFPE₄₀₀₀-diol.

Table 3.1 Chemical shift analysis of a ¹⁹F NMR spectrum of PFPE₁₀₀₀-diol. Peaks a-h correspond to peaks a-h in Figure 3.2.

Peak	Chemical Shift	Peak Assignment to PFPE structure	Monomer	Ratio
a	-51.7 ppm	-OCF ₂ CF ₂ OCF ₂ OCF ₂ CF ₂ O-	$\left(\text{CF}_2\text{O}\right)_n$	n = 3
b	-53.4 ppm	-OCF ₂ CF ₂ OCF ₂ OCF ₂ OCF ₂ -		
c	-55.1 ppm	-CF ₂ OCF ₂ OCF ₂ OCF ₂ OCF ₂ -		
d	-80.6 ppm	-OCF ₂ CF ₂ OCF ₂ CH ₂ OH	Terminal Group	2
e	-82.8 ppm	-OCF ₂ OCF ₂ CH ₂ OH		
f	-88.9 ppm	-OCF ₂ CF ₂ OCF ₂ CF ₂ OCF ₂ CF ₂ O-	$\left(\text{CF}_2\text{CF}_2\text{O}\right)_m$	m = 7
g	-90.6 ppm	-OCF ₂ CF ₂ OCF ₂ CF ₂ OCF ₂ OCF ₂ -		
h	-92.0 ppm	-CF ₂ OCF ₂ OCF ₂ CF ₂ O CF ₂ OCF ₂ -		

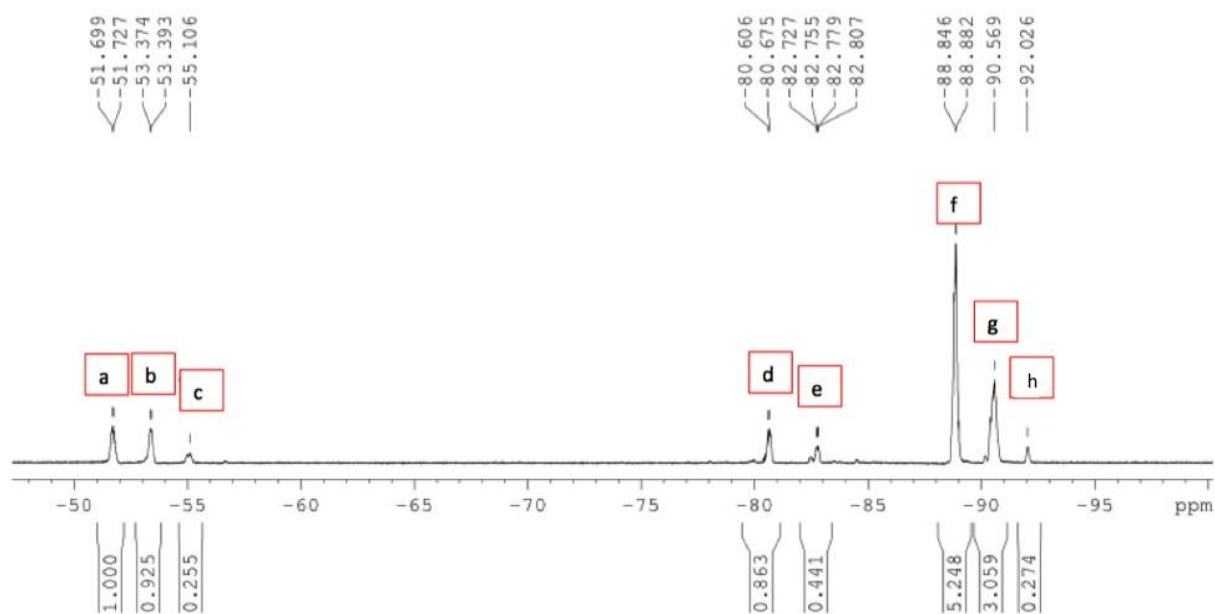


Figure 3.2 ¹⁹F NMR of PFPE₁₀₀₀-diol. Peak labels a-h correspond to peaks a-h in Table 3.1

Table 3.2 Determination of m:n and number of repeating units for PFPE₁₄₀₀-diol, PFPE₂₀₀₀-diol, and PFPE₄₀₀₀-diol

PFPE	m : n	Number of repeating units
PFPE ₁₄₀₀ -diol	10:3	13
PFPE ₂₀₀₀ -diol	5 : 7	24
PFPE ₄₀₀₀ -diol	1 : 1	48

3.3.4 Electrochemical Characterization

Ionic conductivity and cyclic voltammetry (CV) measurements were made via a 16-channel Bio-Logic VMP3 potentiostat. Cyclic voltammetry measurements were conducted in Li metal/electrolyte/stainless steel standard coin cells. Conductivity measurements were obtained using a procedure similar to that previously reported by Teran and coworkers²⁴ and was also previously described in Chapter 2. Alternatively, conductivity can be calculated by impedance measurement of symmetric Li/Li cells. The ionic conductivity, σ , values reported for the symmetric lithium cells were calculated by normalizing the measured resistance by the volume of electrolyte in the porous separator

$$\sigma = \frac{L}{RA\varepsilon} \dots\dots\dots\text{equation 3.1}$$

where L , R , A , and ε is the length, resistance, cross sectional area, and the porosity of the separator respectively.

3.3.5 Determination of t^+ using Alternating Current Impedance Spectroscopy

The lithium-ion transference number, t^+ , was measured using Li/electrolyte/Li symmetrical cells assembled in 2325 coin cell hardware. Alternating current (AC) impedance spectroscopy measurements were made between 38.7 °C and 85.5 °C in the frequency range of 1 MHz to 1 mHz, with a 20 mV excitation signal. t^+ was evaluated with the procedure described by Bouchet and coworkers,²⁵ where the impedance spectrum (Figure 3.3) is modeled by an electrical equivalent circuit (Figure 3.4) that permits the extraction of the electrolyte and the diffusion resistance, R_e and R_d , respectively. The t^+ is calculated by

$$t^+ = \frac{R_e}{R_e + R_d} \dots\dots\dots\text{equation 3.2}$$

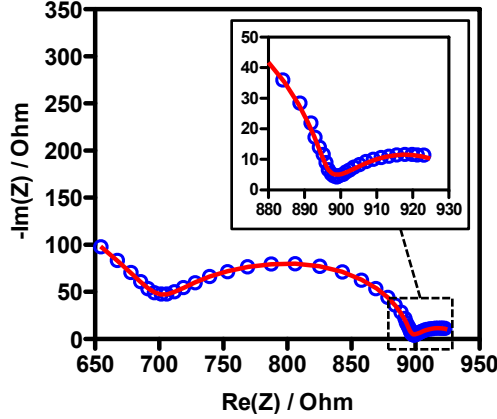


Figure 3.3 Nyquist plot obtained from AC Impedance for PFPE₁₀₀₀-DMC electrolyte. Open symbols represent the experimental spectrum while the line is the modeling using electrical equivalent circuit.

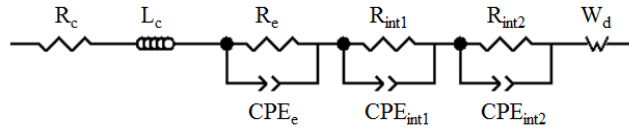


Figure 3.4 Electrical model used to fit the Nyquist plot.

This technique has also been compared with the steady state technique which combines a direct current (DC) polarization with AC measurements.²⁶ This method consists of an initial ac impedance measurement to determine the lithium interfacial resistance, R_{int}^0 followed by a chronoamperometry using a dc voltage, ΔV , of 20 mV to monitor the current evolution over time from its initial I^0 value. When a steady state current, I^∞ , is obtained the interfacial resistance, R_{int}^{∞} , is measured. t^+ is determined by:

$$t^+ = \frac{I^\infty(\Delta V - I^0 R_{int}^0)}{I^0(\Delta V - I^\infty R_{int}^\infty)} \dots \dots \dots \text{equation 3.3}$$

For accuracy, the interfacial resistance of the symmetrical cells was measured every hour during the chronoamperometry period by applying an AC signal to the DC one. These intermittent measurements enable one to follow the t^+ evolution over time. The electrical model takes into account the apparatus resistance (R_c) and inductance (L_c). The electrolyte resistance (R_e) is in

parallel with the electrolyte pseudocapacitance (CPE_e , Constant Phase Element). The Lithium/electrolyte interface phenomena can be decomposed into two contributions, one due to the passive layer modeled by R_{int1} in parallel with CPE_{int1} and the other one, R_{int2} in parallel with CPE_{int2} , corresponding to the electronic transfer. W_d is a short Warburg element related to the diffusion resistance (R_d).

In addition to AC impedance spectroscopy, the transference number of PFPE₁₀₀₀-DMC was also determined using a potentiostatic polarization technique (Figure 3.5).²⁶ Similar high transference values for the lithium cation were observed. Both approaches were also used to determine t^+ of polystyrene-block-poly(ethylene oxide) (also known as SEO) electrolytes.

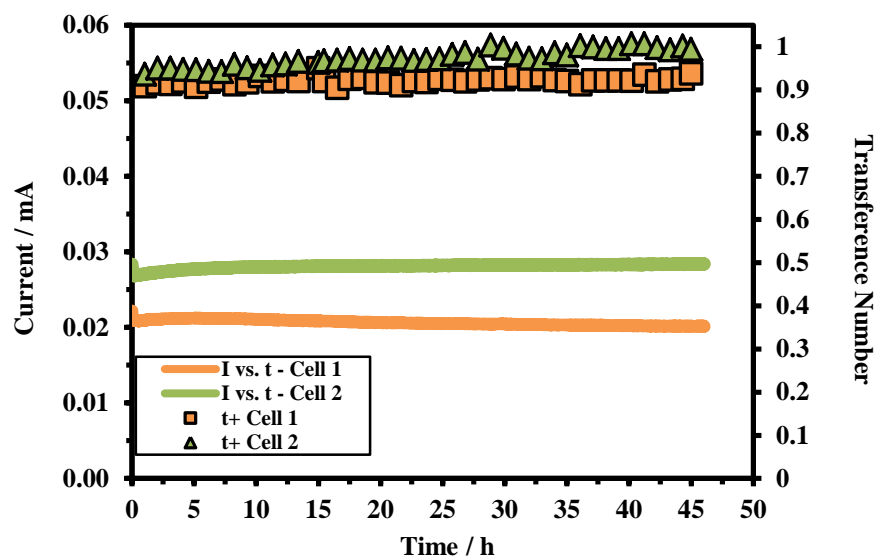


Figure 3.5 t^+ measurements of cells containing 50 μm PFPE₁₀₀₀-DMC electrolyte using the Bruce and Vincent method using a 20 mV polarization at 38.8 °C.

3.3.6 Electrochemical Coin Cell Testing

Slurries containing 85.0 weight (wt.) % NMC, 7.0 wt. % AB, and 8.0 wt. % PVDF dispersed in NMP solvent were prepared. NMC laminates were prepared by casting the slurries onto aluminum foil using a doctor blade. The laminates were subsequently punched into 14.3

mm diameter discs and dried completely before electrochemical studies. Active material loading was, on average, 1.9 mg/cm^2 . Coin cells were assembled in standard 2325 coin cell hardware. Lithium foil was used as anode material and NMC was used as active material in the cathode. Celgard 2500, punched into circles with a diameter of 20.6 mm, served as physical separators. The entire procedure was performed in an argon-filled glove box. Cell testing was conducted on a Maccor Battery Cycler connected with a ThermoTron Environmental Chamber set at 30°C . The batteries were cycled between 2.8 and 4.3 V with equivalent charge and discharge rates. Four formation cycles were performed at C/20 before the cycling rates were increased to C/15, C/10 and C/8 respectively.

3.4 Results and Discussion

Hydroxy-terminated PFPEs (PFPE-diols) with nominal molecular weights of 1000, 1400, 2000, and 4000 g/mol were purchased from Solvay Solexis. In addition to studying these materials, we modified the terminal groups of PFPE chains to more closely resemble chemistries that have successfully been used in batteries, thereby increasing compatibility with current battery systems. A one-step reaction with these oligomers and methyl chloroformate in the presence of TEA in 1,1,1,3,3-pentafluorobutane resulted in the formation of methyl carbonate-terminated PFPEs (PFPE-DMCs) (Figure 3.6). The PFPEs studied are listed in Table 3.3, along with the corresponding degrees of polymerization (DP) and T_g 's.

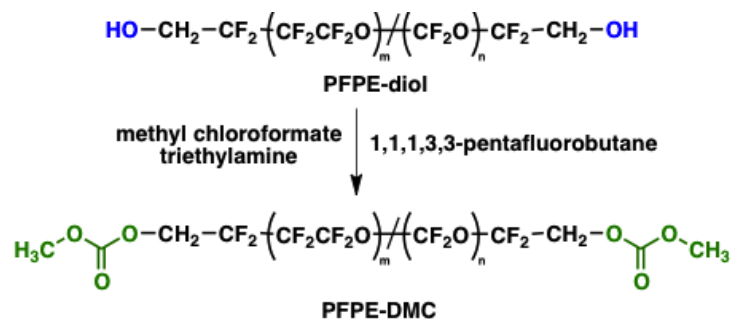


Figure 3.6 Chemical reaction scheme describing the synthesis of PFPE-DMC from PFPE-diol.

Table 3.3 PFPEs studied with their corresponding degrees of polymerization and T_g 's.

PFPE	DP	T_g (°C)
PFPE ₁₀₀₀ -diol	10	-89
PFPE ₁₄₀₀ -diol	13	-98
PFPE ₂₀₀₀ -diol	24	-112
PFPE ₄₀₀₀ -diol	48	-117
PFPE ₁₀₀₀ -DMC	10	-95
PFPE ₁₄₀₀ -DMC	13	-101
PFPE ₂₀₀₀ -DMC	24	-113
PFPE ₄₀₀₀ -DMC	48	-118

The flammability evaluation of electrolytes was determined based on their thermal stability, fire sustainability, and flash point. Figure 3.7 shows the TGA thermograms of PFPE₁₀₀₀-diol and PFPE₁₀₀₀-DMC compared to pure DMC, its small molecule analogue. DMC, a volatile liquid, experiences 5 % wt. loss at 34 °C (denoted as T_d (5%)), and 100 % of the material was vaporized or degraded in the vicinity of 80 °C. In addition, DMC has a flash point below ambient temperature²⁷ and could be easily ignited and sustain a fire (Table 3.4), posing both flammability and over pressurization hazards in lithium batteries. In contrast, PFPE₁₀₀₀-diol and PFPE₁₀₀₀-DMC demonstrate neither volatility nor thermal degradation below 200 °C; T_d values measured for these materials are 210 °C and 212 °C respectively. Flash points could not be detected for PFPE₁₀₀₀-diol and PFPE₁₀₀₀-DMC within our experimental window (25 - 200 °C), and they could not be ignited. The flash point of conventional lithium battery electrolytes (1:1

ethylene carbonate (EC)/DMC by volume) is 24 °C,²⁸ slightly higher than that of DMC, the non-flammability and thermal stability of PFPEs can significantly improve the safety of Li-ion batteries.

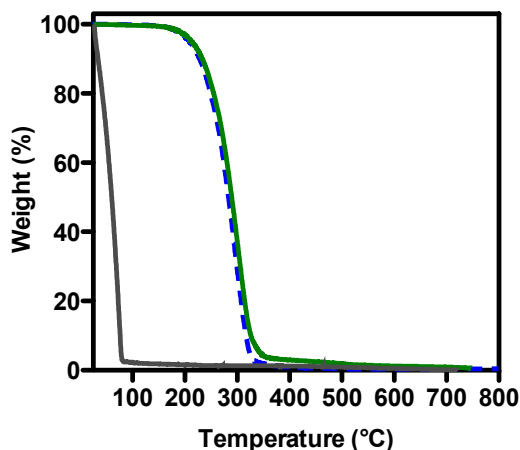


Figure 3.7 Thermogravimetric curves for thermal decompositions of DMC (solid grey), PFPE₁₀₀₀-diol (dash blue), and PFPE₁₀₀₀-DMC (solid green).

Table 3.4 Corresponding decomposition temperature (5%), sustained burning characteristics, and flash points of these materials.

Electrolyte	$T_d(5\%)$ (°C)	Sustained Burning Time (s)	Flash Point (°C)
DMC	34	221 ± 7	18
PFPE ₁₀₀₀ -diol	210	No burning observed	None < 200
PFPE ₁₀₀₀ -DMC	212	No burning observed	None < 200

ICPMS was used to determine the solubility limit of LiTFSI in the PFPE electrolyte. Above this limit salt precipitation occurs, leading to heterogeneous opaque mixtures. In Figure 3.8A we plot the maximum salt concentration in terms of molarity and r_{max} , where r is defined as the molar ratio of Li-ions to perfluoro-alkylene oxide moieties (both perfluoroethylene and perfluoromethylene) in the chain, versus the nominal PFPE molecular weight. The relationship between both molarity and r_{max} and molecular weight for both PFPE-diols and PFPE-DMCs show an exponential decay of LiTFSI maximum loading as molecular weight increases.

However, when salt concentration is normalized by the concentration of terminal groups and plotted as R_{max} , defined as the molar ratio of Li-ions to hydroxyl and methyl carbonate moieties (Figure 3.8A inset), the maximum concentration is nearly independent of molecular weight. This analysis shows that the carbonate functionalization allows for nearly double the maximum salt loading relative to PFPE-diols, presumably because carbonate moieties interact more favorably with Li-ions than hydroxyl groups. To confirm our claim, FTIR was used to study the interactions between LiTFSI and PFPE polymers. Figure 3.8B shows FTIR spectra of PFPE₁₀₀₀-DMC blends with LiTFSI at various concentrations, compared with pure LiTFSI and PFPE₁₀₀₀-DMC. A shift in the C=O signal at 1770 cm⁻¹ to lower wavenumbers as LiTFSI concentration increases is observed. The carbonyl peak shifts systematically with increasing salt concentration and is at approximately 1750 cm⁻¹ when $r = 0.08$. This observation is attributed to interactions between the carbonate moieties and Li-ion. In contrast, the addition of LiTFSI to PFPE₁₀₀₀-diol has no discernible effect on the measured FTIR spectra (Figure 3.9). Although overlap of the signals from PFPE₁₀₀₀-DMC and LiTFSI precludes the observation of LiTFSI peak shifts in this region as the salt is being solvated, the decreased intensities at 1350 cm⁻¹ in PFPE₁₀₀₀-DMC/LiTFSI blends is consistent with the presence of dissociated Li-ions and TFSI ions.²⁹⁻³¹

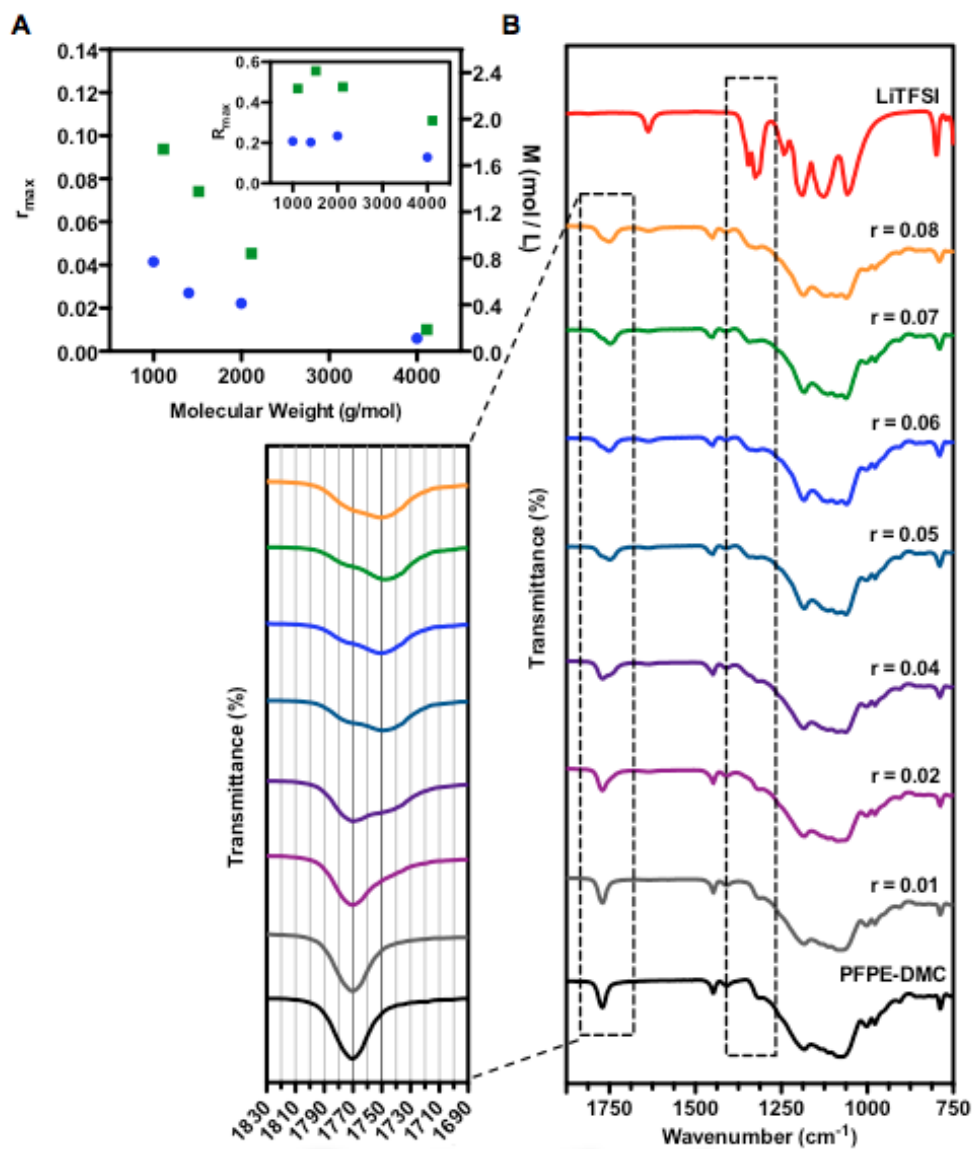


Figure 3.8 Characterization of LiTFSI loading in PFPE electrolytes. (A) Maximum LiTFSI loading in PFPE-diols (blue) and PFPE-DMCs (green) expressed in r_{max} , the molar ratio of Li-ions to repeating fluoroether units and molarity, and in R_{max} (inset), the molar ratio of Li-ions to end group functionalities, as a function of molecular weight. (B) FTIR spectra of PFPE₁₀₀₀-DMC/LiTFSI blends at different concentrations.

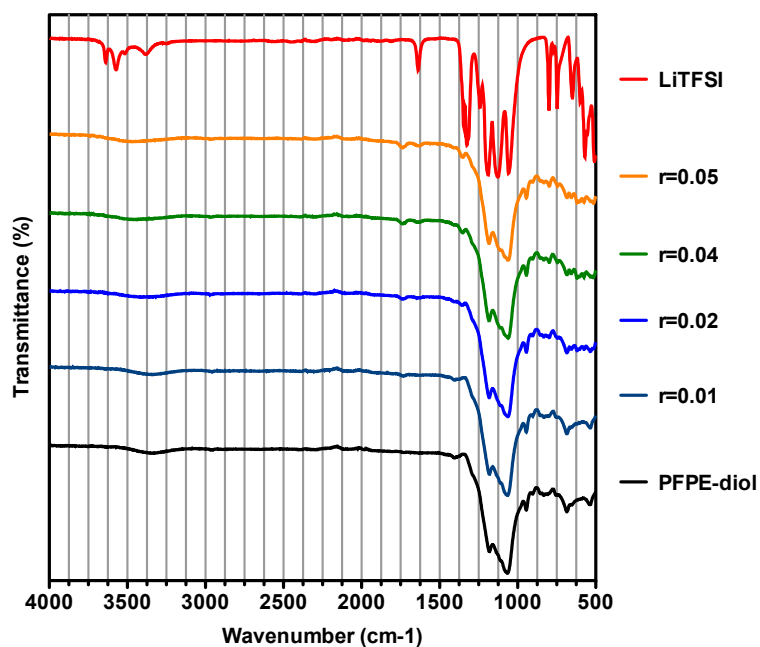


Figure 3.9 FTIR of PFPE₁₀₀₀-diol/LiTFSI blends compared to pure PFPE₁₀₀₀-diol and LiTFSI.

Ionic conductivities, measured via AC impedance spectroscopy, of various PFPE-diol and PFPE-DMC mixtures with LiTFSI at 30 °C are shown in Figure 3.10. By plotting the conductivities as a function of normalized concentration r , we show that although end group composition heavily impacts LiTFSI solvation, it does not significantly influence ionic conduction. All electrolytes appear to demonstrate a logarithmic dependence of conductivity on r that plateaus near $r = 0.08$. Analogous trends have been reported for structurally similar PEO electrolytes.³² In PEO systems, Li-ion transport is predominantly dictated by ion-chain interactions localized on the oligomer backbone, and the conductivity reaches a maximum at a LiTFSI concentration of around $r = 0.085$.^{32,33} It is important to note, however, that the conductivities of the PFPE systems tested are limited by their maximum salt loading, and no maximum in conductivity is observed. Thus PFPE₁₀₀₀-DMC, which can solvate the highest salt loading, is the most promising electrolyte among those tested, reaching a conductivity of $2.5 \times 10^{-5} \text{ Scm}^{-1}$ at 30 °C. These conductivity values are significantly lower than conventional

carbonate electrolytes (10^{-3} S/cm), but are comparable to that of PEO-based electrolytes reported polymeric electrolytes at room temperature.⁴

More complete electrochemical characterization was performed on PFPE₁₀₀₀-DMC at $r = 0.04$. Figure 3.10B illustrates the temperature-dependent conductivity behavior of this electrolyte. We found that conductivity increases with increasing temperature, as is typical of macromolecular electrolytes. The Vogel-Tamman Fulcher (VTF) equation, which is typically used to describe the dependence of viscosity on temperature near its T_g , is also often used to describe the temperature-dependence of conductivity. It is expressed as

$$\sigma(T) = \frac{A}{\sqrt{T}} \exp\left(\frac{-B}{R(T-T_0)}\right) \dots \dots \dots \text{equation 3.4}$$

where σ is the ionic conductivity, A is a constant proportional to the number of charge carriers, B is equivalent to the activation energy for ion motion, R is the gas constant, T is the experimental temperature, and T_0 is an empirical reference temperature³⁴. It is clear from Figure 3.10B that the conductivity of PFPE₁₀₀₀-DMC is a weak function of temperature with $B = 0.47$ kJmol⁻¹ (for complete table of calculated VFT parameters, see Table 3.5). This indicates a very low activation barrier for ion conduction. In fact, the measured conductivity at 120 °C is within a factor of 3 of that at 30 °C. The modest increase in conductivity with temperature coupled with its inherent thermal stability reduces the risk of detrimental side reactions that are often exothermic and lead to thermal runaway in conventional liquid Li-ion batteries.

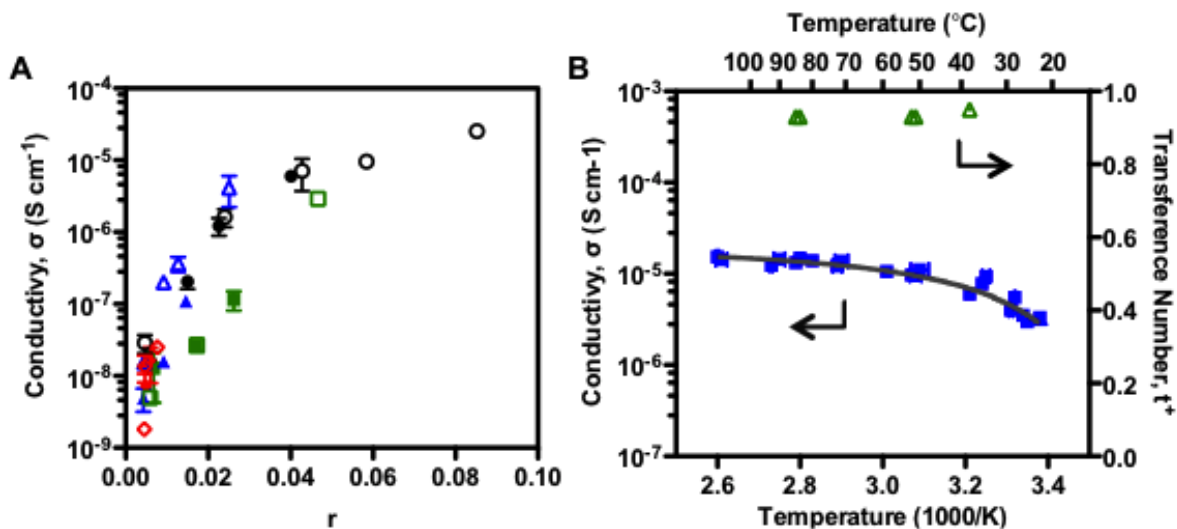


Figure 3.10 Electrochemical behavior of PFPE electrolytes. (A) Ionic conductivities of PFPE₁₀₀₀-diol (filled black circles), PFPE₁₄₀₀-diol (filled green squares), PFPE₂₀₀₀-diol (filled blue triangles), PFPE₄₀₀₀-diol (filled red diamonds), PFPE₁₀₀₀-DMC (open black circles), PFPE₁₄₀₀-DMC (open green squares), PFPE₂₀₀₀-DMC (open blue triangles), PFPE₄₀₀₀-DMC (open red diamonds) with LiTFSI at 30 °C as a function of r . (B) t^+ (open green triangles) and temperature-dependent conductivity (filled blue squares) of PFPE₁₀₀₀-DMC. Conductivity follows VFT regression (grey, parameters listed in Table 3.5).

Table 3.5 VFT parameters calculated for PFPE₁₀₀₀-DMC electrolytes

Parameter	Value	Standard Deviation
A ((S/cm)K ^{0.5})	5.0×10^{-4}	6.7×10^{-5}
B (kJ/mol)	0.47	0.13
T_0 (K)	271.3	6.9

In simple conductors with only one charged species, one observes Ohm's Law in the limit of small dc potentials. The presence of two ions in electrolytes, however, generally results in large deviations from Ohm's law due to concentration polarization. To our surprise, we found that PFPE₁₀₀₀-DMC/LiTFSI electrolytes at $r = 0.04$ exhibited behavior that was very close to that of a simple conductor. The electrolyte was sandwiched between two Li foil electrodes and a steady potential of 0.02 V was applied for about 45 h at 38.8 °C. The electrolyte resistance (including both bulk and interfacial contributions) was measured at various times during the

experiment by ac impedance. The measured resistance after 6 h was $2061.4 \Omega/\text{cm}^2$ and the measured current density, i_m , was $8.84 \times 10^{-6} \text{ A}/\text{cm}^2$. The expected current based on Ohm's law, i_o , is $9.70 \times 10^{-6} \text{ A}/\text{cm}^2$, *i.e.* $i_m/i_o = 0.91$. This implies that most of the current in our electrolyte is carried by the cation. In other words, the Li-ion transference number, t^+ , a transport property that has a dramatic effect on battery performance, is in the vicinity of unity. Two approximate approaches for determining the transference number were used. Both methods yield t^+ values between 0.91 and 1.0 in the temperature range of interest. To our knowledge, this is among the highest t^+ values reported for solutions containing lithium salts, and one of the few near-unity t^+ electrolytes with conductivities above $10^{-6} \text{ S}/\text{cm}$ at room temperature. To establish the validity of our approaches for measuring t^+ , we repeated our procedure using LiTFSI and the commonly investigated SEO electrolytes (where Li-ion is contained exclusively within the PEO block). The t^+ value of this electrolyte was about 0.12 (Figure 3.11), consistent with literature reports that t^+ values for LiTFSI/PEO electrolytes are between 0.1 and 0.3.^{35,36} In the future, we will use more rigorous approaches to measure t^+ .³⁷ While the relatively low conductivity of PFPE electrolytes may hinder power capacities, the near unity transference number may mitigate some of these shortcomings: theoretical calculations show that materials with high t^+ values exhibit better battery performance than those possessing greater conductivity but a lower t^+ .³⁸ The absence of polarization also reduces the risk of lithium plating and dendrite formation.^{35,39} The Li-ion transference number of conventional carbonate electrolytes usually ranges between 0.1 and 0.5;¹⁶ concomitant salt concentration gradients across the electrolyte limit battery life and power density. These t^+ values are mainly due to strong interactions between oxygen atoms in the solvent molecules and lithium cations. We propose two possible reasons for our observation of a high transference number: (1) fluorine-containing functional groups on the PFPE backbone

interact strongly with the fluorinated anion and reduce its mobility, and (2) the delocalization of electron density caused by the fluorine moieties reduces the nucleophilicity of the oxygen atoms in the electrolyte, leading to their decreased binding strength to Li-ion, facilitating cation transport across the medium. It is evident that both the PFPE main chain and the functional end groups play important roles in ion transport; conductivity at a given value of salt concentration is similar for widely different PFPE electrolytes (Figure 3.10) while salt solubility limits depend mainly on end group type and concentration (Figure 3.8).

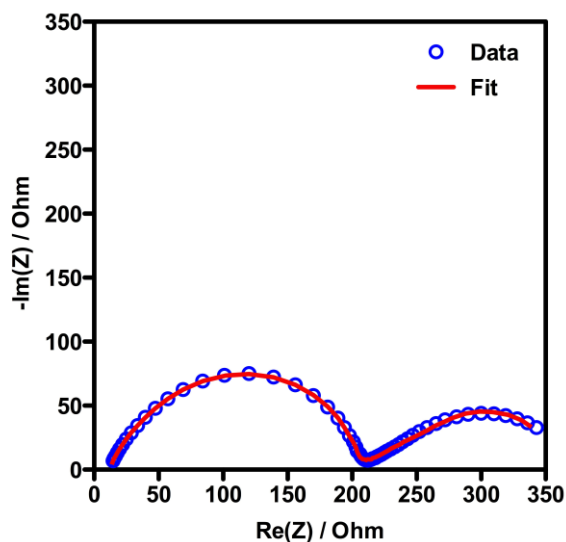


Figure 3.11 Nyquist plot obtained from AC Impedance for SEO polymer electrolyte. t^+ was calculated to be 0.12.

To investigate the viability of using PFPE electrolytes in Li batteries, standard coin cell batteries were built using PFPE₁₀₀₀-DMC at $r = 0.04$ as the electrolyte. Through cyclic voltammetry, we found that PFPE₁₀₀₀-DMC is electrochemically stable up to 4.3V (Figure 3.12), allowing for the use of high voltage cathode materials such as LiNMC. Lithium metal and LiNMC were therefore chosen as the anode and cathode respectively. Cycling tests were performed at 30°C at different charge rates (described as C/n, where n is the number of hours allotted to a full discharge of the theoretical cathode capacity ‘C’). Figure 3.13A shows the

typical discharge profiles of a Li/(PFPE1000-DMC/LiTFSI)/LiNMC battery at C/20, C/15, C/10, and C/8. Capacities of 145, 140, 120, and 105 mAh/g were obtained at these respective rates. At C/10 the capacity of the same half cell described in Figure 3.13 replaced by a conventional EC/DEC electrolyte is 150 mAh/g (Figure 3.14). The results of successive cycling experiments at different C-rates (average behavior of 4 cells) are shown in Figure 3.13B. The stable charge and discharge capacities for each C-rate indicate good compatibility between the PFPE and typical Li-ion battery cathode electrodes. Batteries that can be charged and discharged on the time scale of 8 h are immediately relevant as back up units for solar panels. Further studies related to improving and optimizing electrolyte conductivity, rate capability, and testing battery performance under non-standard temperature conditions are therefore currently under investigation.

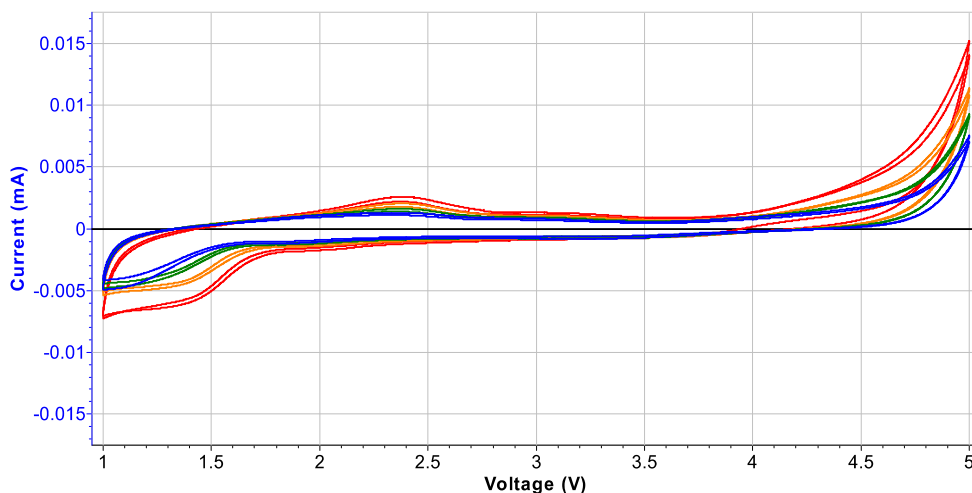


Figure 3.12 Cyclic voltammograms of PFPE₁₀₀₀-DMC at 1 mV/s from a Li/Electrolyte/Stainless steel cell obtained at every fifth cycle at 40 °C (blue), 60 °C (green), 80 °C (orange), and 100 °C (red).

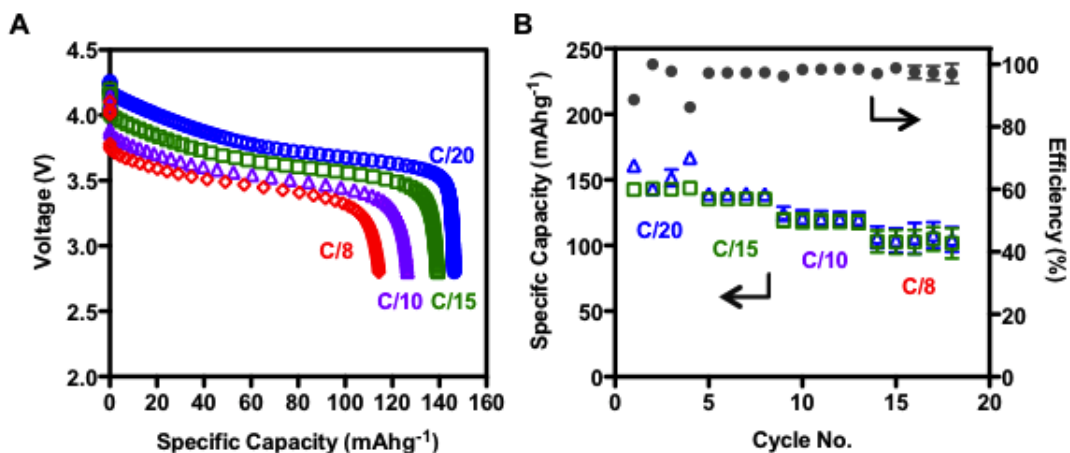


Figure 3.13 Cyclability of Li/PFPE₁₀₀₀-DMC-LiTFSI/LiNMC cells. (A) Discharge profiles obtained at 30 °C at different rates from C/20 to C/8 for a typical prototype Li/PFPE₁₀₀₀-DMC-LiTFSI/LiNMC. (B) Cycle performance of battery prototypes showing discharge (open green squares), charge (open blue squares) capacities, as well as overall efficiencies (filled grey circles).

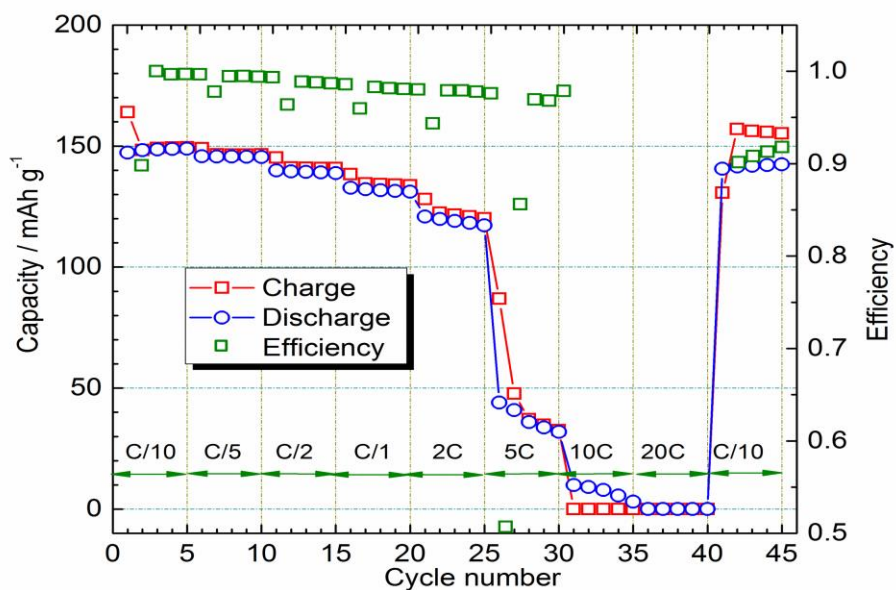


Figure 3.14 Cycle performance of LiPF₆-EC/DEC (1 M, 1 : 2 vol, Daikin Industries) batteries.

In conclusion, we have successfully demonstrated the use of PFPEs as a platform for the development of intrinsically safe lithium battery electrolytes. To our knowledge, this is the first example that shows that PFPEs can be used as a major component of operating batteries. Designing electrolytes that solvate the fluorinated anion represents a radical departure from the established approach that is focused on solvating the lithium cation. By developing PFPE-DMC, we have incorporated compatibility with lithium salts in an inherently nonflammable material. The resulting electrolytes exhibit reasonable conductivity and unprecedented transference numbers. Their compatibility with standard battery electrodes provides the opportunity for seamless integration into current manufacturing infrastructure. While much work remains to be done, we believe that this work represents a significant step towards safer, high energy lithium batteries, and opens the door for the development of new electrolytes that can be tailored to address the persistent challenges of Li-ion technologies

3.5 Future Directions for PFPE-Dimethyl Carbonate Electrolytes

Development of PFPE-DMC electrolytes demonstrates viability in cell prototypes similar to commercial systems and exhibit significantly improved safety relative to small molecule alkyl carbonates. Ongoing research directions continue to investigate compatible electrodes with PFPE-DMC; anodes such as carbon are of especially high interest since they can replace the use of unstable lithium metal. Further studies into the ion transport mechanism of PFPE-diol and PFPE-DMC in order to elucidate the high t^+ would also deepen the understanding of the effect of polymer structure on bulk ion conduction; this would ultimately provide better synthetic and electrochemical optimization of battery electrolytes for large-scale applications. These studies are discussed in greater detail in Chapter 5.

REFERENCES

- (1) Tarascon, J. M.; Armand, M. *Nature* **2001**, *414*, 359.
- (2) Goodenough, J. B.; Park, K.-S. *Journal of the American Chemical Society* **2013**, *135*, 1167.
- (3) Cheng, F. Y.; Liang, J.; Tao, Z. L.; Chen, J. *Advanced Materials* **2011**, *23*, 1695.
- (4) Goodenough, J. B.; Kim, Y. *Chemistry of Materials* **2010**, *22*, 587.
- (5) Hammami, A.; Raymond, N.; Armand, M. *Science* **2003**, *301*, 635.
- (6) Mandal, B. K.; Padhi, A. K.; Shi, Z.; Chakraborty, S.; Filler, R. *Journal of Power Sources* **2006**, *161*, 1341.
- (7) Armand, M.; Endres, F.; MacFarlane, D. R.; Ohno, H.; Scrosati, B. *Nature Materials* **2009**, *8*, 621.
- (8) Lombardo, L.; Brutti, S.; Navarra, M. A.; Panero, S.; Reale, P. *Journal of Power Sources* **2013**, *227*, 8.
- (9) Egashira, M.; Todo, H.; Yoshimoto, N.; Morita, M. *Journal of Power Sources* **2008**, *178*, 729.
- (10) Song, J. Y.; Wang, Y. Y.; Wan, C. C. *Journal of Power Sources* **1999**, *77*, 183.
- (11) Wu, L.; Song, Z.; Liu, L.; Guo, X.; Kong, L.; Zhan, H.; Zhou, Y.; Li, Z. *Journal of Power Sources* **2009**, *188*, 570.
- (12) Nagasubramanian, G.; Orendorff, C. J. *Journal of Power Sources* **2011**, *196*, 8604.
- (13) Naoi, K.; Iwama, E.; Ogihara, N.; Nakamura, Y.; Segawa, H.; Ino, Y. *Journal of The Electrochemical Society* **2009**, *156*, A272.
- (14) Croce, F.; Appetecchi, G. B.; Persi, L.; Scrosati, B. *Nature* **1998**, *394*, 456.
- (15) Fergus, J. W. *Journal of Power Sources* **2010**, *195*, 4554.
- (16) Ghosh, A.; Wang, C.; Kofinas, P. *Journal of The Electrochemical Society* **2010**, *157*, A846.
- (17) Capuano, F.; Croce, F.; Scrosati, B. *Journal of The Electrochemical Society* **1991**, *138*, 1918.

- (18) Appetecchi, G. B.; Zane, D.; Scrosati, B. *Journal of The Electrochemical Society* **2004**, *151*, A1369.
- (19) Evans, J.; Vincent, C. A.; Bruce, P. G. *Polymer* **1987**, *28*, 2324.
- (20) Watanabe, M.; Nishimoto, A. *Solid State Ionics* **1995**, *79*, 306.
- (21) Hu, Z.; Chen, L.; Betts, D. E.; Pandya, A.; Hillmyer, M. A.; DeSimone, J. M. *J Am Chem Soc* **2008**, *130*, 14244.
- (22) Rolland, J. P.; Dam, R. M. V.; Schorzman, D. A.; Quake, S. R.; DeSimone, J. M. *Journal of the American Chemical Society* **2004**, 2322.
- (23) Tchistiokov, A.; Fontana, S.; Tonelli, C.; Solvay Solexis S.p.A: US 2006; Vol. US 2006/0009660 A1.
- (24) Teran, A. A.; Tang, M. H.; Mullin, S. A.; Balsara, N. P. *Solid State Ionics* **2011**, *203*, 18.
- (25) Bouchet, R.; Lascaud, S.; Rosso, M. *Journal of The Electrochemical Society* **2003**, *150*, A1385.
- (26) Bruce, P.; Vincent, C. A. *J. Electroanal. Chem.* **1987**, *225*, 1.
- (27) Mikolajczak, C.; Kahn, M.; White, K.; Long, R. T. *Lithium-Ion Batteries Hazard and Use Assessment* The Fire Protection Research Foundation 2011.
- (28) Hori, M.; Aoki, Y.; Maeda, S.; Tatsumi, R.; Hayakawa, S. *ECS Transactions* **2010**, *25*, 147.
- (29) Huang, W.; Wheeler, R. A.; Frech, R. *Spectrochimica Acta Part A: Molecular Spectroscopy* **1994**, *50*, 985.
- (30) Rey, I.; Lassegues, J. C.; Grondin, J.; Servant, L. *Electrochimica Acta* **1998**, *43*, 1505.
- (31) Barteau, K. P.; Wolffs, M.; Lynd, N. A.; Fredrickson, G. H.; Kramer, E. J.; Hawker, C. J. *Macromolecules* **2013**, *46*, 8988.
- (32) Panday, A.; Mullin, S.; Gomez, E. D.; Wanakule, N.; Chen, V. L.; Hexemer, A.; Pople, J.; Balsara, N. P. *Macromolecules* **2009**, *42*, 4632.
- (33) Lascaud, S.; Perrier, M.; Vallee, A.; Besner, S.; Prud'homme, J.; Armand, M. *Macromolecules* **1994**, 7469.
- (34) Souquet, J.-L.; Duclot, M.; Levy, M. *Solid State Ionics* **1996**, *85*, 149.

- (35) Bouchet, R.; Maria, S.; Meziane, R.; Aboulaich, A.; Lienafa, L.; Bonnet, J. P.; Phan, T. N. T.; Bertin, D.; Gimes, D.; Devaux, D.; Denoyel, R.; Armand, M. *Nature Materials* **2013**, *12*, 452.
- (36) Edman, L.; Doeff, M. M.; Ferry, A.; Kerr, J.; De Jonghe, L. C. *The Journal of Physical Chemistry B* **2000**, *104*, 3476.
- (37) Ma, Y.; Doyle, M.; Fuller, T. F.; Doeff, M. M.; Jonghe, L. C. D.; Newman, J. J. *Electroanal. Chem.* **1995**, *142*, 1859.
- (38) Doyle, M.; Fuller, T. F.; Newman, J. *Electrochimica Acta* **1994**, *39*, 2073.
- (39) Chazalviel, J. N. *Physical Review A* **1990**, *42*, 7355.

CHAPTER 4

FURTHER CHEMICAL MODIFICATIONS OF PERFLUOROPOLYETHERS

4.1 PFPEs as a Chemical Platform for End Group Functionalization

As shown with the synthesis of perfluoropolyether-dimethyl carbonate (PFPE-DMC) in Chapter 3, the hydroxyl-terminated PFPE (PFPE-diol) provides numerous opportunities for versatile chemical modifications in order to explore different functional groups, which may lead to promising opportunities for improvement of lithium-ion (Li-ion) battery electrolytes. Moieties such as nitriles, ethylene carbonate, sulfones, and ethers have been reported to enhance electrolyte properties such as conductivity, viscosity, thermal stability, voltage stability, and capacity.¹⁻³ Furthermore, through functional groups such as thiols and methacrylates, perfluoropolyethers (PFPEs) can be used as a macro-monomer precursor in the preparation of larger PFPE macromolecules to be used as solid-state or gel PFPE electrolytes, eliminating risks associated with electrolyte leakage from a battery cell. Herein, this chapter is two-fold: Part A focuses on the preparation of PFPEs with a variety of functional groups, affording a systematic study on the effects of electron withdrawing and donating groups on the overall electrolyte viscosity and thermal properties. On the other hand, in Part B, the preparation of crosslinked PFPE electrolytes from PFPE-dimethacrylate and PFPE-dithiol will be discussed.

4.2 Part A: Effect of Functional Groups on Electrolyte Properties

It is clear that understanding molecular underpinnings such as functional groups that govern ion transport and voltage potential in electrolytes is crucial for effective material design; there has been extensive research efforts to develop derivatives of carbonates, ionic liquids, and

polymeric electrolytes containing various chemical moieties in order to systematically study the effects of chemical structure on the bulk physical and electrochemical properties of the electrolyte.⁴⁻⁷

In recent years, much attention has been focused on electrolytes based on ethers such as tetraglyme (TG).^{2,3,8,9} This relatively high molecular weight ether has demonstrated compatibility with lithium metal anodes, low volatility, and stability against oxidation potentials up to 4.5V vs. lithium (Li)/Li⁺. Furthermore, it shows great promise in remaining stable towards reduced oxygen (O₂) species relative to small molecular alkyl carbonates, making it an encouraging electrolyte candidate in lithium-air batteries.² Expanding from our work discussed in Chapter 2 regarding physical blends of PFPE and poly(ethylene glycol) (PEG), therefore, we became interested in studying covalent analogues of these materials, where short ether chains added to functionalize the terminal ends of PFPE polymers. This short ether chain-functionalized PFPE oligomer was obtained commercially as Fluorolink E10.

Herein we report the functionalization of PFPE E10 oligomers with a variety of chemical moieties such as carbonates, allyls, and propargyls. The thermal and physical properties of these materials were studied to gauge their viability as high performance electrolytes for Li-ion batteries.

4.2.1 Materials

Bis(trifluoromethane)sulfonimide lithium salt (LITFSI) (chemical structure found in Chapter 2), triethylamine (TEA), allyl chloroformate, and propargyl chloroformate were all purchased from Sigma Aldrich and used as received. 1,1,1,3,3-pentafluorobutane (from MicroCare Corporation) was reagent grade and used without further purification. Fluorolink E10

(PFPE_{E10}-diol) (chemical structure found in Figure 4.1) were purchased from Santa Cruz Biotechnology and Solvay Solexis and functionalized without further purification.

4.2.2 Experimental

4.2.2.1 Synthesis of PFPE_{E10}-Dimethyl Carbonate

Fluorolink E10 (5 g, 5×10^{-3} moles) and TEA (1.4 mL, 0.01 moles) were dissolved in 1,1,1,3,3-pentafluorobutane (approximately 200 mL) at 0 °C in an ice bath with magnetic stirring under a nitrogen atmosphere (N₂). Methyl chloroformate (0.8 mL, 0.01 moles) was then added dropwise over approximately one minute, after which the mixture was allowed to return to ambient temperature (approximately 25°C) and stirred for 18 h. The resulting mixture was gravity filtered and washed with water three times and brine one time. The organic layer was isolated and evaporated under reduced pressure, and filtered using a 0.45 µm syringe filter, giving the product PFPE_{E10}-dimethyl carbonate (PFPE_{E10}-DMC) as a pale yellow, transparent liquid. (81% yield) IR (neat): 2886 cm⁻¹ (C-H), 1752 cm⁻¹ (C=O), 1184 cm⁻¹ (C-H), 1085 cm⁻¹ (C-O). ¹H NMR ((CD₃)₂CO): 3.54-4.31 ppm (m, 14H)

4.2.2.2 Synthesis of PFPE_{E10}-Diallyl Carbonate

Fluorolink E10 (5 g, 5×10^{-3} moles) and TEA (1.4 mL, 0.01 moles) were dissolved in 1,1,1,3,3-pentafluorobutane (approximately 200 mL) at 0 °C with magnetic stirring under N₂. Allyl chloroformate (1.1 g/mL, 0.01 moles) was then added dropwise over approximately one minute, after which the mixture was allowed to return to ambient temperature and stirred for 18 h. The resulting mixture was gravity filtered and washed with water three times and brine one time. The organic layer was isolated and evaporated under reduced pressure, and filtered using a 0.45 µm syringe filter, giving the product PFPE_{E10}-diallyl carbonate (PFPE_{E10}-DAC) as a pale

yellow, transparent liquid. (85% yield) IR (neat): 2885 cm^{-1} (C-H), 1751 cm^{-1} (C=O), 1183 cm^{-1} (C-H), 1067 cm^{-1} (C-O). ^1H NMR ($(\text{CD}_3)_2\text{CO}$): 3.55-4.11ppm (m, 50H), 4.63ppm (m, 2H), 5.25ppm (d, 1H), 5.36ppm (d, 1H), 5.98ppm (m, 1H)

4.2.2.3 Synthesis of PFPE_{E10}-Dipropargyl Carbonate

Fluorolink E10 (5 g, 5×10^{-3} moles) and TEA (1.4 mL, 0.01 moles) were dissolved in 1,1,1,3,3-pentafluorobutane at 0 °C under magnetic stirring in N_2 . Propargyl chloroformate (1.0 mL, 0.01 moles) was then added dropwise over one minute, after which the mixture was allowed to return to ambient temperature and stirred for 18 h. The resulting mixture was gravity filtered and washed with water three times and brine one time. The organic layer was isolated and evaporated under reduced pressure, and filtered using a 0.45 μm syringe filter, giving the product PFPE_{E10}-dipropargyl carbonate (PFPE_{E10}-DPC) as a pale yellow, transparent liquid. (94 % yield) IR (neat): 2843 cm^{-1} (C-H), 1755 cm^{-1} (C=O), 1185 cm^{-1} (C-H), 1085 cm^{-1} (C-O). ^1H NMR ($(\text{CD}_3)_2\text{CO}$): 3.13ppm (d, 1H), 3.55-4.35ppm (m, 8H), 4.81ppm (d, 2H)

4.2.2.4 Physical characterization of PFPEs

The chemical structures of the functionalized PFPE products were confirmed using ^{19}F and ^1H nuclear magnetic resonance spectroscopy (NMR). Differential scanning calorimetry (DSC) thermograms were recorded using a TA Instruments DSC Q200 on samples which were prepared in air over the temperature range from -130 °C to 100 °C using a heat/cool/heat method at a heating and cooling rate of 10 °C and 5 °C/minute respectively. Thermogravimetric analysis (TGA) were run using a PerkinElmer Pyris 1 TGA apparatus under nitrogen and air from ambient to 600 °C with a heating rate of 20 °C/minute. Melting temperatures, glass transition temperatures, and crystallization temperatures (T_m , T_g , T_c 's respectively) were measured using DSC; the T_g was determined using the midpoint method on the second heating cycle

thermogram. The T_c and T_m were determined as the peak maximum and minimum of the cooling and heating cycle respectively. Fourier transform infrared spectroscopy (FTIR) was done using a Bruker ALPHA FTIR instrument under ambient conditions using an attenuated total reflectance (ATR) attachment (from 500 to 4000 cm^{-1} at resolution of 4 cm^{-1}). A TA Instruments ARES-G2 Rheometer, equipped with a cone plate (50 mm diameter; 0.0202 radian cone angle), was used to obtain all rheological measurements. Viscosity, η , was measured as a function of shear rate, which was ramped from 5×10^{-5} to 50 s^{-1} . All measurements were performed at 25 °C. The viscosity was determined using a Bingham analysis, which is used to describe viscoplastic materials (materials that behave as a rigid body at low stresses but flows as a viscous fluid at high stress).

4.2.3 Results and Discussion

Due to promising results obtained from physical blends of PFPE and PEG (discussed in Chapter 2), we ultimately became interested in pursuing PFPE derivatives that consist of both perfluoro-methylene or -ethylene and ethylene glycol functionalities. In particular, we began studying the commercially available product Fluorolink E10 (PFPE_{E10}-diol) (Figure 4.1), which presents short ethylene glycol chains covalently bound to the terminal ends of the PFPE backbone. The molar ratio of the perfluoroethylene (-CF₂CF₂O-), perfluoromethylene (-CF₂O-) and ethylene glycol (-CH₂CH₂O-) functionalities on Fluorolink E10 was determined using ¹⁹F and ¹H NMR using a similar procedure previously described in Chapter 3 and summarized in Table 4.1. It was therefore deduced that there are, on average, two ethylene glycol repeating units on each terminal end of PFPE_{E10}-diol.

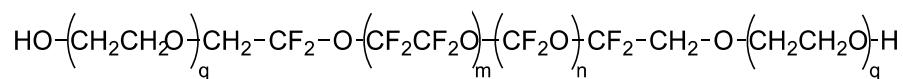


Figure 4.1 Chemical structure of PFPE_{E10}-diol

Table 4.1 Determination of m : n : q ratio and number of units for PFPE_{E10}-diol.

Monomer	Structure	Ratio
perfluoroethylene	-CF ₂ CF ₂ O-	6 (m = 6)
perfluoromethylene	-CF ₂ O-	4 (n = 4)
ethylene glycol	-CH ₂ CH ₂ O-	4 (q = 2)

It is important to differentiate the nomenclature between materials synthesized from Fluorolink E10 and Fluorolink D10. Fluorolink is referred to as PFPE_{E10}-diol while derivatives will be referred to as PFPE_{E10}-X (for example, PFPE_{E10}-dimethyl carbonate or PFPE_{E10}-DMC). On the other hand, Fluorolink D10 is simply be referred to as PFPE-diol and derivatives will be referred to as PFPE_{D10}-X (for example, PFPE-dimethyl carbonate or PFPE-DMC).

The synthesis of dimethyl carbonate-functionalized PFPEs from PFPE-diol was previously discussed in Chapter 3.¹⁰ Similar chloroformate chemistries were applied to PFPE_{E10}-diol in order to prepare PFPE_{E10}-DMC, PFPE_{E10}-diallyl carbonate (PFPE_{E10}-DAC), and PFPE_{E10}-dipropargly carbonate (PFPE_{E10}-DPC) (Figure 4.2). Systematic characterization of all four compounds (including PFPE_{E10}-diol) allows us to understand the effects of the PFPE terminal groups on physical and thermal properties. Comparison of these functionalized PFPE_{E10} compounds with previously studied PFPE-diol and PFPE-DMC will also elucidate the effects of the ethylene glycol chains on the material behavior. More importantly, it will allow us to understand the effects of electron density around the carbonate functional group on the interactions with lithium salts like LiTFSI. In small molecule alky-carbonate electrolytes, each Li-ion is typically solvated by the carbonyl oxygen of approximately 4 – 5 carbonate molecules

(2D rendition shown in Figure 4.3);^{11,12} The coordination strength between Li-ions and carbonate functional groups is therefore governed by the basicity of the carbonyl oxygen atoms. In turn, the electronegativity of the carbonate moieties is dependent on its neighboring functional groups. For example, the terminal methyl groups on PFPE_{E10}-DMC are electron donating by nature, and therefore increase electron density around the carbonate functional group. On the other hand, allyl-PFPE_{E10} and propargyl-PFPE_{E10} are relatively more electron withdrawing, and therefore draw electron density away from the carbonate moiety. Therefore the Lewis basicity of the carbonate group should be PFPE_{E10}-DMC > allyl-PFPE_{E10}, > propargyl-PFPE_{E10} and coordination affinity with Li-ions should increase with increasing basicity.

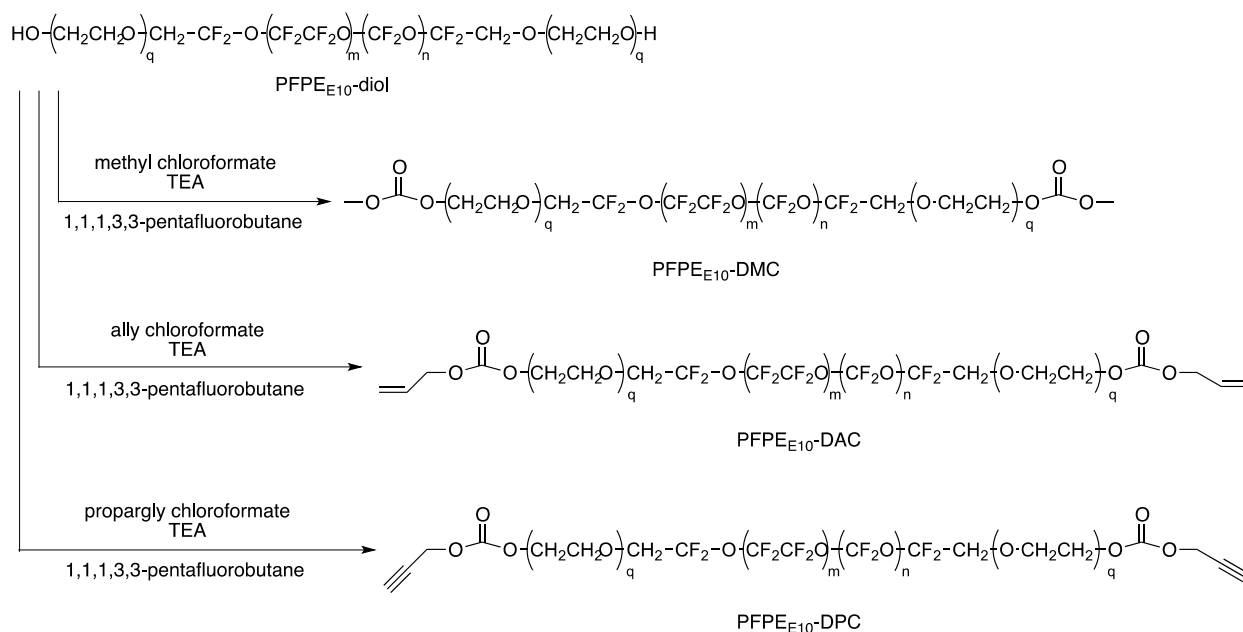


Figure 4.2 Synthetic scheme of PFPE_{E10}-diol to prepare PFPE_{E10}-DMC, PFPE_{E10}-DAC and PFPE_{E10}-DPC.

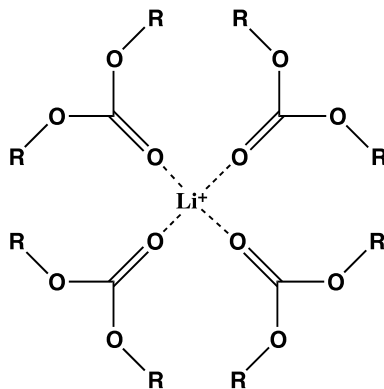


Figure 4.3 Li-ions are solvated by carbonyl oxygen atoms of carbonate molecules.

The thermal properties of PFPE_{E10}-diol and its dicarbonate derivatives were characterized using TGA and DSC. The resulting TGA curves are shown in Figure 4.4; the degradation temperatures as well as the glass transition temperatures are also tabulated in Table 4.2. The observed T_g of PFPE_{E10}-diol and PFPE_{E10}-DMC are comparable to that of PFPE-diol and PFPE-DMC respectively (-92 vs. -89 °C and -91 vs. -95 °C respectively).¹⁰ Similar to the PFPE D10 systems, the E10 materials were completely amorphous, suggesting that the addition of ethylene glycol chains on the PFPE backbone did not result in bulk semi-crystalline characteristics. On the other hand, PFPE_{E10}-diol and its derivatives demonstrated lower degradation temperatures (T_d 's) relative to their PFPE_{D10} analogs. While the degradation temperature at 5 weight (wt.) % loss ranged from 210 to 212 °C for PFPE_{D10}-diol and PFPE_{D10}-DMC,¹⁰ PFPE_{E10}-diol, PFPE_{E10}-DMC, PFPE_{E10}-DAC, and PFPE_{E10}-DPC exhibit degradation temperatures from 180 to 204 °C. Regardless, however, these materials are significantly more thermally stable than traditional alkyl carbonate solvents used in commercial Li-ion batteries.¹³ Use of these PFPE_{E10} materials as an alternative to low molecular weight alkyl carbonates would therefore still impart a drastic improvement in battery safety.

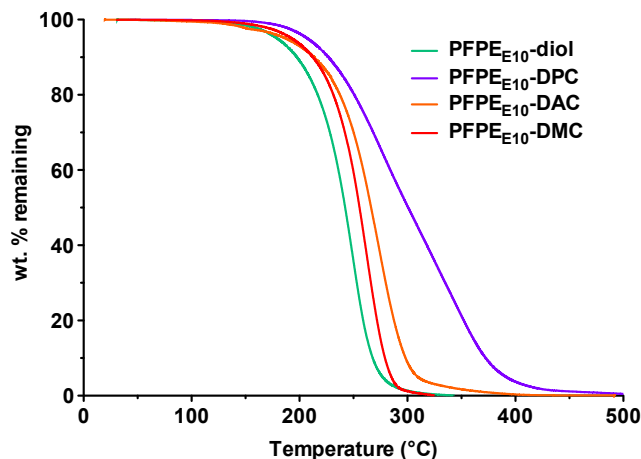


Figure 4.4 Thermogravimetric curves for thermal decomposition of PFPE_{E10}-diol and its derivatives obtained in N₂.

Table 4.2 Thermal properties of PFPE_{E10}-diol and synthesized dicarbonate derivatives

PFPE Sample	PFPE _{E10} -diol	PFPE _{E10} -DPC	PFPE _{E10} -DAC	PFPE _{E10} -DMC
T_d (5%) (°C)	180	204	187	194
T_g (°C)	-92	-85	-91	-91

The solubility of LiTFSI in these materials was also investigated. As expected, PFPE E10 materials demonstrate higher maximum salt loading compared to PFPE D10 materials (Figure 4.5). This increase is likely due to the contribution originating from the ethylene glycol functionality present in PFPE_{E10} systems; the ability for ethylene glycols and poly(ethylene oxide) (PEO) to dissolve large amounts of LiTFSI is commonly recognized.^{14,15} Interestingly, PFPE_{E10}-DMC, PFPE_{E10}-DAC, and PFPE_{E10}-DPC all demonstrate lower maximum LiTFSI concentrations relative to PFPE_{E10}-diol. This is a different trend than the PFPE D10 series, where PFPE-DMC exhibits higher LiTFSI solubility relative to PFPE-diols. This suggests that end group functionality may have different effects in the PFPE_{D10} and PFPE_{E10} systems and that incorporation of carbonate moieties may not necessarily contribute additively to the overall LiTFSI solubility. In fact, addition of the carbonate moiety to PFPE_{E10} may in turn interfere with

ethylene glycol/LiTFSI interactions, ultimately lowering the amount of lithium salt capable of interacting with ethylene glycol groups.

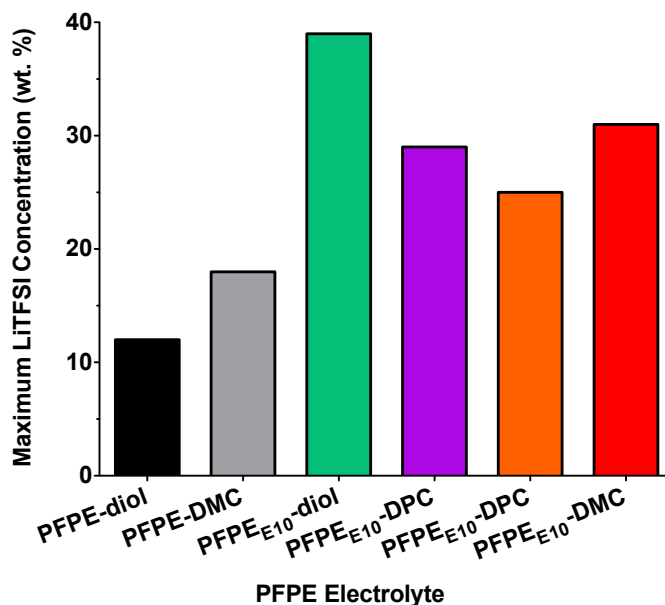


Figure 4.5 Maximum solubility of LiTFSI in different PFPE electrolytes.

Due to the fact that the wettability and flow of electrolytes are important considerations in battery assembly,¹⁶ the viscosities of these materials, with and without LiTFSI were determined (Figure 4.6). Viscosity was measured as a function of shear rate and subsequently modeled using Bingham analysis, a commonly used method to describe viscoplastic materials that exhibit a nonzero shear stress at zero shear rate.¹⁷ As expected, viscosity of the materials increases with increasing LiTFSI concentration. This behavior is observed in all PFPE materials, and indicates an increase in the degree of ionic interaction as the salt concentration is raised,¹⁸ impacting the flow behavior. It is clear that PFPE E10 materials exhibit higher viscosities than PFPE D10 materials; this confirms the contribution of the ethylene glycol functional groups to the ionic interactions with lithium salt. Interestingly, it is also observed that the degree of ionic interaction is affected by end group functionality as well. Although PFPE_{E10}-DMC, PFPE_{E10}-

DAC, and PFPE_{E10}-DPC exhibit similar viscosities in the absence of salt, the rate of increase in viscosity as a function of salt concentration is the highest in PFPE_{E10}-DMC, followed by PFPE_{E10}-DAC, then PFPE_{E10}-DPC. This is consistent with the trend of decreasing electron density surrounding the carbonate group due to the electron withdrawing nature of the allyl and propargyl moieties relative to the methyl functional group. This suggests that the nucleophilicity of the carbonate group on the synthesized PFPE_{E10}-diol derivatives significantly impacts the strength of LiTFSI interactions.

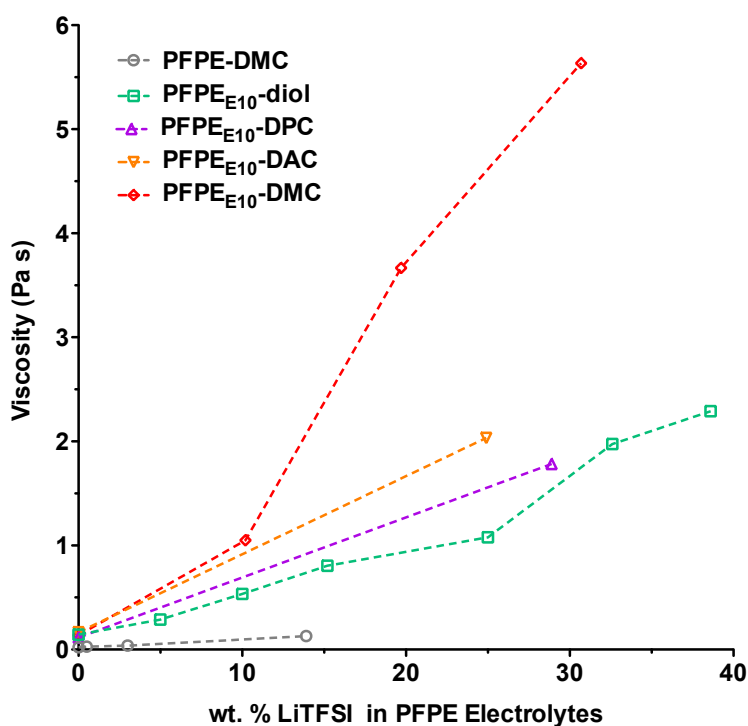


Figure 4.6 Viscosity as a function of salt concentration in PFPE electrolytes.

To further elucidate the interactions between LiTFSI and different functional groups placed on PFPEs, DSC and FTIR spectroscopy were employed. DSC was used to study the effects of LiTFSI salt concentration on the materials' T_g 's. Figure 4.7 presents the T_g of PFPE E10 electrolytes as a function of LiTFSI concentration. As shown in this figure it is clear that the ionic interactions between LiTFSI and PFPE polymer significantly affects the glass transition

temperature as well. At the maximum salt concentration for all of the E10 oligomers, the glass transition temperature is approximately 20 °C higher relative than 0 wt. % of LiTFSI, confirming the presence of coordination between PFPE chains with Li-ions to form ionic crosslinks that limit the mobility of PFPE chains and therefore result in a higher T_g .^{19,20}

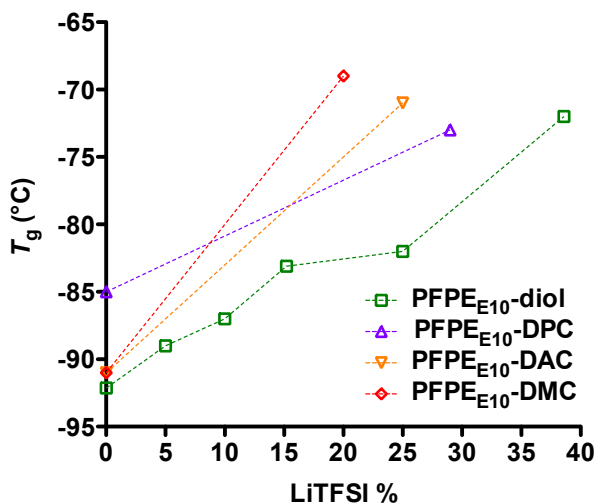


Figure 4.7 T_g as a function of salt concentration in PFPE_{E10}-diol and its derivatives.

FTIR spectroscopy was also used to probe the effects of LiTFSI on the different functional groups on PFPEs. Figure 4.8 illustrates the FTIR spectra of PFPE_{E10}-DPC with saturated LiTFSI (29 wt.%) compared to pure PFPE_{E10}-DPC; the signals originating from the carbonyl stretch, $\text{-C}\equiv\text{C-H}$ stretch and bend are highlight in approximately 1755 cm^{-1} , 3300 cm^{-1} , and 790 cm^{-1} respectively. As shown in the figure, all three signals present a shift upon addition of LiTFSI, suggesting that both the terminal and carbonate group play a role in LiTFSI interactions in the PFPE electrolyte. However, it appears that the carbonyl C=O signal experiences the greatest shift in wavenumber, from 1736 to 1755 cm^{-1} , suggesting that the carbonate functional group interacts with LiTFSI to a greater extent relative to the propargyl moiety. This experiment is currently being repeated with PFPE_{E10}-diol, PFPE_{E10}-DMC, and PFPE_{E10}-DAC.

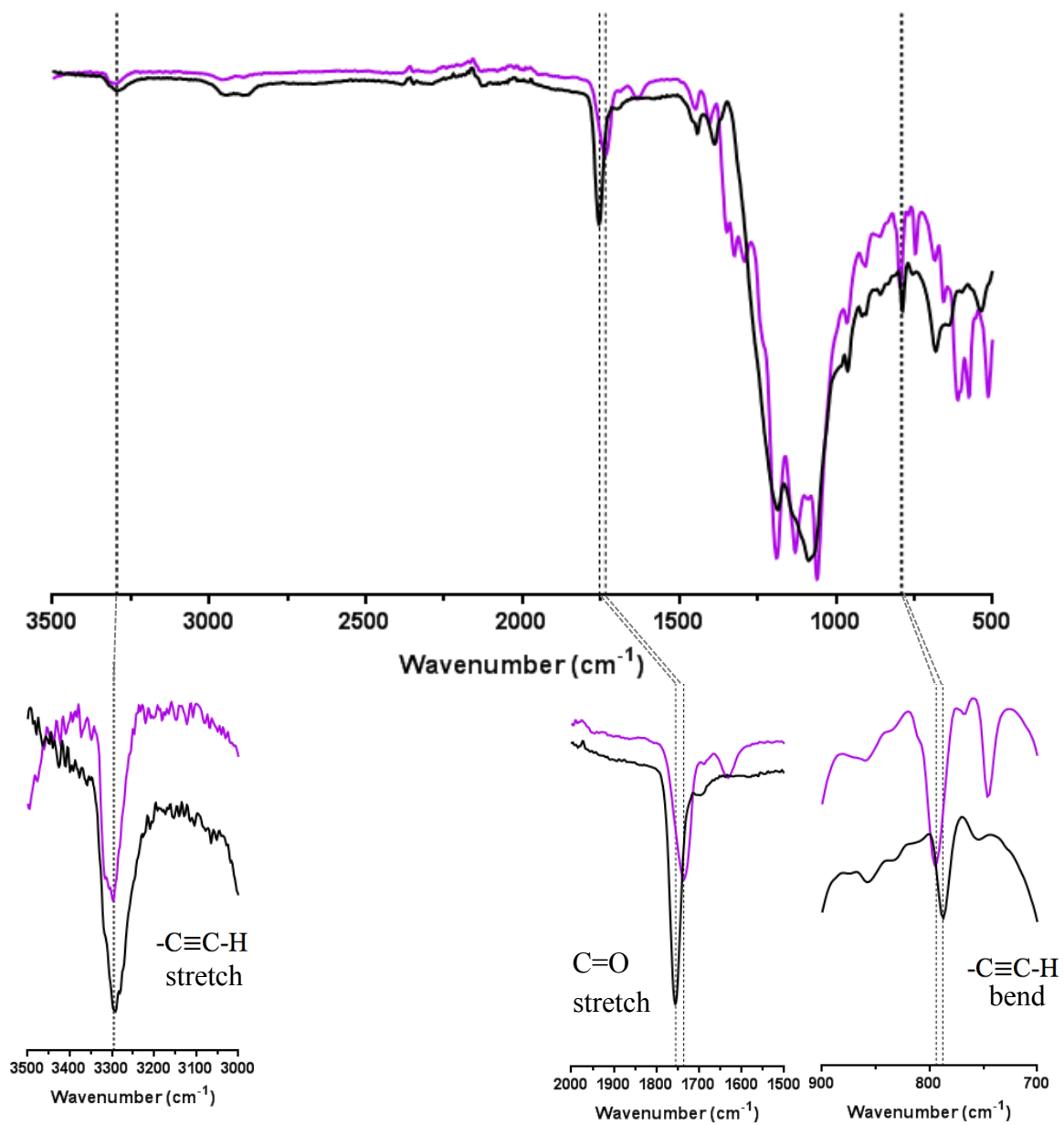


Figure 4.8 FTIR spectra of PFPE_{E10}-DPC with 29 wt. % LiTFSI (purple) relative to pure PFPE_{E10}-DPC (black).

We have demonstrated the importance of end group design on the overall thermal and physical properties of PFPEs. Clearly, incorporation of targeted electron withdrawing and donating groups can be used to manipulate polymer-LiTFSI interactions in order to optimize these interactions for Li-ion battery performance. We are currently continuing to pursue a thorough understanding of the effect of incorporating different functional groups by determining the extent of ionic interactions in PFPE_{E10}-diol, PFPE_{E10}-DAC and PFPE_{E10}-DPC as well. Furthermore, investigation on the effects of these functional groups on the ionic conductivities of these materials is currently underway.

4.3 Part B: Translation to Ultraviolet-Curable PFPE Electrolytes

Modifications of terminal hydroxyl groups on PFPEs to alkene functional groups ultimately led to the development of solid PFPE films or elastomers,^{21,22} evolving into an investigation focused on translating PFPE electrolyte technology towards solid polymer electrolytes (SPEs). SPEs offer many advantages over liquid electrolytes, including eliminated risk of electrolyte leakage, ease of battery cell processing, and ability to mechanically prevent lithium dendrite formation. The mechanical flexibility of SPEs has also garnered interest with regards to its incorporation into batteries for flexible and wearable electronic device applications.

Currently, PEO is the most commonly studied homopolymer SPE due to its ability to dissolve high levels of lithium salts.²³ Unfortunately because ionic conductivity is strongly believed to occur dominantly in the electrolyte's amorphous phase, the crystallinity of PEO limits practical ionic conductivity ($\sim 10^{-4}$ S/cm) except at temperatures above its T_m , which is typically around 60 - 80 °C. Although strategies used to mitigate crystallinity span from the use of nanoparticle fillers such as aluminum oxide (Al₂O₃), titanium oxide (TiO₂), and silicon oxide (SiO₂)^{24,25} to novel macromolecular architectures such as stars,^{26,27} combs,¹⁹ and dendrimers,^{28,29}

there is still a need for more exploration in this area in order to successfully improve the conductivity and efficiency of these materials.

Herein we report the development of solid PFPE conductive elastomers prepared using ultraviolet (UV)-irradiated free radical photo-polymerization of dimethacrylate-functionalized PFPEs containing dissolved LiTFSI. The UV photocuring technique is a rapid solventless method that maintains the integrity of LiTFSI salt and is highly desirable compared to alternative methods which are time consuming, require costly solvents and solvent removal processes and lead to degradation of the lithium salts during the processing steps. Although use of UV curable elastomers for Li-ion batteries have previously been reported in literature,³⁰⁻³³ the development of PFPE-based solids and gels for this application is unprecedented. Furthermore, dithiol-terminated PFPEs were also synthesized as an additive to tune elastomeric flexibility and mechanical integrity.

4.3.1 Materials

2-Isocyanatoethyl methacrylate (IEM), Dibutyltin diacetate (DBTDA), α -hydroxycyclohexylphenyl ketone (HCPK), LiTFSI, TEA, anhydrous methanol, p-toluensulfonyl chloride, cystamine dihydrochloride, and dithiothreitol were purchased commercially from Sigma Aldrich and used as received. 1,1,1,3,3-pentafluorobutane (from MicroCare Corporation) and dimethyl sulfoxide (DMSO) (from Fisher Scientific) solvents were reagent grade and used directly. Fluorolink D10 (PFPE-diol) was purchased from Santa Cruz Biotechnology and Solvay Solexis.

4.3.2 Experimental

4.3.2.1 Synthesis of PFPE-Dimethacrylate

The synthesis of α,ω -dimethacrylate-functionalized PFPEs (PFPE-dimethacrylate, PFPE-DMA) has been reported previously.²² In brief, Fluorolink D10 (20 g, 0.02 moles) was dissolved in 1,1,1,3,3-pentafluorobutane (100 mL) with magnetic stirring and allowed to react with IEM (6.0 mL, 0.04 moles) and 0.1 wt% DBTDA, as a catalyst, at 45 °C for at least 12 h. The solutions was then allowed to cooled to ambient temperatures and gravity filtered through a column of alumina adsorption powder and the solvent was removed by roto-evaporation to yield a clear colorless viscous liquid (reaction scheme shown in Figure 4.9).

4.3.2.2 Synthesis of PFPE-Dithiol

Fluorolink D10 (5 g, 5×10^{-3} moles) and TEA (1.9 mL, 0.0136 moles) were dissolved into 1,1,1,3,3-pentafluorobutane (250 mL) with magnetic stirring and the solution was added drop wise to a solution of p-toluensulfonyl chloride (2.6 g, 0.0136 moles) in DMSO (approximately 20 mL) over 4 to 5 h at room temperature under N₂. The solution was stirred with a magnetic stirrer for at least 18 hours. The solution was subsequently added drop wise over 4 to 5 h to a solution of cystamine dihydrochloride (4.5 g, 0.04 moles) and TEA (5.6 mL, 0.04 moles) in DMSO (approximately 20 mL) and stirred for an additional 18 h. The product was washed with water, the solvent was removed by roto-evaporator, and the product was re-dissolved in 1,1,1,3,3-pentafluorobutane (approximately 100 mL). Dithiothreitol (6.1 g, 0.04 moles) dissolved in DMSO (approximately 20 mL) was added and the solution was heated with magnetic stirring at 50°C for 12 hours. The product was washed with water and isolated through roto-evaporation. Free thiols were confirmed using Ellman's Test. Ellman's solution was prepared using 5,5'-Dithiobis-(2-Nitrobenzoic Acid) and pH 8.0 buffer. The solution turned

translucent yellow after a few drops of PFPE-dithiol product were added to approximately 10 mL of Ellman's solution and vortexed. The reaction scheme is shown in Figure 4.10. (~60 % yield)
IR (neat): 3360 cm^{-1} (N-H), 2956 cm^{-1} (S-H), 1715 cm^{-1} (C-O). $^1\text{H NMR}$ ($(\text{CD}_3)_2\text{CO}$): 3.92 – 3.93 ppm (m, 2H), 2.73 – 2.76 (m, 4H)

4.3.2.3 Photocuring of PFPE Precursors

0.2 wt. % of HPCCK photo-initiator was added to PFPE-DMA and 0 to 40 wt. % of PFPE-dithiol to create a clear colorless mixture. The solution was then pipetted into a Teflon mold, degassed under vacuum, and heated to 45 °C for at least 25 minutes. The mold was transferred to a UV curing chamber (Electronlite UV curing chamber model no. 81432-ELC-500, $\lambda = 365$ nm) and exposed to UV irradiation under nitrogen purge for 20 min.

For ionic conductivity studies, 0.2 wt. % of HPCCK photo-initiator was added to solutions of PFPE-DMA, 0 to 40 wt. % of PFPE-dithiol, and 10 wt. % LiTFSI. Solutions were subsequently spread onto silicon wafers using a 100 μm doctor blade inside a glove box and irradiated for at least 25 minutes. Films were hand pressed into circular pellets of approximately 15 mm in diameter. The sample was placed between two mirror-polished stainless steel electrodes and vacuum sealed together in a non-conducting pouch. The cells were subsequently tested for ionic conductivity using AC impedance, following a procedure previously described in Chapter 2.

4.3.2.4 Characterization of Crosslinked PFPEs

Soluble (sol) fractions of the PFPE elastomers were measured using a Soxlet Extractor with refluxing 1,1,1,3,3-pentafluorobutane for at least 12 h. The initial weights of the films (W_0) and the weight of the dried films recovered from Soxlet Extractor (W) were used to calculate the sol fraction using the equation:³⁴

$$\text{sol fraction (\%)} = W_0 - W/W_0 \times 100 \dots \text{equation 4.1}$$

The gel fraction is then calculated as:

$$\text{gel fraction (\%)} = 100 - \text{sol fraction} \dots \text{equation 4.2}$$

Stress-strain measurements were performed using dogbone-shaped samples (10 mm x 4 mm x 2 mm) at ambient conditions on an Instron model 5566 system using a 500 N load cell at a crosshead speed of 5 mm/min. From the stress-strain curves, the Young's modulus, E , was calculated using the Instron Bluehill software. At least four replicates were performed for each sample.

4.3.3 Results and Discussion

Our methodology allows for the potential to prepare a series of photochemically cured PFPE-based conductive elastomeric networks where the modulus is tunable. This is desirable because of the wide spectrum of applications in which Li-ion batteries can be used. Electrolytes with a high modulus are desirable in high performance batteries composed of lithium metal as an electrode because the electrolyte's mechanical integrity physically suppresses dendrite growth and penetration through the cell. On the other hand, flexible and conformable electrolytes are ideal for wearable and bendable electronics, where good contact between the electrolyte and electrode needs to be maintained even under mechanical stress to facilitate electrochemical reactions at the interface.³⁵ Therefore our strategy was to prepare a class of PFPE solid and gel polymer electrolytes where modulus and flexibility can be tuned simply by modifying ratios of curable PFPEs.

Our group has previously optimized the synthesis of functionalized PFPEs which can subsequently be utilized in a UV-curing crosslinking process.⁴ Using this protocol, PFPE-DMA was prepared in a catalyzed reaction with PFPE-diol and IEM (Figure 4.9).

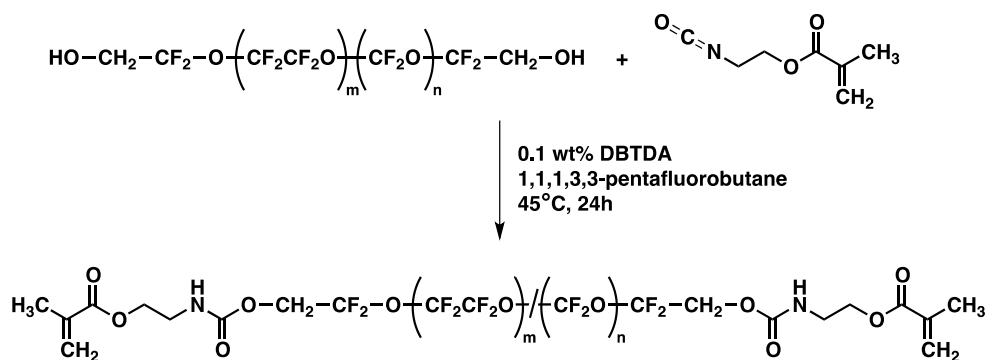


Figure 4.9 Schematic of the synthesis of PFPE-DMA.

Additionally, we developed a synthesis for thiol-terminated PFPEs involving PFPE-diol, 4-toluenesulfonyl chloride, cysteamine dihydrochloride, and dithiothreitol (Figure 4.10). The incorporation of PFPE-dithiol as an additive in the UV-curing process enables UV-facilitated thiol-ene “click” chemistry to also occur. In other words, in addition to photo-polymerization or crosslinking of PFPE-DMA (where PFPE-DMA reacts with itself), hydrothiolation between PFPE-DMA and PFPE-dithiol is simultaneously taking place (Figure 4.11). Because thiol reacts orthogonally and exclusively in a 1:1 molar ratio with C=C bonds in typical thiol-ene “click” chemistry, propagating radical PFPE-DMA chains are effectively scavenged by PFPE-dithiol chains, leading to the chain extension of PFPE-chains. This results in a distribution of larger molecular weight chains between crosslinks (M_c) throughout the crosslinked network as a function of the amount of dithiol modified PFPE that is incorporated.

Using the photocuring process, crosslinked PFPE elastomers were synthesized using 0 wt. %, 10 wt. %, 20 wt. %, 30 wt. %, and 40 wt. % PFPE-dithiol. Elastomers with wt. % of PFPE-dithiol beyond 40 wt. % were not prepared because it was expected that elastomers with a majority wt. % of PFPE-dithiol would not successfully crosslink or produce elastomers with adequate mechanical integrity to be of use. If thiol-ene “click” reactions dominate the curing process, it was expected that the solution would not reach gel point since the functionality of both PFPE-DMA and PFPE-dithiol in hydrothiolation would be 2. Indeed, this was further demonstrated through sol-gel fraction analysis of these elastomers (Figure 4.12). The gel fraction, the percentage of monomers that is a part of the infinite crosslinked PFPE network,³⁶ was calculated for PFPE elastomers composed of 0 to 40 wt. % of PFPE-dithiol by comparing the mass of the elastomers prior and after the Soxhlet extraction; at 40 wt. % of PFPE-dithiol in the PFPE elastomer, the gel fraction was observed to be only 55 %; elastomers made with this high wt. % of PFPE-dithiol are more sticky and gel-like as opposed to dry rigid solids. Clearly, the addition and amount of the PFPE-dithiol has significant effects on the gel fraction of the overall material where both solid and gel type PFPE elastomers could be prepared simply by varying the weight ratios.

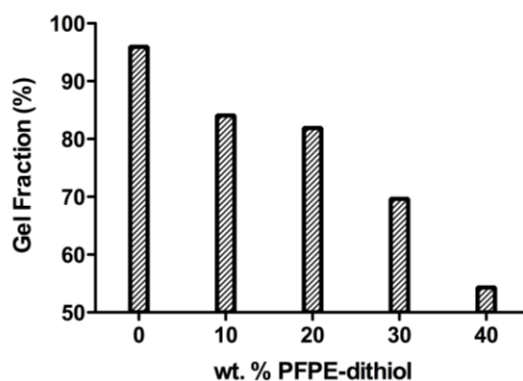


Figure 4.12 Gel fraction of PFPE-DMA elastomers with various wt. % of PFPE-dithiol

The mechanical properties of these PFPE elastomers were characterized by tensile tests. The calculated Young's moduli as well as the resulting stress-strain curves are shown in Figure 4.14 and Figure 4.13 respectively. As shown in Figure 4.13, the Young's modulus, E , decreased by almost tenfold when 40 wt. % of PFPE-dithiol, indicating that increasing the M_c throughout the network and reduction of the gel fraction plays a significant role in enhancing the softness of the elastomer. However, it is noted that as the ratio of PFPE-dithiol increases, the material becomes less crosslinked and loses mechanical integrity. This is shown in Figure 4.14, where the stress-strain curves suggest that elastomers with 20 or 30 wt. % of PFPE-dithiol are able to withstand more load and be elongated to a greater degree before breaking. Because the modulus is related to the crosslink density, ν_E , through the equation:³⁷

$$E = 3\nu_E RT \dots \dots \dots \text{equation 4.3}$$

where R and T are the ideal gas constant and temperature respectively, the lowered modulus as a result of addition of PFPE-dithiol suggest that incorporation of PFPE-dithiol does indeed effectively lower the crosslink density of the material. This confirms that the modulus can be tunable based on simply modifying the ratio of PFPE-DMA and PFPE-dithiol.

Figure 4.15 also demonstrates that addition of PFPE-dithiol enhances the flexibility of PFPE elastomers. PFPE elastomers cured in the absence of PFPE-dithiol are rigid and cannot be bent significantly before snapping. In contrast, PFPE elastomers composed of PFPE-dithiol are relatively more flexible.

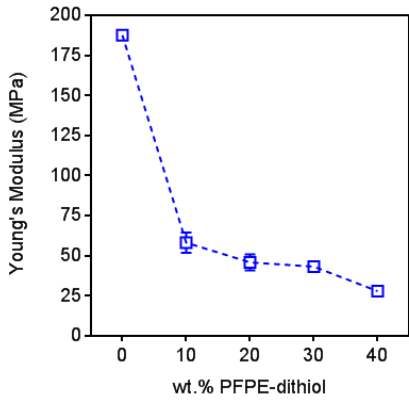


Figure 4.13 Young's Modulus of PFPE elastomers with various wt. % of PFPE-dithiol.

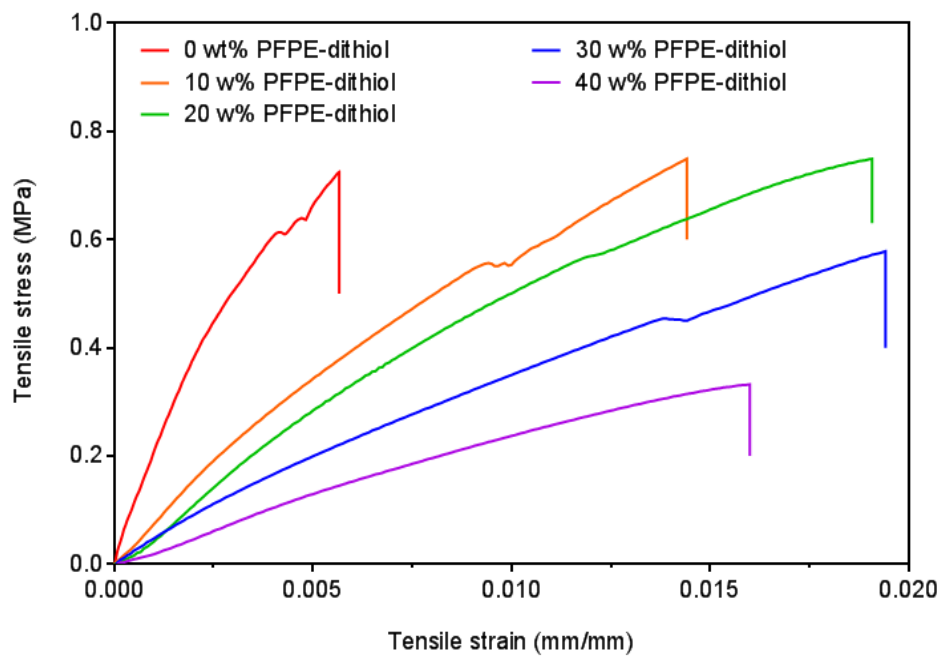


Figure 4.14 Stress strain curves for PFPE-DMA elastomers with various wt. % of PFPE-dithiol

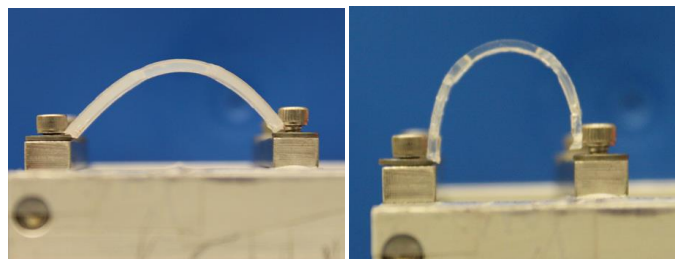


Figure 4.15 The flexibility of (left) a PFPE-DMA elastomer compared to that of a PFPE-DMA with 20% PFPE-dithiol elastomer (right).

The ionic conductivity of PFPE elastomers was characterized using impedance spectroscopy. 10 wt.% of LiTFSI was added to the pre-cure solution of PFPE-DMA and PFPE-dithiol and the films were subsequently tested for ionic conductivity at temperatures from 20 to 120 °C. At some lower temperatures, especially with the case of PFPE-DMA with 0 wt.% PFPE-dithiol, the measured resistance from impedance spectroscopy was too high and therefore could not be accurately used to calculate a conductivity value confidently. The addition of PFPE-dithiol, however, increases the ionic conductivity by at least an order of magnitude. This is expected since a decrease in crosslink density has been shown to increase segmental motions of polymer chains between crosslinks, which should enhance Li-ion transport and increase ionic conductivity. Clearly, the presence of PFPE-dithiol in the pre-cure solution has significant effects on the polymeric crosslinked structure and network, which, in turn, changes the materials' properties related to crosslink density and molecular weight between crosslinks such as ionic conductivity. However, the highest conductivity achieved by these elastomers is on the order of 10^{-8} S/cm at 120 °C, which falls below the practical level of ionic conductivity required for commercial batteries. Further optimization and understanding of these materials is therefore needed to improve the electrochemical properties for battery applications.

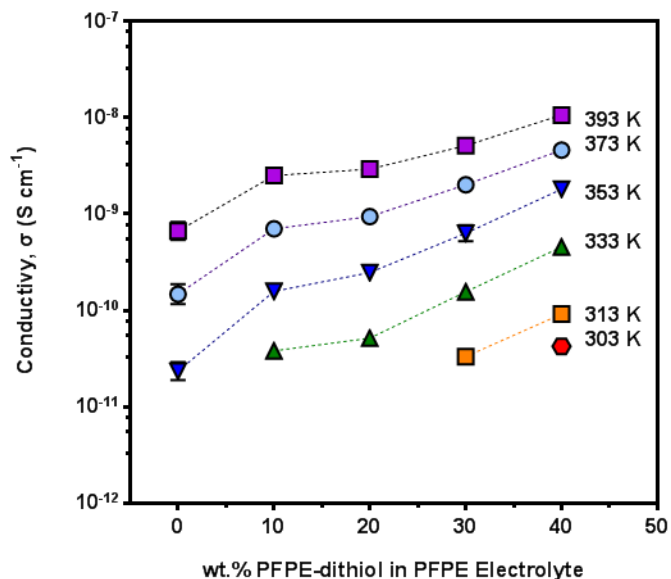


Figure 4.16 Arrhenius plots of temperature-dependent ionic conductivity of PFPE-DMA elastomers with various wt. % of PFPE-dithiol.

In this work, we report the successful fabrication of elastomers from PFPE-DMA and PFPE-dithiol that demonstrate tunable modulus, softness, and bendability. We found that increasing the amount of PFPE-dithiol in the pre-UV curing solution lowers the Young's modulus, as well as increases flexibility and ionic conductivity. Ongoing studies include extensive thermal analysis to determine the T_g and T_g (5%) of these materials using DSC and TGA as well as investigations on the segmental relaxations and elastic modulus of these elastomers using dynamic mechanical analysis. We expect to apply understanding of the relationship between PFPE segmental relaxations and ionic conductivity towards the development of next generation of conductive elastomers with improved physical and electrochemical properties.

REFERENCES

- (1) Tan, S.; Ji, Y. J.; Zhang, Z. R.; Yang, Y. *Chemphyschem* **2014**, *15*, 1956.
- (2) Freunberger, S. A.; Chen, Y.; Drewett, N. E.; Hardwick, L. J.; Barde, F.; Bruce, P. G. *Angew Chem Int Ed Engl* **2011**, *50*, 8609.
- (3) Abraham, K. M.; Goldman, J. L.; Natwig, D. L. *Journal of The Electrochemical Society* **1982**, *129*, 2404.
- (4) Ong, S. P.; Ceder, G. *Electrochimica Acta* **2010**, *55*, 3804.
- (5) Jo, G.; Ahn, H.; Park, M. J. *ACS Macro Letters* **2013**, *2*, 990.
- (6) Wang, X. J.; Lee, H. S.; Li, H.; Yang, X. Q.; Huang, X. J. *Electrochemistry Communications* **2010**, *12*, 386.
- (7) Smart, M. C.; Ratnakumar, B. V.; Ryan-Mowrey, V. S.; Surampudi, S.; Prakash, G. K. S.; Hu, J.; Cheung, I. *Journal of Power Sources* **2003**, *119-121*, 359.
- (8) Laroire, C.; Mukerjee, S.; Plichta, E. J.; Hendrickson, M. A.; Abraham, K. *Journal of The Electrochemical Society* **2011**, *158*, A302.
- (9) Hassoun, J.; Croce, F.; Armand, M.; Scrosati, B. *Angewandte Chemie International Edition* **2011**, *50*, 2999.
- (10) Wong, D. H. C.; Thelen, J. L.; Fu, Y.; Devaux, D.; Pandya, A. A.; Battaglia, V. S.; Balsara, N. P.; Desimone, J. M. *Proc Natl Acad Sci U S A* **2014**, *111*, 3327.
- (11) Mandai, T.; Yoshida, K.; Ueno, K.; Dokko, K.; Watanabe, M. *Phys Chem Chem Phys* **2014**, *16*, 8761.
- (12) Kameda, Y.; Umebayashi, Y.; Takeuchi, M.; Wahab, M. A.; Fukuda, S.; Ishiguro, S.-i.; Sasaki, M.; Amo, Y.; T. Usuki *J. Phys. Chem. B* **2007**, *111*, 6104.
- (13) Mikolajczak, C.; Kahn, M.; White, K.; Long, R. T. *Lithium-Ion Batteries Hazard and Use Assessment* The Fire Protection Research Foundation 2011.
- (14) Lightfoot, P.; Mehta, M. A.; Bruce, P. G. *Science* **1993**, *262*, 883.
- (15) Ito, Y.; Kanehori, K.; Miyauchi, K.; Kudo, T. *Journal of Materials Science* **1987**, *22*, 1845.
- (16) Zhang, S. S. *Journal of Power Sources* **2006**, *162*, 1379.
- (17) Bingham, E. C. *U.S. Bureau of Standards Bulletin* **1916**, *13*, 309.

- (18) Southall, J. P.; Hubbard, H. V. S. A.; Johnston, S. F.; Rogers, V.; Davies, G. R.; McIntyre, J. E.; Ward, I. M. *Solid State Ionics* **1996**, *85*, 51.
- (19) Sun, J.; Stone, G. M.; Balsara, N. P.; Zuckermann, R. N. *Macromolecules* **2012**, *45*, 5151.
- (20) Wong, D. H. C.; Vitale, A.; Devaux, D.; Taylor, A.; Pandya, A. A.; Hallinan, D. T.; Thelen, J. L.; Mecham, S. J.; Lux, S. F.; Lapidés, A. M.; Resnick, P. R.; Meyer, T. J.; Kostecki, R. M.; Balsara, N. P.; DeSimone, J. M. *Chemistry of Materials* **2014** *in press*
- (21) Kim, J.; Rolland, J. P.; Carbonell, R. G.; DeSimone, J. M. *Chemistry of Materials* **2010**, *22*, 2411.
- (22) Rolland, J. P.; Van Dam, R. M.; Schorzman, D. A.; Quake, S. R.; DeSimone, J. M.; *Journal of the American Chemical Society* **2004**, *126*, 2322.
- (23) Fergus, J. W. *Journal of Power Sources* **2010**, *195*, 4554.
- (24) Croce, F.; Appetecchi, G. B.; Persi, L.; Scrosati, B. *Nature* **1998**, *394*, 456.
- (25) Tarascon, J. M.; Armand, M. *Nature* **2001**, *414*, 359.
- (26) Niitani, T.; Amaike, M.; Nakano, H.; Dokko, K.; Kanamura, K. *Journal of The Electrochemical Society* **2009**, *156*, A577.
- (27) Nishimoto, A.; Watanabe, M.; Ikeda, Y.; Kohjiya, S. *Electrochimica Acta* **1998**, *43*, 1177.
- (28) Hawker, C. J.; Chu, F.; Pomery, P. J.; Hill, D. J. T. *Macromolecules* **1996**, *29*, 3831.
- (29) Watanabe, M.; Hirakimoto, T.; Mutoh, S.; Nishimoto, A. *Solid State Ionics* **2002**, *148*, 399.
- (30) Nair, J. R.; Gerbaldi, C.; Destro, M.; Bongiovanni, R.; Penazzi, N. *Reactive & Functional Polymers* **2011**, *71*, 409.
- (31) Nair, J. R.; Gerbaldi, C.; Meligrana, G.; Bongiovanni, R.; Bodoardo, S.; Penazzi, N.; Reale, P.; Gentili, V. *Journal of Power Sources* **2008**, *178*, 751.
- (32) Ha, H.-J.; Kil, E.-H.; Kwon, Y. H.; Kim, J. Y.; Lee, C. K.; Lee, S.-Y. *Energy & Environmental Science* **2012**, *5*, 6491.
- (33) Kim, C.-S.; Kim, B.-H.; Kim, K. *Journal of Power Sources* **1999**, *84*, 12.
- (34) Hassan, M. M.; Aly, R. O.; Aal, S. E. A.; El-Masry, A. M.; Fath, E. S. *Journal of Industrial and Engineering Chemistry* **2013**, *19*, 1722.

(35) Kil, E. H.; Choi, K. H.; Ha, H. J.; Xu, S.; Rogers, J. A.; Kim, M. R.; Lee, Y. G.; Kim, K. M.; Cho, K. Y.; Lee, S. Y. *Adv Mater* **2013**, *25*, 1395.

(36) Odian, G. *Principles of Polymerization 4th edition*; John Wiley & Sons: New Jersey, 2004.

(37) Sekkar, V. *Journal of Applied Polymer Science* **2010**, *117*, 920.

CHAPTER 5

ONGOING AND FUTURE DIRECTIONS

5.1 Introduction

The promising features and properties of perfluoropolyethers (PFPEs) towards lithium-ion (Li-ion) battery applications opens doors for new research ideas that pursue a more thorough understanding of the electrochemical behavior of these materials in order to capitalize on their use. To date, the determination of ion transport mechanisms of lithium salts in PFPEs, as well as the investigation of interfacial PFPE reduction and oxidation chemistry, are unexplored yet important areas that should be considered. Herein, ongoing and future possible directions for this research program are discussed: early results on the use of pulsed-field gradient nuclear magnetic resonance spectroscopy (pfg-NMR) to study Li-ion dynamics in PFPEs are described, followed by a discussion focusing on potential formulation and characterization strategies that can be used to study the PFPE/electrode interface.

5.2 NMR as a Tool to Study Ion Transport in Electrolytes

The ability to synthetically design novel high performance polymeric electrolytes would be limited without a thorough understanding of ion-polymer interactions and ion transport properties. The relationship between electrolyte structure and composition and parameters such as ionic conductivity (σ), diffusion (D), and Li-ion transference numbers (t^+ 's) is therefore an essential consideration.^{1,2} The determination of these properties through electrochemical techniques like alternating current (AC) impedance spectroscopy and electromotive force method are frequently discussed in the literature.¹

In addition, NMR is also commonly used to study ion dynamics and transport in Li-ion electrolytes. It is a powerful non-invasive method that elucidates mesoscale dynamic processes from spin-lattice relaxation to ion mobility.³ In particular, pfg- NMR is especially useful in studying motion related to long-range ionic transport⁴ since this technique can investigate the diffusion of NMR-active nuclei separately. Self-diffusion coefficients (D), and transference numbers of cations, anions or counterions, and polymers can therefore be measured using pfg-NMR by focusing on nuclei such as ^7Li , ^{19}F , ^1H , and ^{13}C .^{3,4}

5.2.1 Using pfg-NMR to Measure t^+ 's in PFPE Electrolytes

We have previously used electrochemical potentiostatic polarization techniques to measure t^+ 's and reported that Li-ion t^+ 's in PFPE-dimethyl carbonate (PFPE-DMC) electrolytes are close to unity (Chapter 3).⁵ Encouraged by these results, we became interested in other methodologies in order to expand our understanding of Li-ion transport in PFPEs and started employing pfg-NMR to study liquid PFPE-diol and PFPE-DMC electrolytes containing bis(trifluoromethane)sulfonimide lithium salt (LiTFSI) (chemical structures can be found in Chapters 2 and 3). The remainder of this section (5.2.1) describes the application of stimulated-echo pulse sequences with bipolar gradients (a specific pfg-NMR pulse sequence) to measured preliminary diffusion data for Li-ions using ^7Li NMR at various temperatures. The effects of temperature and PFPE terminal group on ion diffusion mechanisms in PFPEs are also elucidated.

5.2.1.1 Preliminary Experiments and Results

5.2.1.1.1 Materials

LiTFSI and triethylamine (TEA) was obtained from Sigma Aldrich. Perfluoropolyether Fluorolink D10 (1000 g/mol) was obtained from Solvay-Solexis and Santa Cruz Biotechnology.

PFPEs and lithium salts were dried at 90 °C under vacuum in a glovebox antechamber or vacuum oven for at least 24h prior to the preparation of NMR samples. Deuterated water (D₂O) and acetone ((CD₃)₂CO) were obtained from Fisher Scientific and were used as purchased.

5.2.1.2 Experimental

5.2.1.2.1 Synthesis of PFPE-Dimethyl Carbonate

The synthesis of PFPE-DMC was previously described in Chapter 3. In brief, Fluorolink D10 (1000 g/mL, 0.02 moles) and TEA (0.7255 g/mL, 0.05 moles) were dissolved in 1,1,1,3,3-pentafluorobutane (500 mL) at 0 °C in an ice bath with stirring using a magnetic stir bar under a nitrogen atmosphere. A solution of methyl chloroformate (1.223 g/mL, 0.05 moles) was added drop wise (over approximately 1 minutes), after which the mixture was allowed to return to ambient conditions and stirred for 12 h. The resulting mixture was filtered under vacuum and the filtrate was washed with equal amounts of water three times and brine two times to remove residual triethylammonium hydrochloride salt. The remaining organic layer was dried over magnesium sulfate, filtered, and the solvent in the filtrate was evaporated under reduced pressure, providing the product PFPE-DMC, as a pale yellow translucent liquid. (Yield: 85 %+) FTIR (neat): 2886 cm⁻¹ (C-H), 1752 cm⁻¹ (C=O), 1184 cm⁻¹ (C-H), 1085 cm⁻¹ (C-O). ¹H NMR (400 MHz; CDCl₃; TMS; ppm): δ= 3.87 (s, 6 H), 4.52 (m, 4 H).

5.2.1.2.2 Preparation of NMR Samples

All experiments were performed on neat PFPE-diol/LiTFSI or PFPE-DMC/LiTFSI solutions by inserting a sealed coaxial insert (purchased from Norell; item number NI5CCI-B) containing a deuterated solvent (either D₂O or (CD₃)₂CO) for reference, locking, and shimming into the neat electrolyte samples. Schematic of a typical NMR sample is shown in Figure 5.1.



Figure 5.1 Schematic of NMR sample set up using a coaxial insert.⁶

5.2.1.2.3 Pfg-NMR Experimental Procedure

An overview of the pfg-NMR technique was previously described in Chapter 1. ⁷Li NMR was measured using a Bruker AVANCE500 spectrometer with a 11.7 Tesla wide bore (51 mm) superconducting magnet with a Bruker Broadband Observe (BBO) Z-gradient probe. Experiments operated at a frequency of 194 MHz at temperatures between 40 to 110 °C. Samples were heated inside the probe and held stable at the temperature of interest for at least 3 h prior to the start of each measurement. The pfg technique was used to measure *D* of Li-ions in PFPE-diol and PFPE-DMC. More specifically, a stimulated-echo pulse sequence with bipolar gradients (STEBp) (Figure 5.2), first developed by Cotts⁷ was used. This method, adapted from the gradient spin echo (SE) sequence first reported by Stejskal and Tanner,⁸ measures attenuated signal intensity described by experiment parameters through the equation:

$$I = I_0 e^{-D\gamma^2 g^2 \delta^2 (\Delta - \frac{\delta}{3})} \dots \dots \dots \text{equation 5.1}$$

where *I* is the observed intensity, *I*₀ is the reference intensity, *D* is the diffusion coefficient, γ is the gyromagnetic ratio of the observed nucleus, *g* is the gradient strength, δ is the length of the gradient and Δ is the diffusion time. Typical acquisition parameters for Δ and δ were 345 milliseconds and 5 milliseconds respectively. Due to the application of the bipolar gradients a correction for the time τ between the bipolar gradients has to be added to equation 5.1:

$$I = I_0 e^{-D\gamma^2 g^2 \delta^2 (\Delta - \frac{\delta}{3} - \frac{\tau}{2})} \dots \text{equation 5.2}$$

However, based on our calculations, D calculated from equation 5.1 and equation 5.2 are statistically equivalent because the correction $\frac{\tau}{2}$ is negligible.

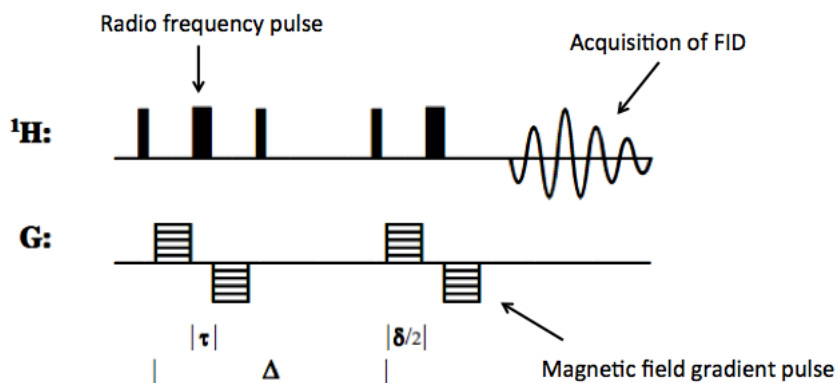


Figure 5.2 Sample STEbp pulse sequence as observed in the nucleus channel (in this example figure the nucleus channel is ^1H) and gradient channel (denoted by G). The radio frequency pulse, magnetic field gradient pulse, and acquisition of the free induction decay (FID) are also noted.

5.2.1.3 Discussion of Preliminary Results

The STE pulse sequence was used to measure D of ions in PFPE electrolytes because Annat and coworkers have previously shown that use of the STE technique was more accurate than the SE technique in viscous liquids due to better suppression of internal gradients and reduced loss of magnetization due to spin-spin relaxation.^{1,9,10} Bipolar gradient pulses, a further improvement to remove background magnetic field gradients due to inhomogeneities in the magnetic field,¹¹ were also used. This pulse sequence is provided by the Bruker TopSpin 3.2 software under the sequence name ‘stebpgp1s’. To validate the accuracy of this method the pfg technique was calibrated and crosschecked using the known D of H_2O at ambient temperatures ($2.23 \times 10^{-9} \text{ m}^2/\text{s}$).¹² Furthermore, D generated from the ‘stebpgp1s’ sequence were compared to that of a similar pulse sequence called the longitudinal eddy current delay with bipolar gradient

pulse (LEDbp) (found in Bruker TopSpin software as ‘ledbpgp2s’). This sequence additionally incorporates a delay time in order to minimize the effect of eddy currents caused by gradients. The presence of eddy currents induced by the metal structures of the magnet and probe due to gradient pulses can alter the position and phase of the spin echo signal, complicating and distorting the analysis of the calculation of D .^{10,13} D determined for Li-ions in a sample of 10 wt.% LiTFSI in PFPE-diol at temperatures from 40 to 75 °C, using both pulse sequences (Figure 5.3), however, demonstrated little difference in the values of D measured using the STEbp and LEDbp methods. Due to these results we deduced that the effects of eddy currents are minimal. Therefore, the STEbp technique can be used with confidence for subsequent studies going forward.

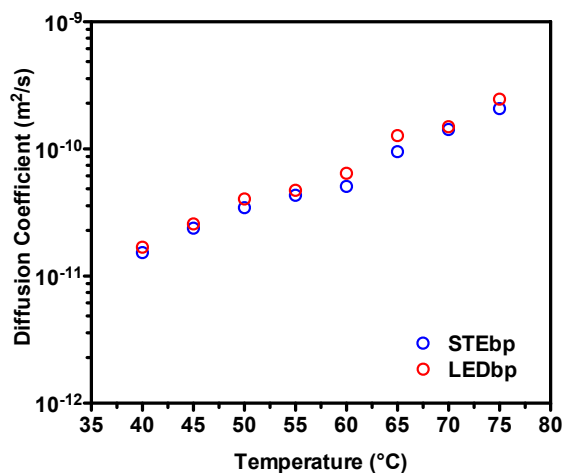


Figure 5.3 Measurement of D from STEbp and LEDbp sequences as a function of temperature.

The ⁷Li NMR spectrum of LiTFSI in PFPE-diol, regardless of lithium salt concentration, exhibits a single peak at approximately -2.4 ppm, indicating a homogenous lithium electronic environment on a timescale faster than the experimental NMR acquisition time (Figure 5.4). In other words, all the ⁷Li species in the sample experience a uniform environment as evidenced by the result that a single peak is observed. Using the STEbp sequence, signal intensity of the

single ^7Li peak was measured as function of gradient strength; 14-16 measurements of peak intensity were determined in the range from 2 % gradient strength to 95 % gradient strength (approximately 0 - 40 G/cm), producing a simulated diffusion decay curve (Figure 5.5). Between each measurement a delay was added to allow magnetization to dissipate; this delay, known as the recycle delay, was set to at least 5 times of the spin-lattice relaxation. The decay curve is subsequently fitted to equation 5.1 using the Bruker TopSpin T1/T2 software that which utilizes a process based on the SimFit algorithm¹⁴ to determine the parameter D .

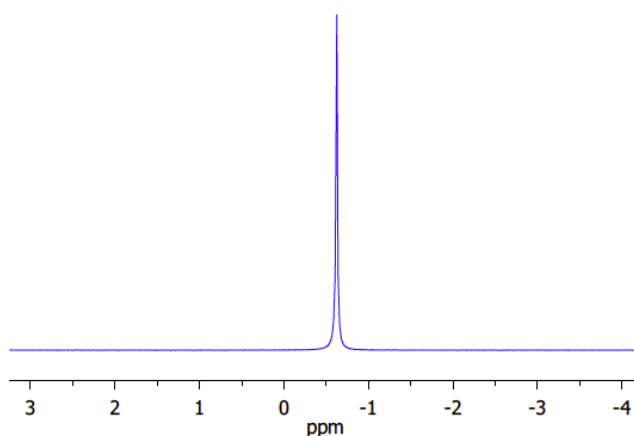


Figure 5.4 ^7Li NMR Spectrum of PFPE-diol with 10 wt.% LiTFSI at 20°C.

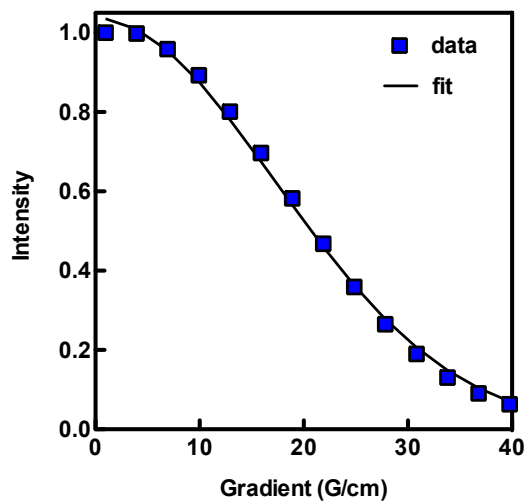


Figure 5.5 Simulated diffusion decay curve from 2 to 95% gradient strength in 14 steps obtained using Bruker TopSpin software. The data fit shown was achieved using equation 5.1.

It is important to note, however, that equation fitting of the decay curve is only accurate when the last intensity point, (attenuated signal with greatest gradient strength), has an intensity of only 5% relative to the first point, known as the reference signal. In other words, the intensity of the peak at 95% gradient strength must be approximately 95% smaller than the intensity of the peak at 0% gradient strength in order to calculate the diffusion coefficient D . At room temperature, the attenuated signal of lithium is significantly greater than 5% of the reference signal in PFPE samples; in these cases, diffusion decay curves look similar to the curve illustrated in Figure 5.6 and D values cannot be confidently determined. This occurs because diffusion of the lithium species is too slow at room temperature and the power of the Bruker Z-gradient probe used is insufficient to induce significant diffusion. In order to address this concern, NMR samples were heated to at least 40 °C so that D values were sufficiently large enough so that measurements were possible.

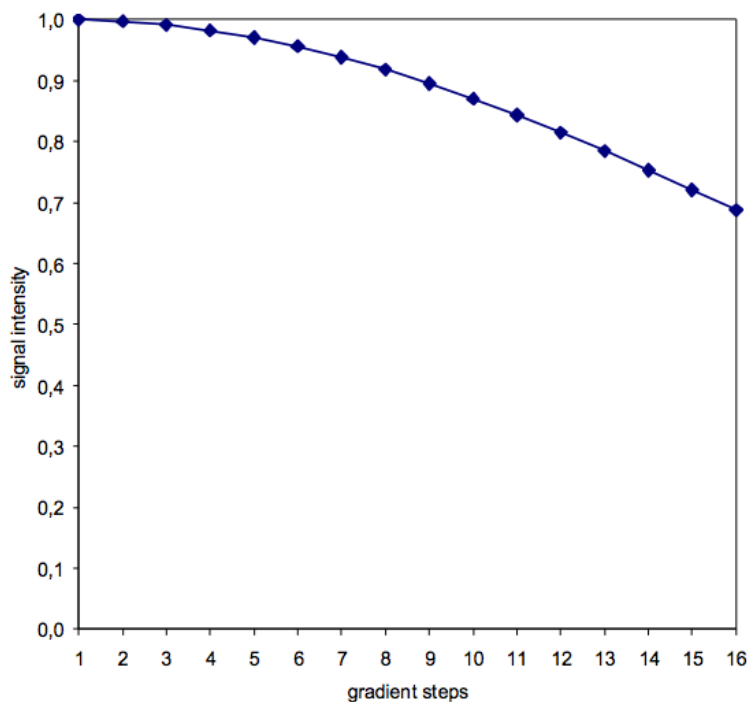


Figure 5.6 Diffusion decay curve where the intensity has not decayed sufficiently even at 95% gradient strength.

⁷Li diffusion coefficients were measured for PFPE-diol and PFPE-DMC samples containing 10 wt.% LiTFSI between 40 °C (3.2 K⁻¹) to 110 °C (2.6 K⁻¹) and are shown in an Arrhenius plot in Figure 5.7, which was graphed by plotting the natural log of the *D* values against the inverse temperature in Kelvin. As shown in Figure 5.7, *D* for Li-ions in PFPE-DMC increase linearly with increasing temperature, reaching as high as 3.4x10⁻¹⁰ m²/s at 110 °C, thus exhibiting Arrhenius type temperature dependence in the form:¹¹

$$D = D_{\infty} e^{\left[\frac{E_D}{RT}\right]} \dots \dots \dots \text{equation 5.3}$$

where *D*_∞, *E*_{*D*}, *R* and *T* are the diffusion coefficient at infinite temperature, activation energy required for diffusion, gas constant and temperature respectively. This Arrhenius temperature dependence of *D* is a typical behavior of electrolytes, and has previously been observed with other electrolyte systems in the literature.¹¹ PFPE-diol, however, does not follow this trend. Although Li-ions in this electrolyte demonstrate similar diffusion coefficients to PFPE-DMC at temperatures above 80°C, diffusion deteriorates to as low as 1.8x10⁻¹² m²/s at 50 °C. Because the two types of electrolytes consist of similar molecular weight and salt concentration, this suggests that end group functionality may contribute significantly to diffusion at lower temperatures. This result is surprising since our previous studies have shown that PFPE-diol and PFPE-DMC, at the same salt concentrations, exhibit statistically equivalent ionic conductivities at temperatures from 25 to 120 °C (Chapter 3), suggesting that the direct effects of end group on conductivity is negligible.⁵ Ongoing investigations include repeating these studies for statistical accuracy as well as expanding our scope to other end group moieties to definitively determine the effects of end group on Li-ion diffusion. Although *D* values of PFPE-diols and PFPE-DMCs measured here are comparable to that of gel and polymeric electrolytes in the literature,¹⁵ determination of *D* values

of standard or well studied electrolyte systems such as PEG or PEO using our STE procedure described above is also needed before direct comparisons can be made.

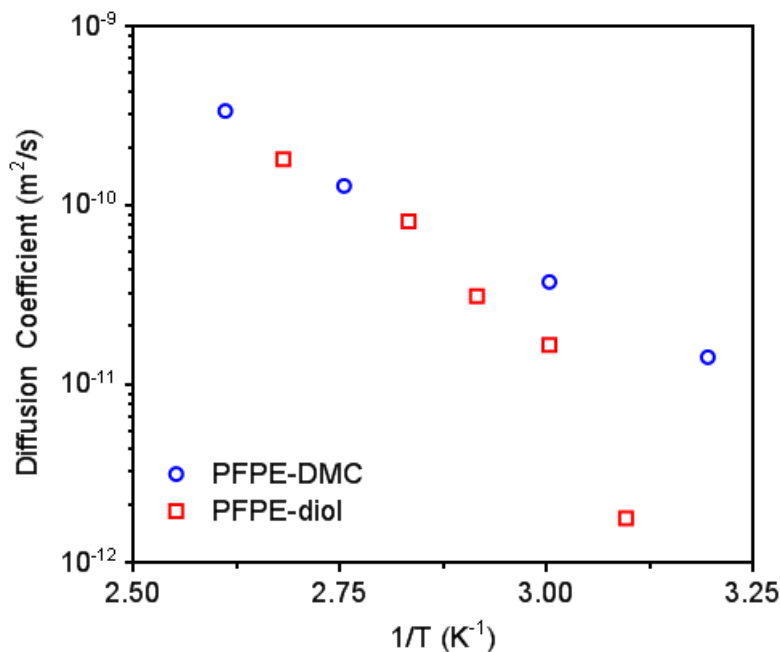


Figure 5.7 D values of Li-ions in PFPE-DMC (open blue circles) and PFPE-diol (open red squares) as a function of temperature (K^{-1})

In this work so far, we have confirmed that diffusion of Li-ions in PFPE electrolytes can be successfully measured using the pfg-NMR method and STEbp pulse sequences. However, it is clear that expansion of these results is essential before drawing definitive conclusions regarding ion transport in these materials. The pfg-NMR method should be repeated using ^{19}F NMR so that D can be determined for the TFSI⁻ counterion and the backbone of PFPE oligomers. After the determination of D for both Li-ions and TFSI⁻, t^+ can subsequently be calculated using equations described in Chapter 1. D values should also be measured for PFPE electrolytes at various LiTFSI concentrations to elucidate the effects of salt concentration on diffusion and t^+ . Ultimately, ionic environments surrounding lithium salts in PFPEs can be further understood by

coupling results obtained from pfg-NMR and ionic conductivity measurements to establish the degree of salt association and ion-ion pairing (previously discussed in Chapter 1).^{1,11,15,16}

5.2.2 Other Possible NMR Experiments: Determination of Linewidth and Relaxation

NMR spectroscopy offers an abundance of tools and techniques that can compliment pfg-NMR methodologies and sample dynamics over multiple timescales (from Hz to MHz frequency range): linewidth and relaxation measurements also provide important information regarding ion and polymer coordination and dynamics in Li-ion battery electrolytes.¹⁷

5.2.2.1 Linewidth

The full width at half-maximum (FWHM) of one dimensional (1D) NMR spectral peaks defines the peak linewidth and is a common parameters used to describe ion mobility and ion-polymer coordination in electrolytes.¹⁷ Mobility, μ , is related to ionic conductivity, σ , in the amorphous phase of polymers through the equation:^{18,19}

$$\sigma = \sum_i n_i q_i \mu_i \dots \dots \dots \text{equation 5.4}$$

where n_i , q_i are the number of charge carriers and the charge on each carrier respectively.

Therefore, measuring mobility is a valuable tool to apply when aiming to optimize ionic conductivity and battery performance. When measured as a function of temperature, FWHM is also indicative of the dipole-dipole interactions inherent to the system, a result of ion hopping and polymer chain segmental motion. Studies involving linewidth measurement in PFPE electrolytes with LiTFSI would therefore contribute insightful information regarding local ion interactions and motion.

We began preliminary investigations of Li-ion mobility by measuring linewidths of the single lithium peak in ⁷Li NMR spectra of PFPE electrolytes as a function of temperature. For the ⁷Li nuclei, spectral linewidths are a result of quadrupolar or internuclear dipole-dipole

interactions.²⁰ If Li-ions are immobile, these interactions intensify, resulting in peak broadening and an increase in linewidth. On the other hand, as the mobility of Li-ions increases, linewidth decreases due to averaging of these interactions.^{18,19} This behavior is shown in Figure 5.8, which shows the change in linewidth as a sample of PFPE-diol containing 10 wt. % LiTFSI is cooled. With decreasing temperature, linewidth increases, suggesting temperature dependence of ion mobility and reduced Li-ion mobility and conductivity at lower temperatures. This behavior is consistent with carbonate and other polymer electrolytes systems.^{18,19}

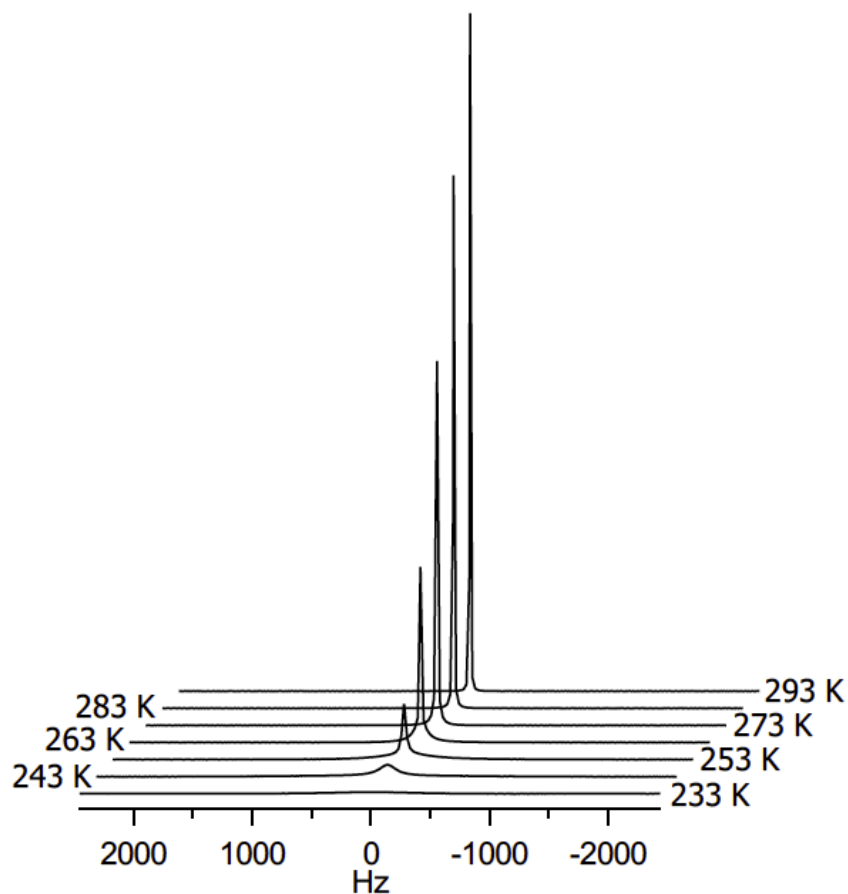


Figure 5.8 ^7Li NMR spectra of PFPE-diol containing 10 wt. % LiTFSI from 20 to -40°C (293 to 233 K).

Building upon these preliminary results, investigations at even lower temperatures are being continued to determine the onset of linewidth narrowing, also known as the temperature at

which a sharp decrease of FWHM occurs. In the case of polymer electrolytes, this narrowing frequently occurs near the T_g of the polymer, attributing the coupling between ion dynamics and polymer segmental motions in these systems.²¹ If Li-ion mobility is therefore, closely associated to the relaxations of PFPE chains, then the expected onset of linewidth narrowing for PFPE-diol containing 10 wt. % LiTFSI is expected to be at approximately -90 °C. Importantly, linewidths as a function of PFPE end group, chemical structure, molecular weight and LiTFSI concentrations should also be investigated in order to elucidate the effects of chemical structure and salt content on ion hopping and polymer chain segmental motion.

5.2.2.2 Relaxation

NMR relaxation time for lithium nuclei also provides important information regarding ion transport in polymer electrolyte systems. In particular, spin-lattice relaxation, also known as longitudinal relaxation or T_1 , for ^7Li NMR, is a common tool used to probe local Li-ion environments. Obtained experimentally by a standard inversion-recovery pulse sequence, T_1 measurements record the time required for a nuclei's spin to return to equilibrium after a pulse that inverts its magnetization (also known as a 180° pulse, inversion pulse or π pulse) (Figure 5.9);³ T_1 relaxation time increases as interaction between the nuclei and its surroundings increases. Studying T_1 relaxation at various temperatures also determines the temperature at which the relaxation minimum occurs (Figure 5.10), enabling determination of lithium correlation times and activation energies for ion motion in the polymer host, which have previously been used to provide a detailed perspective on the relationship between Li-ion hopping motion and segmental motion of polymers, a crucial understanding for fundamental cation transport mechanisms in polymer electrolytes.^{3,18,22} Comparing the relative T_1 minima

between PFPE electrolytes with various end groups also enables relative ion motilities to be evaluated.

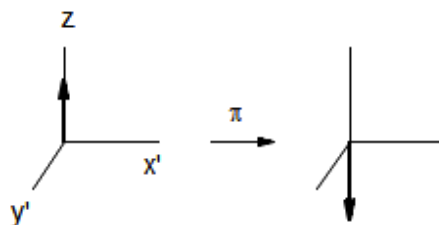


Figure 5.9 Illustration of a π pulse and its effects on magnetic spin.²³

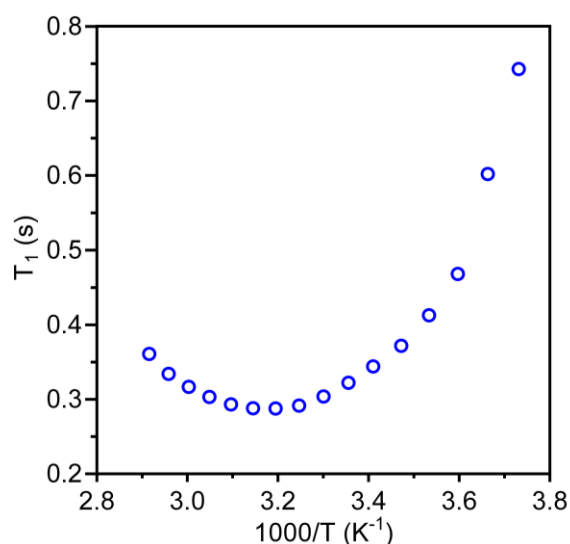


Figure 5.10 Sample graph of T_1 relaxation as a function of inverse temperature (K^{-1}). A T_1 minimum is shown here at approximately $3.15 K^{-1}$ ($44\text{ }^\circ C$).

5.3 Investigation of PFPE/Electrode Interfaces

Stability of PFPE-based electrolytes in electrodes such as lithium metal and nickel manganese cobalt oxide (NMC) have previously been studied; coin cell batteries assembled using these components are capable of cycling at various charge rates without significant loss in energy capacity.⁵ Those results pave the way for investigating the compatibility between PFPE electrolytes and other commonly used electrodes. The potential to pair PFPEs with anodes such as graphite and iron oxide is especially attractive due to the possibility of eliminating the use of

thermally unstable lithium metal as a battery component. Venturing further into this area, however, would be limited without understanding both the short and long term behavior of PFPE/electrode interfaces during or after battery cycling. Degradation of electrodes or electrolytes at the interface that results in loss of active material have significant effects on the long term performance and cycle life of batteries: for example, irreversible oxidation or reduction of the composition of the electrode responsible for Li-ion intercalation would reduce energy retention and storage capacities.

With regards to liquid carbonate-based electrolytes, a common strategy to extend performance and cycle life of batteries is to allow or induce formation of a thin passivating film or layer called the solid-electrolyte interface (SEI). In the case of batteries composed of small molecule carbonate solvents, newly assembled cells undergo a long conditioning charge step prior to full operation to fully lithiate the anode. When this occurs, the electrolyte carbonate molecules at the electrode surface are electrochemically reduced and irreversibly degrade, forming a heterogeneous insoluble film at the interface. This film, known as the SEI, act as a passivation layer that physically separates the electrode from the rest of the electrolyte solvent and prevents further electrolyte break down and electrode exfoliation.²⁴ The formation of a SEI layer prolongs life spans of active materials and extends battery cycle life. Due to this separation from the electrode, formation of the SEI layer also allows carbonate electrolytes to be paired with electrodes having a potential beyond their electrochemical window. Although the formation of an SEI layer inevitably increases the cell internal impedance over time, it is still considered by many research groups to be essential for practical charge efficiency and stability of lithium secondary cells using carbon anodes.²⁵ While the theory and mechanism of SEI formation in carbonate solvents are currently being extensively studied, the study of PFPE electrolytes

changes and reactions at the electrode interface during battery operation is still at its infancy. It is uncertain whether similar SEI formation mechanisms occur with PFPEs or if there is irreversible electrode degradation over time due to contact with PFPEs.

5.3.1 Characterization of PFPE/Electrode Interfaces

Multiple methods can be utilized to monitor structural and composition changes at electrolyte/electrode interfaces. Fourier transform infrared spectroscopy (FTIR), X-ray photoelectron spectroscopy (XPS) and scanning electron microscopy (SEM) are amongst the most commonly used techniques in this regard.²⁶⁻²⁸ XPS, for example, enables quantitative chemical analysis of almost all elements and differentiates functional groups based on binding energies to probe molecular environments throughout the surface. Depth profiling analysis could also be used to study changes in environments as a function of distance from the interface.²⁷ These techniques could similarly be applied to batteries with PFPEs. Typical experiments involve the isolation of wetted electrodes from disassembled battery cells after cycling and studying the surface with these electrodes to probe for changes in electrode thickness, surface roughness, and surface composition.

Furthermore, rapid development of novel sample preparation methods and electrochemical cells has led to state-of-the-art in situ techniques such as in situ atomic force microscopy (AFM) and transmission electron microscopy (TEM).^{27,29-32} For example, Cui and coworkers have reported the observation of silicon anode materials upon first charge using in situ TEM.³³ These techniques monitor the true real-life environments of enclosed battery cells and allow for quantitative analysis with minimal destructive impact. Cells with PFPEs could also be studied in this manner.

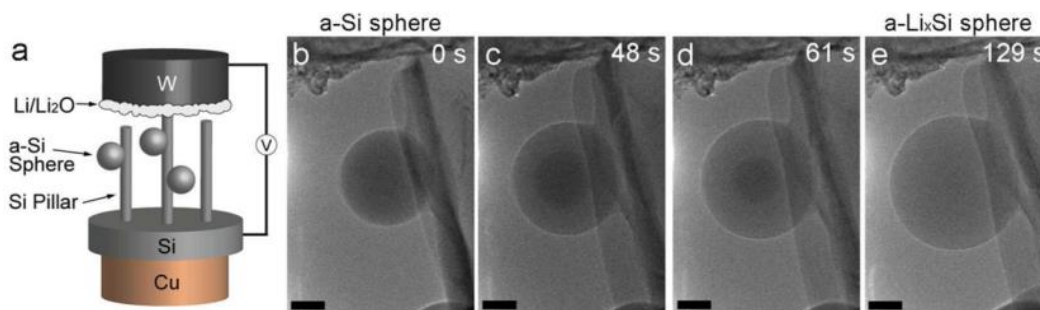


Figure 5.11 In situ TEM experiments reported by Cui and coworkers in *Nano Letters*. (a) schematic of a typical in situ TEM cell. (b-d) Time series of the lithiation of a single silicon sphere (a-Si sphere and a-Li_xSi sphere indicates unlithiated and lithiated spheres respectively).³³

5.3.2 Enhancing SEI Formation through Incorporation of Ethylene Carbonate

Complimentary to instrumental techniques that can be used to study PFPE/electrode interfaces, synthetic and formulation strategies can also be employed to optimize electrolyte design towards stability with electrodes and potential SEI formation. Incorporation of ethylene carbonate (EC) has been extensively studied as an additive to enhance SEI formation and stability against anodes such as graphite in ionic liquids³⁴ and carbonate-based solvents.^{35,36} While the exact composition and reaction pathway of SEI formation is still widely controversial, it has been shown that addition of EC into electrolytes successfully leads to stable SEI formation and prevents graphite exfoliation and anode destruction, thus resulting in improved battery performance and cycle life.³⁷

A proposed approach is to synthesize and study copolymer electrolytes composed of both PFPE and EC. PFPE-ethylene carbonate (PFPE-EC) block copolymers can be synthesized first through the preparation of a vinyl ether carbonate monomer via transesterification of ethyl vinyl ether and glycerol carbonate catalyzed by a palladium (II) complex, first described by Boutevin and coworkers (Figure 5.12).³⁸ Subsequently, the vinyl ether ethylene carbonate monomer could be copolymerized with dimethacrylate-terminated PFPEs (Figure 5.13). Monomer composition,

molecular weight, and polydispersity can potentially be controlled using living polymerization methodologies such as atom transfer radical polymerization (ATRP).³⁹

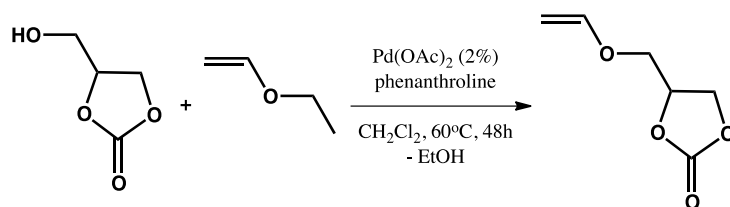


Figure 5.12 Synthesis of vinyl ethers bearing carbonate side groups, as reported by Boutevin and coworkers in *the Journal of Polymer Science*.³⁸

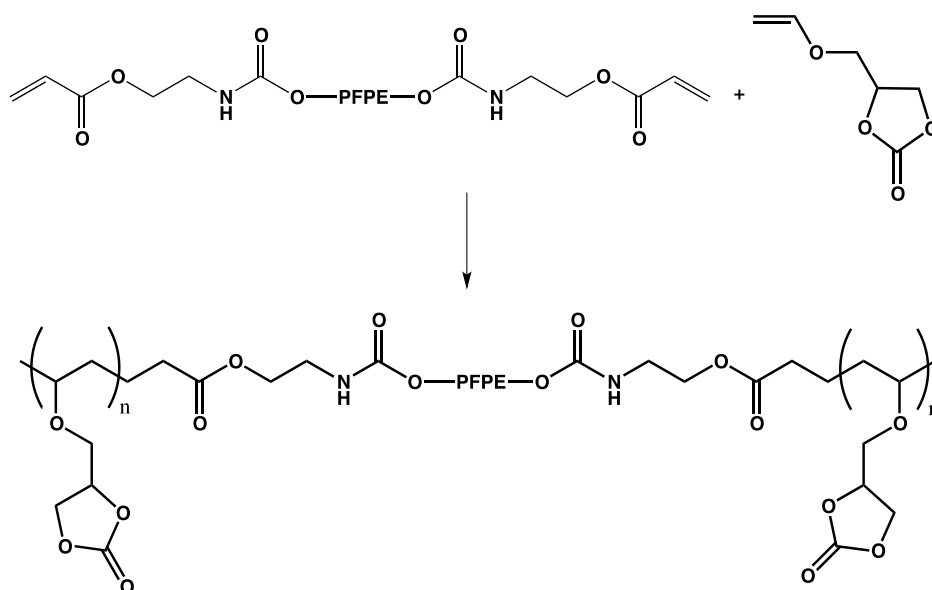


Figure 5.13 Proposed synthetic scheme of the synthesis of PFPE-EC electrolytes

Addition of EC functional groups could promote SEI formation through the ring opening mechanism of cyclic carbonates by the reduction pathway previously described,⁴⁰ thus potentially increasing the compatibility of PFPE electrolytes with carbon-based electrodes such as graphite. Functionalization of additional carbonate moieties could also increase the LiTFSI salt loading in these electrolytes; thereby increasing its conductivity limits without sacrifice its near-unity transference number.

5.3.3 Investigation of Failure Modes

Investigation of PFPE/electrode surfaces could also be expanded to include studies of lithium dendrite formation over numerous charge and discharge cycles. One of the most common reasons for long term battery failure is related to dendrites composed of lithium metal that are irreversibly produced and protrude from lithium metal anodes as batteries are cycled (Figure 5.14).⁴¹ The passage of current through these structures eventually leads to short-circuiting of the cell, reducing the life span of the battery.

Growth of lithium dendrites could be monitored through ex situ and in situ characterization methods previously described in this chapter, such as AFM and TEM. In a recent study, Balsara and coworkers have additionally used synchrotron X-ray tomography to study underneath polymer electrolyte/lithium metal interfaces, demonstrating that early dendritic growth begin from within the electrode as well.⁴² These techniques can be applied to the examination of cycled PFPE-based cells to determine failure modes and identify the reasons for capacity fade and cell death.^{42,43}

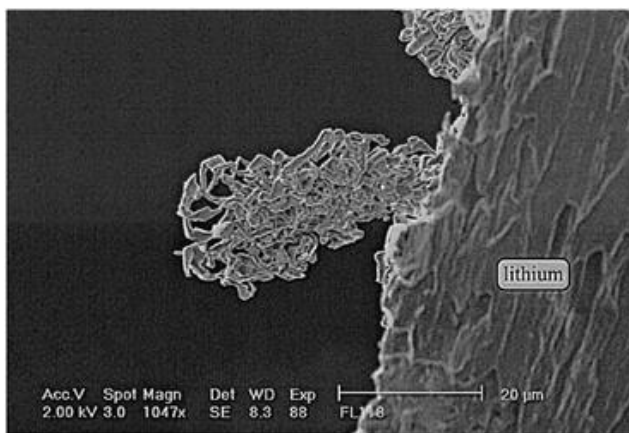


Figure 5.14 Dendritic lithium formed in a lithium battery, as observed by Notten and coworkers in *The Journal of Power Sources*.⁴⁴

REFERENCES

- (1) Zugmann, S.; Fleischmann, M.; Amereller, M.; Gschwind, R. M.; Wiemhöfer, H. D.; Gores, H. J. *Electrochimica Acta* **2011**, *56*, 3926.
- (2) Zhao, J.; Wang, L.; He, X.; Wan, C.; Jiang, C. *Journal of The Electrochemical Society* **2008**, *155*, A292.
- (3) Abbrent, S.; Greenbaum, S. *Current Opinion in Colloid & Interface Science* **2013**, *18*, 228.
- (4) Walderhaug, H.; Söderman, O.; Topgaard, D. *Progress in Nuclear Magnetic Resonance Spectroscopy* **2010**, *56*, 406.
- (5) Wong, D. H. C.; Thelen, J. L.; Fu, Y.; Devaux, D.; Pandya, A. A.; Battaglia, V. S.; Balsara, N. P.; Desimone, J. M. *Proc Natl Acad Sci U S A* **2014**, *111*, 3327.
- (6) <http://www.wilmad-labglass.com/Products/WGS-5BL/>.
- (7) Cotts, R. M.; Hoch, M. J. R.; Sun, T.; Markert, J. T. *Journal of Magnetic Resonance* **1989**, *83*, 252.
- (8) Stejskal, E. O.; Tanner, J. E. *J. Chem. Phys.* **1965**, *42*, 288.
- (9) Annat, G.; MacFarlane, D. R.; Forsyth, M. *J. Phys. Chem. B* **2007**, *111*, 9018.
- (10) Wu, D.; Chen, A.; Charles Johnson, J. *Journal of Magnetic Resonance. Series A* **1995**, *115*, 260.
- (11) Richardson, P. M.; Voice, A. M.; Ward, I. M. *Electrochimica Acta* **2014**, *130*, 606.
- (12) Hayamizu, K.; Aihara, Y.; Arai, S.; Martinez, C. G. *J. Phys. Chem. B* **1999**, *103*, 519.
- (13) Johnson Jr., C. S. *Progress in Nuclear Magnetic Resonance Spectroscopy* **1999**, *34*, 203.
- (14) Kerssebaum, R.; Bruker BioSpin GmbH: Rheinstetten, Germany, 2002.
- (15) Williamson, M. J.; Hubbard, H. V. S. A.; Ward, I. M. *Polymer* **1999**, *40*, 7177.
- (16) Stolwijk, N. A.; Kösters, J.; Wiencierz, M.; Schönhoff, M. *Electrochimica Acta* **2013**, *102*, 451.
- (17) Volkov, V. I.; Marinin, A. A. *Russian Chemical Reviews* **2013**, *82*, 248.

- (18) Jeon, J.-D.; Kwak, S.-Y. *Macromolecules* **2006**, *39*, 8027.
- (19) Every, H. A.; Zhou, F.; Forsyth, M.; MacFarlane, D. R. *Electrochimica Acta* **1998**, *43*, 1465.
- (20) Croce, F.; Brown, S. D.; Greenbaum, S. G.; Slane, S. M.; Salomone, M. *Chem. Mater.* **1993**, *5*, 1268.
- (21) Sequeira, C. A. C.; Santos, D. M. F. *Polymer Electrolytes: Fundamentals and Applications* Woodhead Publishing Limited: Cambridge 2010.
- (22) Arun, N.; Vasudevan, S.; Ramanathan, K. V. *The Journal of Chemical Physics* **2003**, *119*, 2849.
- (23) Reich, H. J.; University of Wisconsin
<http://www.chem.wisc.edu/areas/reich/nmr/08-tech-01-relax.htm>, 2011.
- (24) Nie, M., University of Rhode Island 2014.
- (25) *Lithium-Ion Batteries: Solid-Electrolyte Interphase* Imperial College Press: London, 2004.
- (26) Chattopadhyay, S.; Lipson, A. L.; Karmel, H. J.; Emery, J. D.; Fister, T. T.; Fenter, P. A.; Hersam, M. C.; Bedzyk, M. J. *Chemistry of Materials* **2012**, *24*, 3038.
- (27) Verma, P.; Maire, P.; Novák, P. *Electrochimica Acta* **2010**, *55*, 6332.
- (28) Park, Y.; Shin, S. H.; Hwang, H.; Lee, S. M.; Kim, S. P.; Choi, H. C.; Jung, Y. M. *Journal of Molecular Structure* **2014**, *1069*, 157.
- (29) Cresce, A. v.; Russell, S. M.; Baker, D. R.; Gaskell, K. J.; Xu, K. *Nano Lett* **2014**, *14*, 1405.
- (30) Wu, F.; Yao, N. *Nano Energy* **2015**, *11*, 196.
- (31) Dollé, M.; Grugeon, S.; Beaudoin, B.; Dupont, L.; Tarascon, J. M. *Journal of Power Sources* **2001**, *97–98*, 104.
- (32) Tokranov, A.; Sheldon, B. W.; Li, C.; Minne, S.; Xiao, X. *ACS Appl Mater Interfaces* **2014**, *6*, 6672.
- (33) McDowell, M. T.; Lee, S. W.; Harris, J. T.; Korgel, B. A.; Wang, C.; Nix, W. D.; Cui, Y. *Nano Lett* **2013**, *12*, 758.

- (34) Fu, Y. B.; Chen, C.; Qiu, C. C.; Ma, X. H. *Journal of Applied Electrochemistry* **2009**, *39*, 2597.
- (35) Wang, X. J.; Lee, H. S.; Li, H.; Yang, X. Q.; Huang, X. J. *Electrochemistry Communications* **2010**, *12*, 386.
- (36) Bhatt, M. D.; O'Dwyer, C. *Current Applied Physics* **2014**, *14*, 349.
- (37) Shkrob, I. A.; Zhu, Y.; Marin, T. W.; Abraham, D. *The Journal of Physical Chemistry C* **2013**, *117*, 19255.
- (38) Alaaeddine, A.; Boschet, F.; Ameduri, B.; Boutevin, B. *Journal of Polymer Science Part a-Polymer Chemistry* **2012**, *50*, 3303.
- (39) Wang, J. S.; Matyjaszewski, K. *Macromolecules* **1995**, *28*, 7901.
- (40) Wang, F.-M.; Yu, M.-H.; Hsiao, Y.-J.; Tsai, Y.; Hwang, B.-J.; Wang, Y.-Y.; Wan, C.-C. *International Journal of Electrochemical Science* **2011**, *6*, 1014.
- (41) Tarascon, J. M.; Armand, M. *Nature* **2001**, *414*, 359.
- (42) Harry, K. J.; Hallinan, D. T.; Parkinson, D. Y.; MacDowell, A. A.; Balsara, N. P. *Nat Mater* **2014**, *13*, 69.
- (43) Stock, S. R.; MacDowell, A. A.; Parkinson, D. Y.; Haboub, A.; Schaible, E.; Nasiatka, J. R.; Yee, C. A.; Jameson, J. R.; Ajo-Franklin, J. B.; Brodersen, C. R.; McElrone, A. *J. Developments in X-Ray Tomography Viii* **2012**, *8506*, 850618.
- (44) F. Orsini, A. D. P., B. Beaudoin, J. M. Tarascon, M. Trentin, N. Langenhuizen, D. E. Beer, P. Notten *Journal of Power Sources* **1998**, *76*, 19.